Design of Tunable Hybrid Metal-Semiconductor Metasurfaces for Tailored Control of Light-Driven Reactions

Dissertation

for the acquisition of the academic title
Doktor Rerum Naturalium (Dr. rer. Nat.)



submitted to
the Council of the Faculty of Physics and Astronomy
of the Friedrich-Schiller-Universität Jena

by M.Eng. Ning Lyu
born on 17.06.1993 in Changchun, China

Reviewers:

1. Dr. habil. Christin David

2. Prof. Dr. Carsten Rockstuhl

3. A/Prof. Dr. Alejandro Manjavacas

Date of the Disputation: 13.04.2026

Abstract

A central aim of photochemistry is to develop a strategy to meet increasing global energy demands while achieving net-zero emissions through multibranched reaction pathways, such as the synthesis of energy-dense hydrocarbons or biofuels, an essential step toward a renewable energy-based economy. Recent advances in nanophotonics, especially in plasmonic hybrid nanostructures, can enable resonance-driven chemical transformations *via* localized surface plasmon resonances (LSPRs). The tunable and wavelength-dependent properties of these resonances allow precise control of catalytic performance, enabling manipulation of reaction reactivity hold the potential in improving chemical products selectivity and providing an efficiency sustainable energy storage solution.

In this thesis, I theoretical and experimental develop various plasmonic-based metasurfaces to support tunable plasmonic resonance through multiple strategies, including resonance-mode hybridization, polarization-dependent control, and phase-change material switching. This optical property can drive target chemical reactions through two non-thermal LSPR mechanisms: (1) near-field enhancement, which amplifies localized electromagnetic fields, and (2) hot-electron energy transfer, which injects energetic electrons into reactant molecules, effectively modulating the electron population at unoccupied reactant molecular orbitals determine controlling in reactivity. The catalytic performance of these metasurfaces is investigated using the N-demethylation of methylene blue (MB) as a model reaction, primarily driven by these two effects. That enable manipulation in correlated reactivity, and real-time monitoring through surface-enhanced Raman spectroscopy (SERS).

First, I design the self-assemble Au nanoparticle-cavity to tune plasmonic resonances through coupling with Fabry-Pérot (F-P) modes by varying the TiO_2 cavity thickness. By optimizing the spatial and spectral overlap between F-P node/peak and plasmonic resonances, the Au nanoparticle -cavities support a wide range tunable plasmonic resonance at target wavelength

to enable either suppression or enhancement of the MB degradation reaction. A significant tunability results in over a 100-fold modulation of product yield from 0.07 to 7.18. This strategy demonstrates a wide range manipulation of photo-reactivity through optical mode hybridization with a device-level scalability.

Next, I develop an elliptical Au nanodisk-TiO_2 nanopillar metasurface to achieve polarization-sensitive plasmonic resonances within a single configuration. The absorption peak wavelength, determined by the axis length of the elliptical nanodisks, can be tuned from 650 to 850 nm by switching the polarization of the incident light. In a model reaction, the product yield is gradually modulated from 4.7 to 9.98 within 10 s through polarization switching, attributed to the tunability of the plasmonic resonance at the target wavelength of 633 nm. Moreover, the yield exhibits a linear relationship with the metasurface absorption, demonstrating continuous and predictable control of reaction reactivity.

Finally, I investigate dynamic resonance tunability by integrating a phase-change material (PCM), Sb_2S_3, as the material of cavity. The Au nanodisk array coupled with the F-P resonance of the Sb_2S_3 cavity, enabling refractive index shifting between amorphous and crystalline phases. Strong plasmonic resonance aligns with the MB reaction wavelength with amorphous metasurface, and a reduction induced by crystallization, which results in a 2.4-fold modulation in product yield. Although the reactivity manipulation is restricted by the thermal stability of cavity phase, this metasurface illustrates the potential for dynamic and reversible catalytic control with phase switching.

Overall, I demonstrate and investigate precise reactivities modulation of resonance driven reaction by tailoring LSPR strength across various metasurface configurations. These results establish a versatile framework for plasmonically control of photochemical reactivity, offering pathways toward selective and efficient solar-driven chemical synthesis.

Zusammenfassung

Ein zentrales anliegen der Photochemie ist Strategien zu entwickeln, um gleichermaßen den weltweit steigenden Energiebedarf zu decken und Netto-Null-Emissionen zu erreichen. Mehrschrittige Reaktionen wie die Synthese energiereicher Kohlenwasserstoffe und Biokraftstoffe sind entscheidende Schritte hin zu einer auf erneuerbaren Energien basierenden Wirtschaft. Jüngste Fortschritte in der Nanophotonik und im Besonderen in plasmonischen Hybrid-Nanostrukturen erlauben resonanzgetriebene chemische Umwandlungen unter Ausnutzung lokaler Oberflächenplasmonresonanzen (LSPRs). Die regelbaren und wellenlängenabhängigen Eigenschaften dieser Resonanzen ermöglichen eine präzise Steuerung der katalytischen Wirksamkeit und somit der Reaktionsaktivität mit dem Potential verbesserter selektivität chemischer Produkte und effizienter erneuerbarer Energiespeicherung.

In dieser Arbeit entwickle ich theoretisch und experimentell verschiedene Metaoberflächen, die abstimmbare Plasmonresonanzen beherbergen können. Als Strategien verfolge ich Resonanzmodenhybridisierung, polarisationsabhängige Kontrolle und den Einsatz von Phasenwechselmaterialien. Die optischen Eigenschaften solcher plasmonischer Strukturen ermöglichen es, chemische Zielreaktionen über zwei verschiedene nicht-thermische LSPR-Mechanismen zu realisieren. Bei der Nahfeldverstärkung (1) werden lokale elektromagnetische Felder verstärkt, während bei dem Transfer heißer Elektronen (2) energiereiche Elektronen in Reaktantmoleküle injiziert werden. Durch letzteres können unbesetzte molekulare Orbitale der Reaktanten mit Elektronen besetzt werden und damit gezielt deren Reaktivität angepasst werden. Die katalytische Leistung dieser Metaflächen wird anhand der N-Demethylierung von Methylenblau (MB) als Modellreaktion untersucht, die hauptsächlich durch diese beiden Effekte bestimmt wird. Diese ermöglichen sowohl die

Steuerung der korrelierten Reaktivität als auch die Echtzeitüberwachung mittels oberflächenverstärkter Raman-Spektroskopie (SERS).

Zunächst entwarf ich eine selbstorganisierende Gold-Nanoteilchenkavität, um Plasmonresonanzen über die Kopplung an Fabry-Pérot (F-P) Moden durch die Variation der TiO_2-Kavitätsdicke abzustimmen. Durch die Optimierung des räumlichen und spektralen Überlapps zwischen F-P Knoten/Peaks und Plasmonresonanzen können Gold-Nanoteilchenkavitäten eine große Bandbreite an abstimmbaren Plasmonresonanzen mit Zielwellenlängen unterstützen, um die MB-Abbaureaktion zu unterdrücken oder zu verstärken. Die Produktausbeute lässt sich dadurch um etwa das Hundertfache von 0,07 auf 7,18 erhöhen. Diese Strategie zeigt, dass sich die Photoreaktivität durch optische Modenhybridisierung weitgehend maßschneidern lässt, mit Skalierbarkeit auf Geräteebene.

Anschließend entwickelte ich eine Metaoberfläche, bestehend aus elliptischen Gold-Nanodisks und TiO_2-Nanopfeilern, um polarisationabhängige Plasmonresonanzen innerhalb einer einzigen Konfiguration zu realisieren. Die Wellenlänge des Apbsorptionspeaks, bestimmt durch die Achsenlänge der elliptischen Nanodisks, kann durch die Polarisation des einfallenden Lichts zwischen 650 nm und 850 nm variiert werden. In einer Modellreaktion konnte die Produktausbeute innerhalb von 10 s, mittels Polarisationswechsel, von 4,7 auf 9,98 geändert werden, was wir der Plasmonresonanz mit der Zielwellenlänge von 633 nm zuschreiben. Zudem weist die Produktausbeute einen linearen Zusammenhang zur Absorption der Metaoberfläche auf, was eine stetige und vorhersagbare Änderung der Reaktionsreaktivität aufzeigt.

Abschließend untersuchte ich das dynamische Durchstimmen von Resonanzen durch die Integration des Phasenwechselmaterials (PCM) Sb_2S_3 für die Kavität. Die Gold-Nanodiskmatrix, gekoppelt an die Fabry-Pérot Resonanz dieser Sb_2S_3-Kavität, ermöglicht eine Änderung der Brechzahl zwischen amorpher und kristalliner Phase. Im amorphen Zustand der Metaoberfläche tritt bei der Wellenlänge für die MB-Reaktion eine starke Plasmonresonanz auf, welche hingegen im Fall der kristallinen Phase abgeschwächt ist. Der Unterschied der Produktausbeute beläuft sich auf das 2,4-fache. Die untersuchte Metaoberfläche verdeutlicht, dass eine dynamische und reversible katalytische Kontrolle mittels Phasenwechsel implementiert werden kann, obgleich die Anpassung der Reaktivität durch die thermische Stabilität der Kavitätsphase eingeschränkt ist.

Insgesamt konnte ich über verschiedene Konfigurationen von Metaoberflächen hinweg zeigen, dass maßgeschneiderte Oberflächenplasmonresonanzen eine präzise Kontrolle der Reaktivität von resonanzgetriebenen chemischen Reaktionen erlauben. Diese Ergebnisse eröffnen vielseitige Einsatzgebiete für die plasmonische Steuerung von photochemischen Reaktionen hin zu einer selektiven und effizienten solargetriebenen chemischen Synthese.

Contents

Abstract I
Zusammenfassung III
Chapter 1. Introduction 3
1.1. Introduction of light-driven reactions 3
1.2. Plasmonic metasurfaces in light-driven reactions 6
Chapter 2. Principles of metasurface modelling and light-driven reactions 10
2.1. Optical simulation with finite element method 10
2.1.1. Fundamental principles of electric field simulation and finite element method 10
2.1.2. Simulation model and optical properties calculation in *COMSOL Multiphysics* 14
2.2. Plasmon-mediated chemical reactions 16
2.2.1. Mechanism of plasmon-mediated chemical reactions 16
2.2.2. Selectively controlling photocatalytic reactions *via* nonthermal effects 18
2.3. Model reaction system: methylene blue N-demethylation reaction 21
2.4. Real-time characterization of light-driven reactions 23
2.4.1. Real-time *in-situ* Raman spectroscopy 23
2.4.2. Quantitative analysis of the reaction product generation and yield calculation 26
Chapter 3. Hybridized resonance modes of light-driven reactions 29
3.1. Optical design of hybridized metasurfaces with Au nanoparticles coupled to a Fabry-Pérot cavity 29
3.2. Nanofabrication of Au NP-cavities 36
3.2.1. Fabrication of Au NP-cavities 36
3.2.2. Analysis of disordered Au nanoparticles 37
3.3. Optical and catalytic characterization of Au nanoparticle-cavities 41
3.3.1. Tunable optical properties of Au NP-cavities 41
3.3.2. Au NP-cavities in controlling MB reaction yield 44
Chapter 4. Morphology of metasurfaces for light-driven reactions 50
4.1. Design of polarization-dependent metasurfaces 50
4.1.1. Elliptical Au-TiO_2 nanopillar arrays 50

4.1.2. Simulation of Au-TiO_2 nanopillar arrays and parameter design 52
4.2. Nanofabrication of elliptical Au-TiO_2 nanopillar arrays 55
4.3. Optical and catalytic characterization of Au-TiO_2 nanopillar arrays 59
4.3.1. Polarization-dependent optical properties 59
4.3.2. MB reaction yield control on a single metasurface configuration 62
Chapter 5. Phase-change material in light-driven reactions 68
5.1. Background of phase-change materials 68
5.1.1. Phase-change material principles 68
5.1.2. Thermal switching of Sb_2S_3 thin films 70
5.1.3. Optical properties of amorphous/crystalline-Sb_2S_3 73
5.2. Integrating Au nanodisk arrays on an Sb_2S_3 cavity 76
5.2.1. Design tunable metasurface with Au ND coupled Sb_2S_3 cavity 76
5.2.2. Fabrication of Au ND arrays on Sb_2S_3 cavity 79
5.3. Optical and catalytic manipulation of Au nanodisk-Sb_2S_3 cavity 83
5.3.1. Tunable optical properties of Au ND-Sb_2S_3 cavity 83
5.3.2. Yield Control of MB degradation reaction 86
5.3.3. Temperature-dependent MB degradation and selective catalysis enhancement 88
Chapter 6. Summary and Outlook 92
6.1. Summary of metasurface strategies in light-driven reaction manipulation 92
6.2. Light-driven reaction manipulation potential in multibranched reaction system 97
Abbreviations 100
Bibliography 102
Curriculum vitae 117
Publications 119
Ehrenwörtliche Erklärung 120
Appendices 121

Chapter 1. Introduction

1.1. Introduction of light-driven reactions

Capturing solar energy and storing it as chemical fuels offers a promising pathway to meet both present and future energy demands[1]. With rising global energy consumption, the traditional energy industry faces challenges, such as significant price fluctuations, highlighting the necessity of improving solar-based renewable energy, an abundant and virtually limitless resource[2]. To meet the projected annual global energy demand of 25 - 27 TW by 2050, harnessing solar energy with a 10% conversion efficiency over just 0.3% of Earth's land surface would be sufficient[2]. Especially in the energy supplying of shipping, future fuels are expected to meet the energy demand set by the International Maritime Organization and achieve zero-emissions in the maritime industry[3]. Various renewable energy sources are being considered in this area, such as fuel cells, hydrogen or blue ammonia, which can be synthesized and produced by converting chemical energies.

In photochemistry, solar energy can be converted into usable energy and stored as high-energy chemical products through light-driven reactions[4–6], tracing back to the pioneering work of Honda and Fujishima in 1972. By splitting water, hydrogen fuel was generated using sunlight with a titanium dioxide (TiO_2) photoanode in an electrochemical cell[7]. Similar to the products of natural photosynthesis (carbohydrates product generation), this environmentally friendly method of fuel generation is often referred to as "artificial photosynthesis," which produces energy-storing compounds with net-zero emissions[4]. For example, various organic products can be synthesized through carbon dioxide (CO_2) reduction, mitigating greenhouse gas pollution *via* a sustainable, photo-driven approach[6]. Unlike traditional fossil fuel resources, these renewable fuels address critical environmental challenges by not only reducing CO_2 emissions but also transforming them into valuable products, contributing to efficient carbon capture and storage within the carbon cycle[5,8]. Artificial photosynthesis holds great potential

for supporting the transition to a renewable energy-driven global economy, meeting energy demands in diverse sectors, especially in the hard-to-abate industries, such as mining and shipping[1,2,6]. It not only contributes to global decarbonization goals but also enables the sustainable production of renewable fuels[1,5].

Catalysts play a crucial role in promoting reactions, because their activity determines the efficiency of chemical transformations and the overall performance of solar energy conversion[4]. They typically enhance reaction rates by lowering the activation energy of the rate limiting step[9], for example, by polarizing molecules or altering bond angles, or by increasing reaction probability through surface engineering[10,11]. Photocatalysis activates or accelerates reactions by harnessing solar energy and was initially dominated by semiconductor materials[12], such as TiO_2. When illuminated with photons of energy greater than the material bandgap, charge carriers are photoexcited from the valence band (VB) to the conduction band (CB) of the semiconductor. These carriers then diffuse to unoccupied molecular orbitals of surface absorbers, where they participate in reduction or oxidation reactions[13]. However, the intrinsic bandgap of semiconductors restricts excitation wavelength primarily located in the ultraviolet (UV) range[1] which represents only a small fraction of the solar spectrum. In addition, the material thickness is constrained by a 'trade-off' relationship between light absorption and the recombination rate of photogenerated electron-hole pairs, both factors influencing the conversion efficiency[14–16].

Plasmon-mediated photocatalysis offers a pathway to overcome these challenges by enabling strong interactions with electromagnetic (EM) radiation through plasmonic excitation[17,18]. The electronic bands overlap in energy across the reciprocal space, allowing for broadband absorption, extending the effective resonance wavelength of semiconductors to cover a wide range from the UV to the near-infrared (NIR) region[9,19]. For example, metals such as gold and copper which are commonly applied in plasmonic-assisted catalysis, can collectively excite electrons primary on surface to oscillate. It is a phenomenon known as surface plasmon resonance (SPR), which significantly enhances solar energy conversion efficiency[17]. SPR plays a crucial role in concentrating incident light into nanoscale volumes and gives rise to two key effects: surface plasmon polaritons (SPPs), which propagate energy along a metal-dielectric interface, and localized surface plasmon resonances (LSPRs), which confine electron oscillation and assists in the transfer of photons and energetic charge carriers into the surrounding environment. Moreover, LSPRs can accelerate photochemical transformations by

inducing photothermal effects, enhancing the localized near-field further and generating energetic carriers that interact with molecules[18]. These effects have been integrated into applications such as photoheaters[20], photodetectors[8,21], and, most relevant to this thesis, photochemistry, where optical near-field effects are engineered to enhance reactivity. Compared with semiconductor-mediated photocatalysis, plasmon-induced processes sacrifice the long lifetime of excited carriers. However, this drawback is offset by the large number of mobile carriers that oscillate coherently, collectively constituting plasmonic excitations under continuous illumination[9]. Furthermore, both the resonance wavelength and the intensity of the LSPR can be tuned through morphological engineering of metallic nanostructures, enabling effective responses across the full solar spectrum or tailoring wavelength-dependent properties.

Most photosynthesis involves complex, multi-step reaction pathways with numerous intermediates, such as the conversion of CO_2 into energy-dense hydrocarbons[2] or the biofuel synthesis of advanced alcohols and esters[22,23]. Selectivity is crucial in multibranched reactions, which involve multiple steps with various competitive intermediates branching into different pathways[13]. Enhancing or suppressing particular intermediate steps can either promote desired pathways or prevent side reactions, which is both crucial to ensure an effective production of target products and enable a large-scale renewable fuel production[24]. Recent studies have demonstrated the potential of plasmonic metasurfaces to promote particular reactions[8], thereby enhancing catalytic activity and improving the yield of high energy density products—an area of growing importance in sustainable energy conversion, such as carbon mitigation research[13,24]. However, recent studies indicate that the catalysts involved can undergo continuous structural reconstruction under practical operating conditions, leading to challenges in interpretations of the active sites and reaction mechanisms in multibranched reductions. Additionally, current analytical techniques face challenges in effectively monitoring multi-pathway intermediates in real-time[25].

To demonstrate the selectivity strategy of resonance-driven reactions, plasmon-mediated dye degradation can be employed as a model reaction, given its well-studied organic reaction mechanism and potential products, which has been shown to be driven by plasmon-assisted photocatalysis[26]. In such optical resonance-driven reactions, LSPR can be tailored through morphological engineering of metasurfaces to selectively match the energy of specific chemical bonds or unoccupied adsorbate states, manipulating the reaction conversion rate[4,27]. Furthermore, product generation rates can be monitored in real-time using approaches such as

surface enhanced Raman spectroscopy (SERS)[4,28] or X-ray diffraction (XRD)[9], Fourier transform infrared (FTIR) measurements *et al*. These methods provide strong evidence for understanding the contribution of tunable plasmonic resonances to catalytic performance and highlight the potential for finely tuning reactions to favor specific pathways while suppressing undesirable byproducts, enabling high selectivity in complex, multibranch photocatalytic systems[29–31].

1.2. Plasmonic metasurfaces in light-driven reactions

Optical metasurfaces have garnered significant attention as a promising platform for artificial photosynthesis[32–37]. Solar energy is efficiently harvested by these subwavelength structures to support localized optical resonances that concentrate light on the surfaces, enabling catalytic activity[38–40]. Recent advances in nanophotonic have been integrated into photochemical applications to demonstrate optical resonance-driven chemistry, particularly through plasmonic[10,30] and hybrid nanostructure configrations[35,41]. Plasmonic-based metasurfaces catalyze resonance-driven reactions through LSPRs[26]. In this process, incident EM waves within a specific wavelength range excite collective oscillations of conduction electrons within metallic nanostructures, generating intense EM field enhancement, commonly referred to as *"hot spots"*, on the metal surface. During the decay process, these resonances effectively generate photo- or thermally induced energetic carriers or photons that transfer to reactant molecules to drive photocatalytic reactions[42].

Optical properties of metasurfaces strongly dependent on their geometric configurations and material compositions, resulting in a high tunability, which is an advantageous feature for controlling photocatalytic reactivity[43]. Tunable optical properties of metasurfaces are, thus, a critical strategy for tailoring their resonant behavior, enabling precise control over resonance wavelength and intensity[44,45] and offering opportunities to manipulating optical energy transfer at the nanoscale[31]. Various approaches can be employed to tailor the optical properties of plasmonic metasurfaces, such as hybridization of resonance modes, geometric morphology engineering, material phase switching *et al*. Advanced metasurface designs are applied to promote the conversion rate, with effectively collecting solar energy or providing energetic carriers and photons.

Plasmonic nanostructures have been employed to enhance the conversion efficiency of photocatalytic reactions with highly effective solar energy harvesting[19,32,46]. Optically resonant

structures enhance absorption, capturing light effectively across a broad range of wavelengths that can cover the full solar spectrum, from UV to visible and into the NIR region, improving catalytic activity. For example, Xu *et al*. combined multiple periodic arrays of Au nanoparticles (NPs) into a single planar superlattice and integrated it into photoelectrochemical (PEC) anodes[46]. Multiple plasmonic resonances are obtained that collectively provide broadband light absorption, demonstrating a significant improvement in photocurrent density of about 260% compared to a bare CdS film. Hybrid metasurfaces can also be used to extend the active wavelength region by combining plasmonic and semiconductor materials into hybrid structures. For example, Li *et al*. demonstrated broadband UV-NIR absorption using hematite nanorods coupled with gold nanoholes[19]. Local field enhancement from LSPRs matched the hematite band edge, enabling plasmon-induced resonant energy transfer (PRET) that boosted sub-bandgap absorption and yielded a ~ten-fold increase in photocurrent at 0.23 V vs. Ag|AgCl under simulated solar light in PEC water splitting. Beyond wide bandwidth, the absorption of metasurfaces can further be enhanced by collecting light at wide angles[47], with all polarizations[46], and through efficient electron excitation[35,41,48], effectively promoting the reaction with significant resonance strength.

Additionally, to target specific reactions, wavelength dependent optical properties, such as the plasmonic resonance, can be tailored to matched the molecular resonance energy[26], effectively injecting the carriers into the unoccupied molecular orbitals with diverse effects to promote the reactions. For example, Shi *et al*. developed Au NPs/TiO_2/Au-film structures to enhance plasmon-induced water-splitting reactions. With appropriate thickness of the TiO_2 cavity, the resonance of Au NPs can be enhanced *via* strong coupling with the cavity mode, resulting in dual peaks in the absorption spectrum. This effect broadens the resonance wavelength range and effectively enhances hydrogen (H_2) evolution[35]. Morphology tailoring of metasurfaces also shows promise for enhancing specific photocatalytic reactions by supporting spectrally matched resonant modes. For example, Dutta *et al*. designed a sandwiched gold-hematite-gold nanodisk (ND) structure that extends the effective wavelength range for photoelectron generation beyond the bandgap of hematite, facilitating the plasmon-induced generation of hot electrons in the NIR range[41]. Furthermore, Hu *et al*. developed a TiO_2-based metasurface relying on optical bound states in the continuum (BIC), demonstrating broad spectral tunability. By adjusting the scaling factor, tilting angle, and material composition of the nanostructure, they significantly promoted photocatalytic activity for Ag^+ reduction[29]. These studies

demonstrate that plasmonic metasurfaces hold the potential to target driving photocatalytic reactions *via* LSPRs and selectively promote specific photochemical reactions by tuning the resonance strength to enhance the population of excited or injected electrons into unoccupied molecule orbitals of reactants.

Further studies have explored the ability of metasurfaces to achieve selectivity in photochemical processes by tailoring their optical properties. For instance, theoretical work by Wang *et al*. provided valuable insights into designing polarization-sensitive systems using chiral plasmonic nanostructures[31]. These nanostructures exhibit significant chiral asymmetry in optical absorption and hot electron generation between left- and right-circular polarizations, demonstrating their potential for driving photochemical reactions. Furthermore, metasurface designs with high tunability can enable active control over reaction rates. For instance, Yuan *et al*. employed Si_3N_4 nanocubes coated with Ni NPs that support polarization-dependent quasi-BIC modes, modulating the reactivity of the H_2 dissociation reaction[36]. Their optical properties were tuned to activate and enhance specific photochemical reactions. To advance the selective control of photocatalytic reactions, it is essential to extend the functionality of plasmonic metasurfaces to enable both enhancement and suppression of reactivity.

In this thesis, I theoretical and experimental develope strategies for manipulating photocatalytic reaction reactivity with various tailorable metasurface designs. The plasmonic resonance strengths are designed to be tuned at target wavelengths through hybridizing resonance modes, engineering geometric morphology, and switching material phases, demonstrating the effective and dynamic tailoring of plasmonic effects to selectively drive photocatalytic reaction reactivities. A real-time *in-situ* catalysis characterization approach is developed based on SERS, tracking and investigating the time evolution of product yields. The relationship between optical and catalytic performance is analyzed, correlating the plasmonic resonance and reaction reactivities, and highlighting a plasmonically tailored approach for photocatalytic reaction control. Desired product yields can be selectively controlled by modulating plasmonic resonance to achieve either enhancement or suppression of reactions, which is crucial for further promoting target pathways or suppressing byproducts to investigate the potential in multibranched reaction system.

In Chapter 2, the basic principles of employing plasmonic metasurfaces for photocatalysis are introduced, with a focus on plasmon excitation and decay for photochemical transformation.

For metasurface design, this chapter contains the simulation approach of determining the electric field distribution with the solution of the wave equation and is linked to the plasmonic resonance of metasurfaces. Furthermore, catalytic characterization is demonstrated using a model reaction, methylene blue (MB) degradation, illustrating real-time monitoring of the reaction process.

In Chapter 3, a tunable metasurface is designed *via* resonance mode hybridization between plasmonic resonance and Fabry-Pérot (F-P) resonance. In Au NP coupled cavities, the strength of the plasmonic resonance is tailored by peak shifts of the F-P resonance under strong coupling conditions, induced by increasing cavity thickness. Absorption at the target wavelength, corresponding to the resonance of the reactant molecules, is tuned across samples, effectively suppressing, enabling, or enhancing the reaction product yield.

In Chapter 4, to eliminate the influence on sample variations in catalytic performance, a single metasurface is designed and investigated to support polarization-dependent optical properties. An asymmetric elliptical Au-TiO_2 nanopillar array modulates the plasmonic resonance, enabling continuous control of the reaction yield by switching the polarization state of the incident light. The correlation between optical and catalytic properties is systematically analyzed, highlighting the potential of modulating in desired product yields.

In Chapter 5, I further integrate a phase-change material, antimony sulphide (Sb_2S_3), as a cavity coupled with Au NDs array. The plasmonic resonance is tuned through refractive index changes between the amorphous and crystalline phases, inducing a switchable catalytic property in a model reaction, MB degradation. Moreover, tunability can be achieved at several wavelengths, which can be considered to catalyze multiple aligned reactions, demonstrating potential of selective enhancement and suppression across various reactions.

In Chapter 6, three tunable metasurfaces are summarized and discussed, highlighting their ability to modulate photocatalytic reactivity in terms of tunability, efficiency, and dynamic switching. Finally, the potential for achieving selectivity in multibranch reactions is introduced, building on previous manipulation approaches to resonance-driven reaction.

Chapter 2. Principles of metasurface modelling and light-driven reactions

2.1. Optical simulation with finite element method

2.1.1. Fundamental principles of electric field simulation and finite element method

A metasurface comprises of periodic or random nanostructures with subwavelength features capable of interacting with light and supporting a variety of optical resonance modes, including metallic[49], dielectric[50,51], and hybridized[52] modes. Within such nanoresonators, diverse near-field effects can be harnessed to spectrally tune the resonance, modulate the localized EM field, or enable effects phenomena such as surface lattice resonances[37,53,54]. Morphological engineering of metasurfaces offers a versatile approach for tailoring optical properties to achieve multifunctionality in a wide range of photonics applications including photochemistry.

EM field simulation is an essential tool for predicting both near-field and far-field optical responses, guiding nanostructure design, and further evaluating photocatalytic performance[4]. The finite element method (FEM) is a widely employed frequency-domain computational technique that provides solutions with high geometric adaptability and accurate static-field[54]. In this work, the optical properties of plasmonic-based nanostructures were simulated using FEM implemented in *COMSOL Multiphysics*, with systematically varying metasurface parameters to optimize for specific light-driven reactions.

As a frequency-domain simulation technique, FEM is based on the time-harmonic Maxwell's equations, which describe the EM fields oscillating at angular frequency $\omega = 2\pi f$. The equations are expressed as follows:

$$\nabla \times \mathbf{H} = \mathbf{J} + j\omega\varepsilon\mathbf{E} \tag{2.1}$$

$$\nabla \times \mathbf{E} = -j\omega\mu\mathbf{H} \tag{2.2}$$

$$\nabla \cdot (\mu\mathbf{H}) = 0 \tag{2.3}$$

$$\nabla \cdot (\varepsilon\mathbf{E}) = \rho \tag{2.4}$$

where **H** and **E** denote the magnetic and electric field, respectively; **J** and ρ represent the electric current density and charge density; and ε and μ are the permittivity and permeability of the medium. The permeability is given by $\mu = \mu_r\mu_0$, where μ_0 is the permeability of free space and μ_r is the relative permeability of the material[55]. For most optical materials, μ_r can be approximated as 1.

The permittivity ε is expressed as $\varepsilon = \varepsilon_r\varepsilon_0$, where ε_0 is the permittivity of free space, a fundamental constant, and ε_r is the relative permittivity of the medium. The relative permittivity ε_r is a key material parameter that determines the electric field distribution and generally varies with the frequency of the incident light. To simplify Equation (2.1), the complex permittivity is introduced and defined as follows:[56]

$$\varepsilon_c = \varepsilon - j\frac{\sigma}{\omega} = \varepsilon' - j\varepsilon'' \tag{2.5}$$

where σ is the electrical conductivity of the medium. The real part of the complex permittivity, $\varepsilon' = \varepsilon_r\varepsilon_0$, corresponds to the conventional permittivity of the medium, while the imaginary part, $\varepsilon'' = \frac{\sigma}{\omega}$, characterizes material losses[57]. The complex refractive index, $n_c = n + i\kappa$, commonly provided as material parameters in simulation, is related to the complex permittivity by:

$$\varepsilon' = n^2 - \kappa^2 \tag{2.6}$$

$$\varepsilon'' = 2n\kappa \tag{2.7}$$

Accordingly, Maxwell's equations for isotropic media can be simplified as:

$$\nabla \times \mathbf{H} = j\omega\varepsilon_c\mathbf{E} \tag{2.8}$$

$$\nabla \times \mathbf{E} = -j\omega\mu_0\mu_r\mathbf{H} \tag{2.9}$$

$$\nabla \cdot (\mu_0\mu_r\mathbf{H}) = 0 \tag{2.10}$$

$$\nabla \cdot (\varepsilon_0\varepsilon_r\mathbf{E}) = \rho \tag{2.11}$$

The wave equation can be derived by combining Ampère-Maxwell's law in Equation (2.8) with Faraday's law in Equation (2.9), expressed as

$$\nabla \times \frac{1}{\mu_r}(\nabla \times \mathbf{E}) - k_0^2(\varepsilon_r - \frac{j\sigma}{\omega\varepsilon_0})\mathbf{E} = 0 \tag{2.12}$$

where k_0 represents the wavenumber in free space defined as $k_0 = \frac{\omega}{c} = \omega\sqrt{\mu_0\varepsilon_0}$, and c is the speed of light in vacuum. For a source-free region ($\sigma = 0$), Equation (2.12) simplifies to[56]:

$$\nabla \times \frac{1}{\mu_r}(\nabla \times \mathbf{E}) - k_0^2 \varepsilon_r \mathbf{E} = 0 \tag{2.13}$$

In vacuum, one of the solutions of the wave equation (2.13) takes the form of plane wave

$$\mathbf{E} = \mathrm{E}_0 e^{ik_0 \boldsymbol{z}} \tag{2.14}$$

where k_0 is the wavenumber in free space and $\boldsymbol{z}$ is the propagation direction. E_0 defines the amplitude of the electric field. When the light propagates in a material with a complex refractive index $n_c = n + i\kappa$, the plane wave solution becomes

$$\mathbf{E} = \mathrm{E}_0 e^{ik_0 n \boldsymbol{z}} e^{-k_0 \kappa \boldsymbol{z}} \tag{2.15}$$

The wavelength in the medium is reduced to $\lambda = \lambda_0/n$, which reflects the reduction of the speed of light and reshapes the distribution of the field. The imaginary part of the refractive index, κ, determines the attenuation of the field and is used in the calculation of material absorption. The refractive index is crucial both for describing the near-field distribution and for determining the far-field parameters of an optical material.

The metasurface has a nanoscale structure with dimensions comparable to the wavelength of light, which affects the distribution of the electric field, due to the refractive index difference between materials. By engineering the nanostructure morphology, it becomes possible to manipulate the amplitude, phase, and polarization of the EM wave. For example, F-P resonance can be supported in a thin film cavity due to the high reflection caused by the refractive index contrast at the material interfaces, and constructive interfere the light at the peak wavelength depending by the cavity thickness. Similarly, plasmonic resonance can be supported by a metallic metasurface, arising from the interaction of light with free electrons in the metal. The plasmonic resonance wavelength is also significantly influenced by the nanostructure geometry, including size, shape, and arrangement, which are critical factors in plasmonic metasurface design. In photochemistry, plasmonic resonance offers an effective means of enhancing the energetic electron population available to reactant molecules, which is the key principle of this work and will be described in detail in Section 2.2.

Since the geometry of metasurfaces is commonly complex, solving the wave equation with traditional analytical approaches is challenging[56]. FEM is employed to simulate the electric field in metasurfaces. With this method, the complex geometry of the structure is discretized

into a set of tetrahedral mesh elements, as illustrated in Figure 2.1. The Galerkin method is employed to transform the continuous wave equation in Equation (2.12) into its discrete integral form for each mesh element[58,59]. The approximate electric field distribution is expressed using basis functions,

$$\mathbf{E} = \sum_{j=1}^{n} K_i \, \mathbf{E}_j \tag{2.16}$$

which are substituted into the discretized integral wave equation. The resulting system of assembled linear algebraic equations is then solved subject to the appropriate boundary conditions[60]. The mesh element size strongly influences the accuracy of the simulation; as recommended by the software, it should not exceed λ/n. Tetrahedral elements are particularly advantageous for three-dimensional simulations due to their high adaptability in representing complex geometries[61], making them well-suited for circular and other intricate metasurface structures[62].

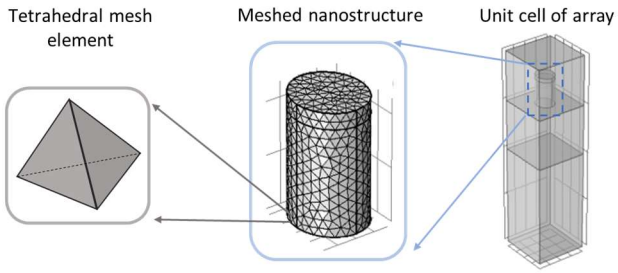

Figure 2.1 Unit structure modeled in *COMSOL Multiphysics* and the corresponding meshed nanostructure using tetrahedral elements.

Several boundary conditions were applied to the simulation model to accommodate different metasurface morphologies. For periodic array structures, a single unit cell was constructed in the software, and periodic boundary conditions were imposed. Under these conditions, a periodic integral equation is used to solve for the electric field distribution using Floquet modes, which replicate the EM boundary and radiation conditions periodically across the unit cell[55]. In the simulation, periodic boundary conditions were assigned to all surrounding lateral surfaces of the unit cell, with the wave vector (**k**-vector) defined by the corresponding periodic ports, for example, from the left face to the right face of the structure[63]. This approach yields the electric field distribution corresponding to an infinite periodic array. In addition, other boundary types can be applied to represent specific physical constraints of the model, such as

perfect electrical conductor ($\mathbf{n} \times \mathbf{E} = 0$), perfect magnetic conductor ($\mathbf{n} \cdot \mathbf{E} = 0$) among others[64]. At the edge of each meshed element, the boundary condition is considered as perfect electrical conductor, where tangential electric field is continuous.

In the simulation of absorbers, the perfectly matched layer (PML) is implemented as an artificial medium with additional degrees of freedom in its electric and magnetic conductivities. This design produces an interface that is completely non-reflective and exhibits high absorption[64]. Although the PML is a purely mathematical construct[55], it provides an effective strategy for modelling thick metasurface substrates on the millimeter scale. In this approach, the substrate is divided into two layers: a conventional material layer placed above the PML. At the interface, all light enters the PML, where it is gradually absorbed, effectively reproducing substrate absorption while reducing the required layer thickness and accelerating computation.

COMSOL Multiphysics can also simulate metasurfaces with non-periodic nanostructures. For example, a single nanostructure can be enclosed within a PML to analyze the near-field enhancement[65] of a resonator without the influence of periodic mode coupling. This method enables the distinction between the intrinsic resonance modes of an individual structure and the inter-coupling effects among multiple structures[49,66]. Furthermore, random nanoparticle arrangements can be simulated by importing morphologies directly from scanning electron microscopy (SEM) or atomic force microscopy (AFM) images[67] as shown in Appendix 1, allowing for the reproduction of experimentally fabricated geometries. This approach enables precise estimation of optical properties based on the actual nanostructure shapes, in contrast to modelling relying on statistically average parameters. However, in most cases, the latter approach is favorable with view to computational times.

2.1.2.Simulation model and optical properties calculation in *COMSOL Multiphysics*

In this study, optical simulations using *COMSOL Multiphysics* were conducted following the workflow illustrated in Figure 2.2. As all simulated systems possess periodic structures, the process begins with the construction of the unit-cell geometry within the software according to the design specifications. Key structural parameters are defined as global variables, allowing systematic adjustment during computation. The material properties are specified using the complex refractive index as a function of wavelength, obtained either from literature sources

or from experimental measurements performed using ellipsometry. The material refractive index data applied for the models of this thesis are shown in Appendix 2. And the principle of ellipsometer is introduced in Appendix 3. An interpolation method is employed to determine refractive index values at specific wavelengths. The real part of the refractive index n governs the spatial and spectral distribution of the electric field, while the extinction coefficient κ determines the material's optical absorption.

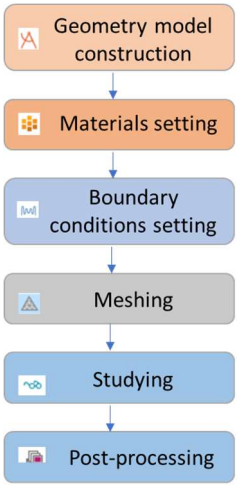

Figure 2.2 *COMSOL Multiphysics* workflow for wavelength-domain EM field simulation.

Additionally, Floquet periodic boundary conditions were applied to all surrounding surfaces forming the periodic array. The incident light was introduced through a port with wave excitation on the top surface of surrounded by the environment air. The polarization of the incident light is defined by the mode field amplitude vectors. For transverse electric (TE) waves the electric field vector is perpendicular to the incident plane, which defines the electrical mode field amplitude vectors as $E_x = 0, E_y = 1, E_z = 0$ for the light propagating in z direction. Similarly, for transverse magnetic (TM) waves the magnetic mode field amplitude vectors are $H_x = 0, H_y = 1, H_z = 0$. The PML is applied as the bottom layer of the substrate to avoid additional reflection at the interface as described above.

Following the model setup, the geometry was discretized into finite tetrahedral elements. The mesh element size was selected for each structure individually, considering its known geometric dimensions, material properties, and minimum excitation wavelength. The simulations were performed over a range of wavelengths to obtain the corresponding electric field distributions. These results were used to visualize the electric near-field enhancement,

absorption and other quantities discussed in later chapters. To investigate the tunability of metasurface morphology, both geometric and material parameters could be accordingly varied with designs, and the resulting optical responses were analyzed as functions of the design parameters. The absorption spectra of materials were calculated from the integrated absorbed power,

$$P_{abs} = \int_{\Omega} Q_{abs} dV \tag{2.17}$$

and the total absorption was determined from

$$A = 1 - T - R \tag{2.18}$$

where R and T are the reflectance and transmittance at the excitation and detection ports, respectively. The near-field and far-field properties are analyzed with the simulation model guides the morphology design of metasurfaces.

2.2. Plasmon-mediated chemical reactions

2.2.1. Mechanism of plasmon-mediated chemical reactions

Metallic-based metasurfaces can effectively harness light at specific wavelength range to support the plasmon resonances which enabling both the spatial and spectral localization of EM wave energy[4]. Precise control of light resonance can be achieved through nanostructured material engineering, which enables tailoring of optical responses in both the far-field and near-field regimes. The conduction electrons in metals can be externally driven by light, supporting resonances at metal/dielectric interfaces, such as surface plasmon polaritons (SPPs) and localized surface plasmon resonances (LSPRs). SPPs are surface EM waves that propagate along the interface between a metal and air/substrate[68]. And LSPRs confinement of a surface plasmon in a nanostructure with the size comparable to light wavelength used to excite the plasmon which can transfer photons and energetic charge carriers into the surrounding environment. In this thesis, we focus on metasurfaces designing that support LSPRs for applications in photochemistry. By integrating LSPRs into resonance-driven reactions, these metasurfaces facilitate light-induced processes through strong spatial confinement of EM waves and high flexibility in resonance engineering *via* appropriately designed geometries[37]. And excited photons and energetic carriers can be transferred into the adsorbed molecules, providing an efficient approach to promote photocatalytic processes.

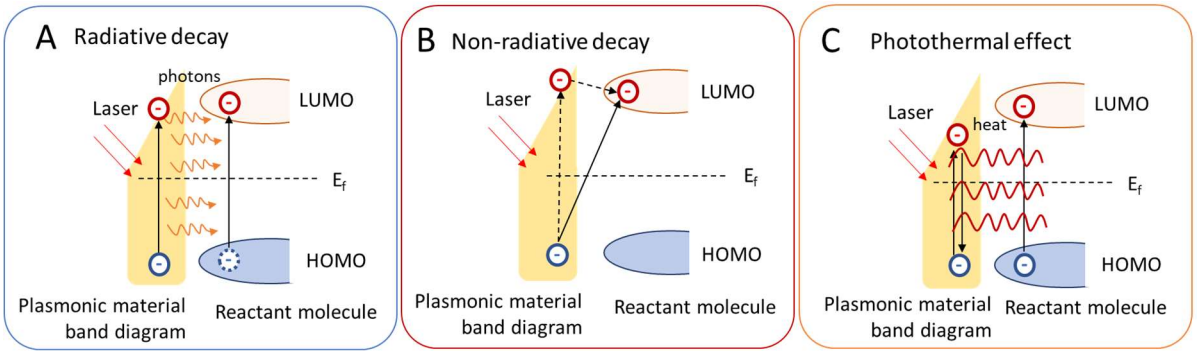

Figure 2.3 Band diagram of the plasmonic metasurface with an adsorbed reactant molecule, illustrating three effects of localized surface plasmon resonance: near-field enhancement (A), hot electron transfer (B), and the photothermal effect (C).

The principle of plasmon-induced photocatalysis are reveals in Figure 2.3. EM waves at specific wavelengths excite coherent oscillations of conduction electrons within metallic nanostructures, increasing to local field enhancement on the metal surface, which are commonly referred to as *hot spots*[42]. These collective electron oscillations amplify the localized electric field surrounding the nanostructures and, during radiative decay[26], transfer energy in photons to the surrounding environment. Reactant molecules adsorbed on the surface, as illustrated in Figure 2.3A, can absorb the emitted photons, excited electrons from the highest occupied molecular orbital (HOMO) to the lowest unoccupied molecular orbital (LUMO) within the molecules. Photoinduced excitations enable or accelerate chemical reactions by increasing the population of energetic electrons available for reaction activation.

The non-radiative decay of plasmonic oscillations can promote electrons (or holes) to energy states exceeding the Fermi level within the plasmonic nanostructure. These energetic charge carriers, referred to as *hot carriers*, exhibit lifetimes on the picosecond scale and are capable of overcoming interfacial energy barriers to inject into the LUMO of proximate molecular adsorbates[42], initiating and enhancing specific chemical transformations[18,69]. Such injection may proceed *via* an indirect pathway (dashed line in Figure 2.3A), in which hot carriers generated within the plasmonic metasurface undergo momentum- and energy-conserving scattering into the molecular orbitals of the adsorbate[4,18,70]. Alternatively, hybridization between the electronic states of the metal and the molecule can facilitate a direct injection mechanism (solid line in Figure 2.3A), wherein hot carriers are transferred into hybridized surface states without an intermediate scattering step[20].

If the energetic carriers are not transferred to acceptor states, they undergo relaxation primarily *via* electron-electron scattering, resulting in localized heating that can also enhance reaction rates[20]. This effect heats up the surrounding environment, producing a temperature increase on the nanosecond timescale[1]. This temperature rise can enhance the collision probability of the active molecules, promoting the dynamic process of the reaction[71]. The spatial distribution of the induced temperature is governed by the geometry of the plasmonic metasurface. This photothermal process is effective over a broad range of incident light wavelengths[72]. In practice, one or more of these mechanisms, near-field enhancement, hot-carrier injection and photothermal heating may contribute to catalyzing a resonance-driven reaction.

2.2.2.Selectively controlling photocatalytic reactions *via* nonthermal effects

Near-field enhancement and hot-carrier generation are classified as non-thermal charge-transfer mechanisms. In contrast to thermally driven effects, these non-thermal pathways in plasmonic photocatalysis enable the selective activation of specific chemical bonds, and allow precise control over catalytic reaction reactivity[26]. Plasmonic metasurfaces interact with incident light within a defined wavelength range, allowing targeted catalysis of specific light-driven reactions. Moreover, the optical properties of a metasurface can be systematically tuned through morphological engineering and material parameter optimization to achieve reactivity manipulation, offering significant potential in selective catalysis across multiple reaction pathways.

In Figure 2.4, two non-thermal effects are engineered to interact with specific light wavelengths to modulate catalytic reactivity. When the plasmonic resonance wavelength aligns with the HOMO-LUMO gap of the molecule, both the re-emitted local electric field intensity and the hot electron generation rate are maximized, increasing the electron population in the LUMO and enhancing the rate of the target resonance-driven reaction[73]. Conversely, if the plasmonic resonance is red-shifted to longer wavelengths, the energetic electrons lack sufficient energy to be directly excited into unoccupied molecular orbitals or to be transferred from the metal, resulting in a reduced energetic electron population and suppression of the reaction. Thereby, the photocatalytic behavior can be finely tuned by engineering the plasmonic resonance wavelength through the design and material selection of the plasmonic metasurface.

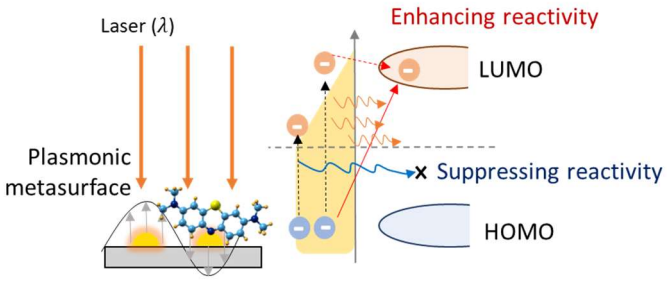

Figure 2.4 Reactivity modulation of a light-driven reaction. The optical properties are engineered to align with the activation energy of the reaction (red and orange lines), determined by the HOMO-LUMO gap of the reactant, thereby enhancing reactivity. In contrast, a mismatch between the plasmonic and the molecular resonance wavelengths suppresses the reaction.

Precise modulation of reactivity can preferentially catalyze the formation of desired end products, achieving selectivity in multibranched reaction systems. Leveraging the two non-thermal effects, plasmonic metasurfaces can be engineered to promote target reaction pathways while simultaneously suppressing competing side pathways, thereby reducing the formation rate of undesired byproducts. Additionally, the tunable optical properties of metasurfaces can be tailored to deliver the precise energy required for specific pathways, enabling dynamic control over product selectivity for advanced applications. However, recent studies have revealed that catalysts may undergo continuous structural reconstruction under practical operating conditions, complicating the identification of active sites and the elucidation of reaction mechanisms in multibranched systems, such as CO_2 reduction[25]. Compounding this challenge, current analytical techniques face significant limitations in real-time monitoring of transient reaction intermediates. To experimentally demonstrate the selectivity strategy in resonance-driven reactions, we focused on clear mechanism model reactions in this study, such as MB degradation, wherein reactivity could be systematically modulated to either enhance or suppress specific light-driven pathways[26]. These model systems can be real-time monitored *via* SERS, enabling direct analysis of the real-time monitored of product formation and providing insight into the underlying reaction dynamics.

Two non-thermal mechanisms can be evaluated using simulated EM fields to analyze the catalytic performance of the plasmonic metasurface. The theoretical foundations, basic equations and more technical details on the simulations are given in the Section 2.1. The near-field enhancement effect is quantified through the normal electric field distribution $\mathbf{E}_{\text{normal}}$ at the surface of the plasmonic nanostructure. The averaged squared electric field enhancement is calculated according to[74]:

$$\left|\frac{\mathbf{E}}{\mathbf{E}_0}\right|^2 = \frac{1}{a^2|\mathbf{E}_0|^2}\int_0^a dx \int_0^a dy|\mathbf{E}_{\text{normal}}|^2 \tag{2.19}$$

where $\mathbf{E}_0$ is the reference electric field and a^2 represents the calculation area. Figure 2.5A presents the results for a cavity-enhanced Au NP model, evaluated at the NP surface. The electric field enhancement occurs at the plasmonic resonance wavelength range of 600 - 700 nm exhibiting wavelength dependence. The localized electric field transfers photons to molecules at the peak wavelength, which drive specific catalytic reactions with matched energies. Furthermore, as shown in Figure 2.5A, the resonance peak wavelength red-shifts with increasing TiO_2 cavity thickness. The effective excitation wavelengths can be precisely and morphologically tailored to manipulate reaction reactivity.

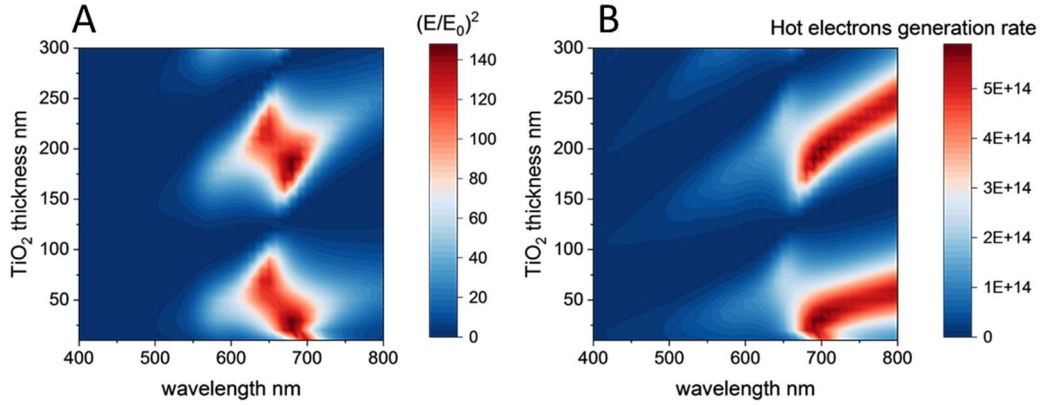

Figure 2.5 Simulated spectra of the electrical near-field enhancement on the Au surface (A) and the hot electron generation rate (B) for the cavity-enhanced Au NP metasurface. The Au NPs have a radius of 14 nm and an interparticle gap of 22 nm.

Additionally, the rate of hot-electron generation is governed by the component of the electric field normal to the NP surface, as described by the following relation:[52]

$$Rate_{high-energy} \approx \frac{2}{\pi^2} \times \frac{q^2 E_f^2}{\hbar} \frac{1}{(\hbar\omega)^3} \int_S |\mathbf{E}_{\text{normal}}|^2 ds \tag{2.20}$$

where q, E_f and $\hbar$ denote the elementary charge, the Fermi energy of gold, and the reduced Planck constant, respectively. The irradiative intensity used in the simulation is determined by the laser parameters employed in the catalytic performance characterization. The effective integral area is defined as a spherical region surrounding the plasmonic nanostructure. As shown in Figure 2.4B, the hot-electron generation rate exhibits a pronounced maximum at the plasmonic resonance wavelength of approximately 700 nm, which are design to aligns with the activation energy requirements of the target reaction. Details of model photocatalytic reaction

will be introduced in Section 2.3. This generation rate can also be tuned by varying the cavity thickness, adjusting the resonance wavelength to optimize catalytic performance.

The photothermal effect can be evaluated by calculating the localized heat generation associated with excited plasmonic nanostructures. The temperature increase of the sample is determined by the plasmon-induced heat generation, expressed as: [26]

$$\Delta T = \sum_{k=1}^{N} \frac{Q_k}{4\pi k_h |\mathbf{r} - \mathbf{r}_k|} \tag{2.21}$$

where Q_k represents the heat power generated *via* Joule heating, which is proportional to the absorption cross-section of the plasmonic nanostructure[75]. The magnitude of the localized temperature enhancement is governed by both the metasurface morphology and the illumination conditions. However, while these parameters effectively determine the extent of the temperature rise, they present limitations in selectively modulating reaction reactivity, as photothermal heating inherently lacks the bond-specific selectivity characteristic of non-thermal mechanisms.

2.3. Model reaction system: methylene blue N-demethylation reaction

To investigate the reactivity modulation capability of plasmonic metasurfaces, we focused on a model photocatalytic system: the N-demethylation of MB, illustrated in Figure 2.6. In this process, cleavage of the C-N bond yields Azure B[76]. Sequential cleavage of additional C-N bonds generates further derivatives, including Azure A and thionine[76]. This reaction can be catalyzed under light irradiation in the wavelength range of approximately 530 - 710 nm[77], as characterized by the photoluminescence spectrum in Figure 2.7A. In plasmonic photocatalysis, MB molecules adsorb onto the gold surface *via* weak dispersion forces[78,79], where they can accept energetic (hot) electrons or energies. And the degradation reactions exhibit a selectivity toward N-demethylation pathways in plasmonic photocatalysis with gold[76], facilitating C-N bond cleavage through a sequential process initialing with the excited electron population into the LUMO, and promoting the formation of reaction products.

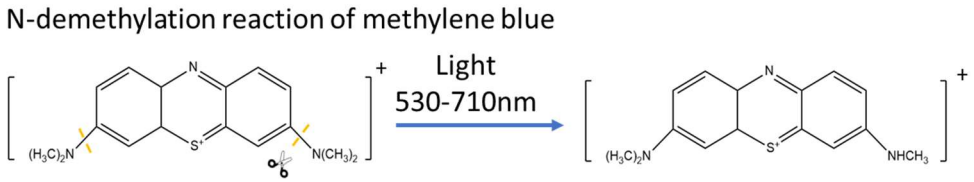

Figure 2.6 Reaction equation for the N-demethylation of MB.

The plasmon-mediated photoreaction mechanisms underlying the N-demethylation of MB have been previously investigated by Fusco *et al*[26]. The potential plasmonic energy transfer channels encompass both non-thermal and thermal effects, including near-field enhancement, hot-electron transfer, and photothermal heating (Figure 2.7B). In previous studies, self-assembled Au NP ensembles with varying radius were employed to examine the catalytic performance across different samples. The findings revealed that catalytic activity reaches a maximum when the excitation laser wavelength, the plasmonic resonance, and the molecular HOMO-LUMO gap are spectrally aligned[4], as discussed in Section 2.2.2.

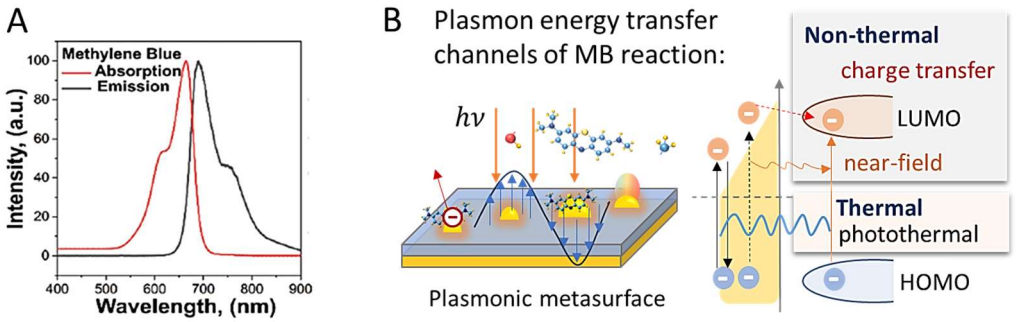

Figure 2.7 A) Fluorescence spectra of MB solution, reproduced with permission from *Ref*[26]. B) Potential plasmon energy transfer pathways involved in the MB reaction, including near-field enhancement (orange), direct charge transfer (red), and photothermal effect (blue).

To investigate the underlying mechanisms of these plasmon-mediated photoreactions, the near-field enhancement was calculated using Equation (2.19), confirming that the intermolecular electron transition exhibits strong agreement with experimental measurements for small NP radius. Subsequently, hot-electron transfer was evaluated by real-time time-domain density functional theory (RT-TDDFT), which demonstrated the active participation of energetic electron injection[26,27,70]. In contrast, the photothermal effect was found to increase the local temperature by no more than 8 °C, a value insufficient to drive the N-demethylation reaction[26,80]. Given these earlier observations, the N-demethylation of MB serves as an

effective model reaction for investigating the reactivity modulation achievable *via* tuning two non-thermal effects with metasurface design engineering.

Additionally, as a widely used dye, both the reaction pathway and the structures of its N-demethylated derivatives have been extensively studied, making MB a well-established model system for mechanistic investigations[79]. Moreover, its absorption band (530 - 710 nm) overlaps with the LSPR of gold, enabling strong resonance excitation in the visible range. Finally, to characterize the catalytic performance in MB degradation, SERS is employed as a standard tool, enabling in situ and real-time monitoring of product formation.

2.4. Real-time characterization of light-driven reactions

2.4.1. Real-time *in-situ* Raman spectroscopy

As a real-time *in-situ* characterization approach, SERS dynamically monitors the product generation rate and chemical processing to evaluate the catalytic behavior of designed metasurfaces. The Renishaw inVia Reflex Raman spectroscopy is employed in our measurements with a diagram of the setup shown in Figure 2.8A. The equipment has three available lasers at 532, 633 and 785 nm. The selected laser focuses on the sample *via* an object lens, to excite the molecules to a virtual energy state. Each chemical bond has unique vibrational frequencies which can be detected as the Raman shift[81] revealing the 'fingerprint' of the molecule[82]. This way, the reactants and products can be detected *via* the specific Raman shift in this measurement. As the molecules are adsorbed on the metal metasurface, the Raman scattering signal is enhanced by its LSPR and collected by the object again. The dichroic mirror splits the laser and the signal and detects the scattering signal spectrum with a spectrometer.

In Raman spectroscopy, the excitation laser wavelength can be selected from 532, 633, and 785 nm to facilitate reactions involving various molecular resonance energies during *in-situ* measurements. Laser power is controlled using neutral density filters, allowing transmittance adjustments from 0.1% to 100%. The measurement area is defined by the laser spot diameter in micrometer scale, which depends on the objective lens magnification. The spectral resolution of a Raman spectrum is determined by the gratings, which have either 1200 or 2400 lines/mm; higher spectral resolution improves peak definition but reduces the spectral range due to the limited size of the detector. For time-dependent measurements, molecular concentrations can be monitored dynamically to track reaction progress, with a minimum time interval of 0.1 s[78].

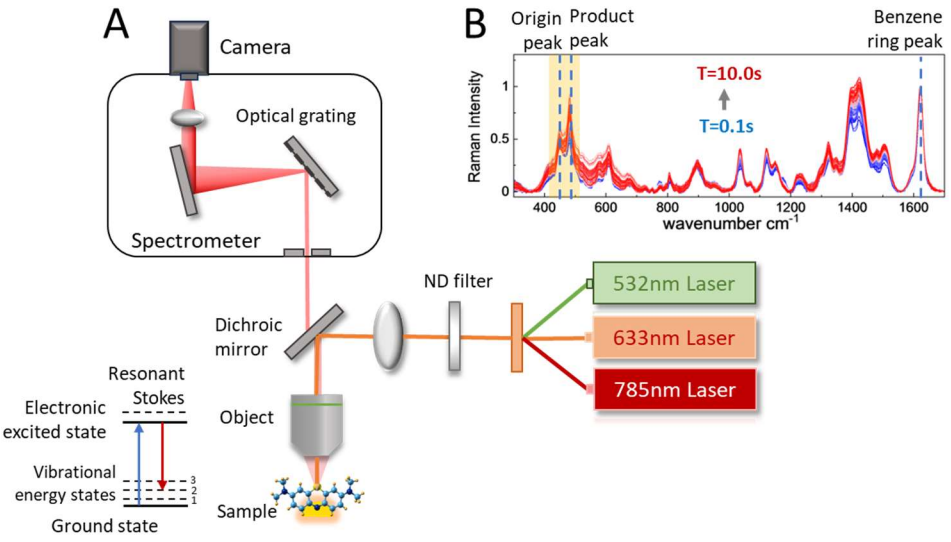

Figure 2.8 A) Diagram of Raman spectroscopy with various laser wavelengths in 523, 633 and 785 nm. The Raman scattering is shown in Jablonski diagram B) Time-resolved Raman spectra of the MB reaction, highlighting characteristic vibrational peaks: 450 cm^{-1} for the reactant, 480 cm^{-1} for the product, and 1600 cm^{-1} for the benzene ring. The excitation laser wavelength was set to 633 nm with a power of 0.68 mW.

Post-processing of collected spectra includes baseline correction and noise reduction to enhance spectral quality. Baseline correction, typically achieved through adaptive methods such as polynomial fitting[83,84], serves to remove substrate contributions and isolate molecular signals. In cases of weak signals where the signal-to-noise ratio (SNR) is low, noise reduction is applied using smoothing algorithms such as the Savitzky-Golay filter[81] to improve SNR. To eliminate the effect of systematic variations between measurements, temporal Raman spectra are normalized to a specific Raman peak.

Figure 2.8B presents the real-time monitoring of the MB N-demethylation reaction *via* SERS, with spectra acquired at 0.1 s intervals over a duration of 10 s. All spectra are subjected to baseline correction and normalized with respect to the 1622 cm^{-1} peak corresponding to C-C stretching in the benzene ring[76], due to its stability during the reaction. The temporal evolution of both the reactant (MB) and its N-demethylated derivatives is detected through specific vibrational fingerprints. At the initial timestep (t = 0.1 s), the Raman spectrum primarily exhibits characteristic vibrational modes of MB, highlighted by the peak at 448 cm^{-1}, which corresponds to the C-N-C skeletal deformation[76]. This peak diminishes as the N-demethylation reaction proceeds, indicative of bond cleavage. Simultaneously, a new peak emerges at 480 cm^{-1}, assigned to the N_{amino}-H skeletal deformation mode of the photoproduct[85,86]. These spectral features facilitate analysis of the reaction kinetics and mechanistic insights under

varying experimental conditions as well as calculating a reaction yield. Further Raman peaks and band assignment of this reaction are also determined from the references[26,76,78] shown in Appendix 4.

The choice of laser wavelength for photocatalysis is guided by the resonance energy of the reactant molecule, MB, as well as the available laser sources for Raman spectroscopy. The absorption and emission spectra of MB in solution, as presented in Figure 2.7, indicate an absorption ranging approximately 530 to 710 nm. Raman spectra were recorded using excitation wavelengths of 532, 633, and 785 nm, each at comparable power levels. The 633 nm laser closely matches MB absorption peak, facilitating effective photocatalysis, as evidenced by the highest Raman signal intensity shown in Figure 2.9A. In contrast, MB absorption at 532 and 785 nm is comparatively low. Under excitation with the higher-energy photons in 532 nm, vibrational features such as the C-C stretching mode in the benzene ring at 1622 cm^{-1} remain discernible; however, changes in the intensity of both reactant and product peaks within the 400 - 600 cm^{-1} range are minimal. Excitation at the lower-energy wavelength in 785 nm yields weaker overall Raman signals, with no discernible peak shifts. Increasing the excitation wavelength constrains the effective spectral range of the spectrometer as shown in the Raman spectra at 785 nm due to limitations imposed by the grating dimensions. Consequently, the photocatalytic performance of MB degradation is wavelength-dependent and optimized at 633 nm excitation wavelength which is selected as the laser source for metasurface characterization.

Additionally, Raman spectra of cavity-enhanced Au NPs were measured under varying laser powers to investigate the influence of the excitation intensity. The intensity of the normalized vibrational peak at 480 cm^{-1}, corresponding to the product concentration, was monitored over 30 s, to track product generation. At a laser power of 0.07 mW, the product peak intensity increased modestly from 0.55 to 0.75, as shown by the transition from blue to red spectra in Figure 2.9B. With increasing laser power, the plasmonic resonance of the Au NPs was enhanced, leading to a more pronounced increase in the product peak intensity and, consequently, greater product formation. Notably, at 0.68 mW, the product peak intensity rose significantly from 0.74 to 1.25, indicating considerable catalytic activity. These results demonstrate that Raman spectroscopy effectively monitors product generation *via* the 480 cm^{-1} vibrational peaks. Furthermore, the observed laser power-dependent catalytic properties highlight the role of the LSPR strength in modulating the photocatalytic degradation of MB.

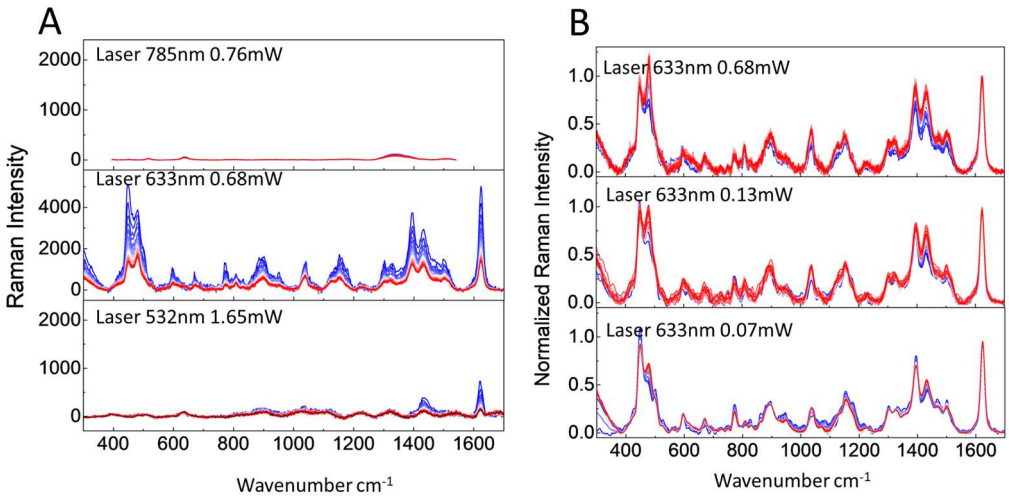

Figure 2.9 Raman spectra of the MB reaction reveal varying reactivity under different wavelengths (A) and laser powers (B) on a Au NP coupled TiO_2 cavity. Laser power ranges from 0.07 mW to 0.68 mW. Spectra were recorded over a 30 s period (from blue to red) with 1 s intervals.

2.4.2.Quantitative analysis of the reaction product generation and yield calculation

Temporal Raman measurements illustrate the concentration evolution of both reactant and product molecules, as shown in Figure 2.10A. Over the 10 s period, the plasmonic metasurface effectively catalyzes the degradation of MB, evidenced by shifts in peak intensities at 448 and 480 cm^{-1}, corresponding to the C-N-C skeletal deformation in MB and the skeletal deformation of the product, respectively. The vibrational peak increases significantly from 0.49 to 1.14 in intensity, as reflected by the color change in Figure 2.10A. Similarly, the degradation of MB is tracked *via* the intensity decreasing at 448 cm^{-1}. Since MB contains multiple C-N-C bonds that are gradually cleaved during the formation of N-demethylated derivatives, the product peak provides a more direct and reliable indicator of degradation progress and product generation rate.

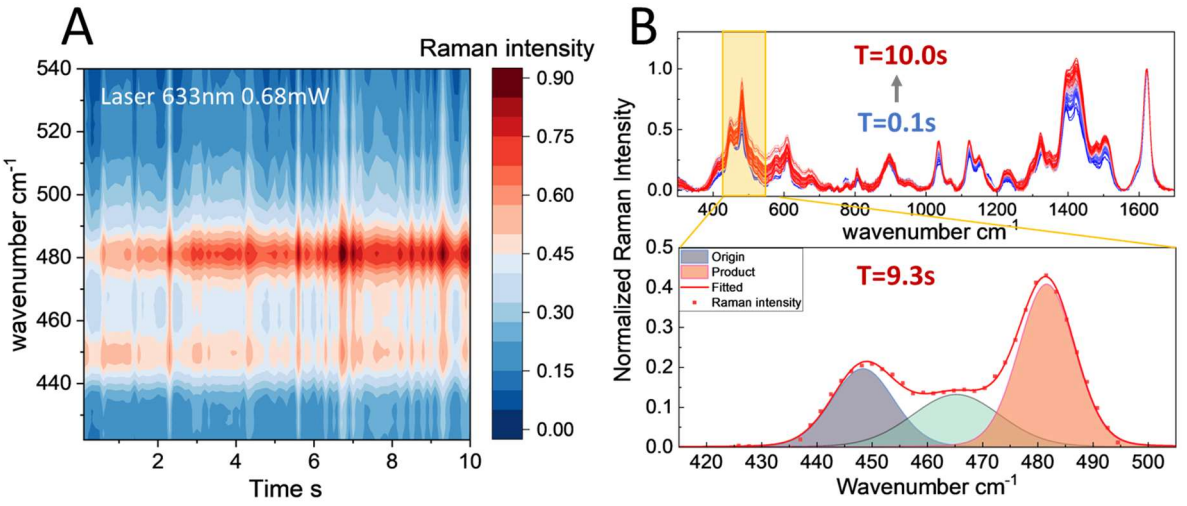

Figure 2.10 A) Time evolution of the reactant and product vibrational peaks over a 10 s period. B) Fitted curves of the reactant (gray) and product (orange) vibrational peaks at 9.3 s for quantitative analysis.

To quantitatively analyze reactivity, the yield of products can be determined by integrating the area under specific Raman peaks, as the vibrational peak correlates with the concentration of molecules[26]. In Figure 2.10B, the Raman spectra within the wavenumber range of 410 - 510 cm^{-1} were fitted using a deconvolution method based on a Gaussian-Lorentzian blend model. The resulting peaks at approximately 445 and 480 cm^{-1} correspond to the original reactant (grey curve) and product (orange curve) of the MB reaction, respectively[26,78]. To optimize the fitting, another auxiliary peak is added at 465 cm^{-1} shown in green curve. The sum of these fitted peaks (red curve) shows excellent agreement with the measured data (red dots), with residual errors below 4%. The product yield of MB reaction, defined as the integrated area of the product vibrational peak at 480 cm^{-1}, reveals the time-dependent generation of the product and is used to evaluate the photocatalytic reactivity.

The time-dependent product yield tracking provides a means to quantify the reaction reactivity during the photocatalytic process. The catalytic performance of plasmonic metasurfaces can be characterized by monitoring product yield over time. Furthermore, kinetic modeling of the reaction from these data allows investigation of the underlying reaction mechanisms and determination of end product generation rate for plasmonic metasurfaces[87]. In this work, tunable metasurfaces subject to reaction reactivity manipulation have been characterized in this approach, investigating the relationship between tunable plasmonic resonance strength and

catalytic properties offering a potential solution in reaction controlling and product yield selectivity.

In summary, this chapter introduces the principles of light-driven reactions and analytical approaches applied to both metasurfaces and catalytic processes. In light-driven reactions, LSPR enhances the electron population in the LUMO of reactant molecules through three mechanisms: near-field enhancement, hot-electron injection, and photothermal effects. To evaluate catalytic performance, we focus on a model system, the N-demethylation reaction of MB, to characterize the activity of tunable optical metasurfaces designed using FEM optical simulations with *COMSOL Multiphysics*. This reaction can be monitored in real-time using *in-situ* Raman spectroscopy, enabling time-resolved analysis of the reaction progress and quantitative determination of product yield.

Chapter 3. Hybridized resonance modes of light-driven reactions

The hybridized resonance has been applied in tuning the optical response of the nanostructure design, enabling control over two non-thermal effects of its LSPR[46]. The plasmonic resonance strength is adjusted by tuning the resonance peak in the strong coupling regime across a group of samples, maximizing or minimizing the value over a wide range[26]. Reaction reactivity varies through both modified near-field effects and hot-electron transfer to enhance and suppress the product generation rate in the model reaction, the MB degradation.

3.1. Optical design of hybridized metasurfaces with Au nanoparticles coupled to a Fabry-Pérot cavity

To manipulate the strength of plasmonic resonances, a series of coupled gold nanoparticle-cavity (Au NP-cavity) nanostructures with tunable cavity thickness are developed. Figure 3.1A shows the configuration of Au NP-cavities, in which reactant molecules are adsorbed onto the surface of plasmonic NPs[88]. Au NPs support LSPR enhancement of the near field and hot-electron generation rate to catalyze light-driven reactions[5]. Since the NPs were prepared *via* a self-assembly process, their sizes and interparticle gaps follow a statistical distribution[89], which directly affects the optical response of the resulting disordered structure. A semi-open optical cavity is formed due to the high reflectance of the metallic mirror film[35], supporting F-P resonances within the anatase TiO_2 cavity layer[52,90]. These resonances can be precisely tuned to specific wavelengths by adjusting the cavity thickness, enabling the modulating from constructive peaks to destructive nodes[34]. The strong coupling regime in the Au NP-cavity arises from the interaction between the LSPR and the F-P mode, which will be further evaluated with optical simulations.

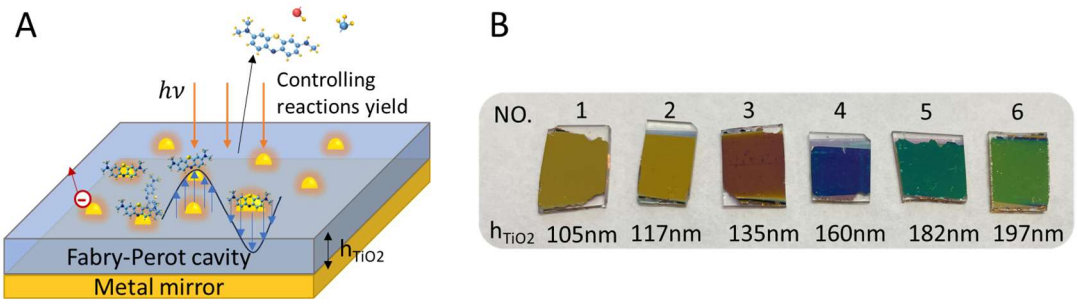

Figure 3.1 A) Schematic of the Au NP-cavity system for light-driven MB degradation, illustrating the photocatalytic mechanism based on two non-thermal effects of LSPR. B) Six Au NP-cavity samples with cavity thicknesses ranging from 105 to 197 nm. Variations in cavity thickness alter the optical properties of the samples, resulting in observable color changes.

Six Au NP-cavity samples with increasing TiO_2 cavity thicknesses are presented in Figure 3.1B, which contains cavities in h_{TiO2} = 105 nm, h_{TiO2} = 117 nm, h_{TiO2} = 135 nm, h_{TiO2} = 160 nm, h_{TiO2} = 182 nm and h_{TiO2} = 197 nm. A distinct color change is observed across the samples, indicating the tunable optical properties arising from the shift of the F-P resonance peak. When the cavity thickness is below 120 nm, the sample color primarily reflects that of the underlying Au mirror layer, with minimal influence from either the TiO_2 cavity or the plasmonic resonance of the Au NPs in visible wavelength. Once the TiO_2 cavity thickness exceeds 120 nm, the optical response becomes governed by the cavity thickness, producing a gradual color transition from red to green. The cavity thicknesses are tailored to span the minimum and maximum of the F-P resonance, enabling coupling of the plasmonic resonance with both the peak and node of the cavity mode[32].

The optical tunabilities of the Au NP-cavity samples were investigated with FEM simulations performed in *COMSOL Multiphysics*. Optical absorption spectra were calculated as functions of both the Au NP parameters[49] and the TiO_2 cavity thickness, and their respective morphological contributions were analyzed. The refractive index of TiO_2 was measured with a J.A. Woollam M-2000D ellipsometer over the 200 - 1700 nm spectral range on a 100 nm thin film, as shown in Figure 3.2. These data were incorporated into the material model of the simulations to determine the F-P resonance wavelength and absorption coefficient. The cutoff wavelength of the imaginary component κ is approximately at 380 nm which further confirms the anatase phase of TiO_2[91].

As introduced in Section 2.1.2, a periodic model is constructed to study the electric field distribution and to calculate related optical properties such as near-field enhancement and far-

field absorptions. Although the Au NPs in the experimental system exhibit a disordered distribution[80], a Floquet periodic nanoparticle model is employed in the simulations with average NP radius and interparticle gaps (refer as the parameters from Figure 3.12). This approach optimizes computational efficiency, and the influence of NP parameter variation are further examined to assess the uncertainty of the simulation methodology[92].

The incident light was introduced through an excitation port with unit power under a linear polarization. Due to the structural symmetry of the sample, the optical resonance remained unchanged upon switching the polarization states. The detection port was assigned the same polarization state. The mesh size was defined according to the geometric dimensions and the minimum characterization wavelength. In particular, the mesh element size for the Au NPs is defined to 1 - 5 nm to precisely describe their semi-sphere shapes in small radii. The simulations are performed over the visible range (400 - 800 nm) with a wavelength step of 5 nm to balance spectral resolution and computational efficiency.

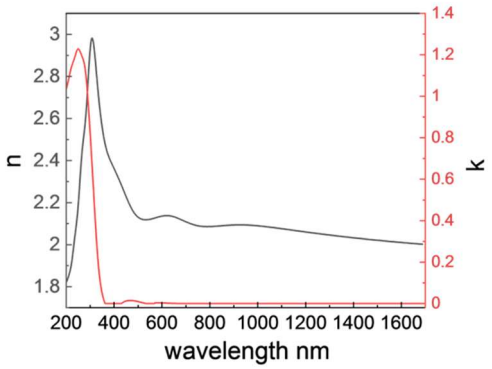

Figure 3.2 Refractive index (n and k) of anatase TiO_2 which measured with ellipsometer from 200 to 1600 nm.

Firstly, Figure 3.3A and B present the simulated absorption spectra of Au NPs as a function of interparticle gap and of TiO_2 nanocavities as a function of thickness, respectively, to examine the LSPR and F-P resonances, respectively. In Figure 3.3A, the plasmonic response of Au NPs is modelled using the NPs with a radius of 14 nm placed on an infinite TiO_2 layer. Floquet periodic boundary conditions are applied to the four surrounding surfaces to generate a periodic array. The interparticle gap varies from 12 to 30 nm, spanning the experimentally observed distribution. The LSPR peak exhibits a slight blue shift as the gap increased beyond 16 nm, stabilizing approximately at 655 nm. This peak wavelength closely matches the target resonance of MB molecules at 633 nm, providing an effective morphological design for

plasmonic catalytic reactions[30]. For samples with an average interparticle gap of 22 nm, the LSPR peak occurs at 659 nm. The bandwidth is also influenced by the interparticle gap, narrowing as spacing increases. However, the maximum absorption of the Au NPs reaches only ~40%, which is expected to add further enhancement *via* mode hybridization with the F-P cavity[90,93].

For the nanocavity model shown in Figure 3.3B, a TiO_2 layer of varying thickness between 10 - 300 nm is deposited on the 200 nm Au mirror. The TiO_2 nanocavity supports constructive F-P resonances at several specific wavelengths, which red-shift with increasing cavity thickness. Due to the bandgap of TiO_2 (E_g = 3.2 eV) and the interband electronic transitions of the Au mirror film[92], absorption is cut off near 550 nm. At the target wavelength, the F-P resonance produces constructive peaks at cavity thicknesses of 40 and 170 nm (corresponding to the first and second F-P resonance orders), and a destructive node at 100 and 250 nm. A considerable absorption tuning is observed from constructive peaks to destructive nodes through cavity thickness variation, which provides an approach expanding the tunability of the plasmonic resonances *via* mode coupling.

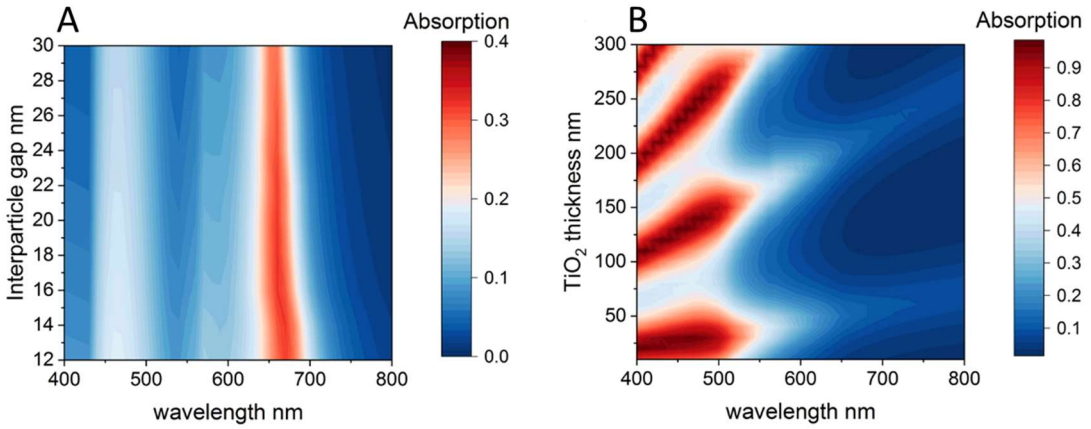

Figure 3.3 Simulated total absorption of LSPR and F-P resonance: A) Au NPs on an infinite TiO_2 layer, with interparticle gaps varying from 12 to 30 nm. b) TiO_2 cavity on an Au mirror layer with increasing cavity thickness from 10 to 300 nm.

To investigate this tunability, the total absorption spectra of Au NP-cavities are calculated as a function of TiO_2 cavity thickness[52]. Figure 3.4 shows how the optical absorption of the hybrid system varies with increasing TiO_2 cavity thickness, while the Au NP parameters remain constant (r = 14 nm, gap = 22 nm). Upon coupling Au NPs to the cavity surface, the total absorption extends into the 600 - 700 nm wavelength range due to the LSPR resonance at 659

nm, which enhances absorption in this spectral region. In Figure 3.4A, the appearance of dual peaks near the overlapped wavelength of plasmonic resonance and cavity resonance reflects energy splitting from the hybridization between the LSPR and F-P modes, a signature of the strong coupling. Overall, the total absorption exhibits oscillatory behavior as the cavity thickness varies over a wide range between 600 - 700 nm.

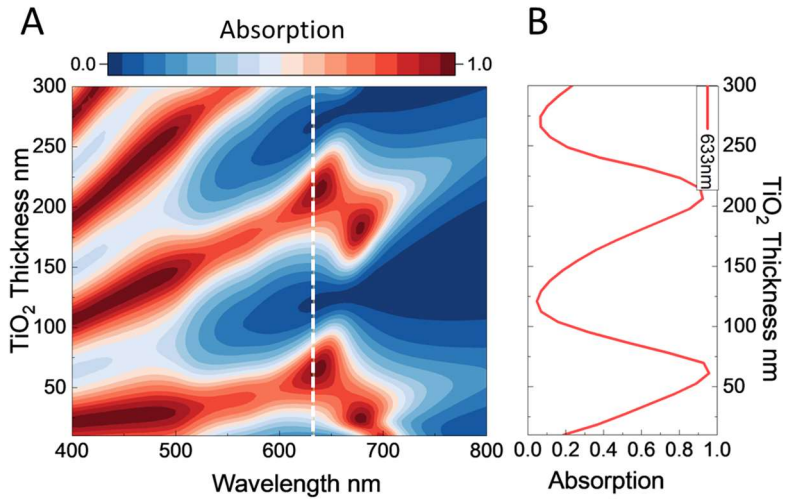

Figure 3.4 Simulated absorption spectra of Au NP-cavities as the function of cavity thickness from 10 to 300 nm in thickness (A), which reveals a dual peak induce by the strong coupling between LSPR and F-P resonance. The total absorption of samples oscillating with cavity thickness at excited light wavelength in 633 nm (B).

The interaction between F-P and LSPR modes can be effectively described using a simple coupled oscillator model[52]. When the LSPR peak spectrally and spatially overlaps with the F-P resonance, strong coupling occurs, and the hybrid mode undergoes energy splitting, resulting in distinct high- and low-energy peaks in the absorption spectrum[35,93]. The upper (ω_{c+}) and lower (ω_{c-}) resonance frequencies of the hybridized mode are determined by the resonance frequencies of the two coupled modes and can be expressed as[93]:

$$\omega_{c\pm} = \frac{\omega_{\mathrm{LSPR}}}{2} + \frac{\omega_{\mathrm{mth-FP}}}{2} \pm \frac{1}{2}\sqrt{\left(\omega_{LSPR}^2 - \omega_{\mathrm{mth-FP}}^2\right) + \Omega^2} \qquad (3.1)$$

where ω_{LSPR} and ω_{mth} are the resonance frequencies of the Au NP plasmonic mode and the m-th order F-P mode of the TiO_2 cavity, respectively, in the strongly coupled system. The coupling strength, Ω, represents the frequency splitting that occurs when the resonance frequencies of the two modes coincide and depends on the NP density in the coupled system, with higher density leading to stronger coupling[52]. This can be expressed as:

$$\hbar\Omega = \sqrt{N/V}\frac{e}{\sqrt{\varepsilon_0 m_e}} \tag{3.2}$$

where N/V denotes the density of dipole moments associated with the Au NP density, and e, ε_0 and m_e are the electron charge, vacuum permittivity, and electron mass, respectively. Consequently, the coupling strength and therefore the absorption spectra is affected by the parameters of the Au NPs[34].

At the target wavelength of 633 nm, corresponding to the molecular resonance (HOMO-LUMO gap) of MB, the cavity resonance wavelength is shifting with increasing cavity thickness. Consequently, the total absorption exhibits oscillatory behavior due to the hybridized resonance, as shown in Figure 3.4B. As the wavelength exceeds the cavity cutoff, the absorption is primarily attributed to the Au NPs and the gold mirror layer. The plasmonic resonance strength of the NPs is effectively tuned by the F-P resonance wavelength through mode hybridization. Guided by these simulations, six samples were fabricated to investigate the hybridization of the LSPR with the second-order cavity mode (m = 2) of the F-P resonance, with TiO_2 thicknesses ranging from 105 to 197 nm. Figure 3.1B illustrates the spectral tunability across the samples, with the reflected color shifting from gold to green. According to the simulations, the total absorption can be tailored from 8% to 90%.

Moreover, the absorption spectra of the Au NP-cavity system are investigated with respect to the NP parameters, specifically in the NP radius and interparticle gap. As shown in Figure 3.5, the coupling strength, Ω, is determined by the frequency difference between dual peaks, influenced by both parameters. With increasing interparticle gap from 10 to 30 nm, the density of dipole moments (N/V) decreases[94], leading to a reduction in the coupling strength from 82 to 32 GHz, as illustrated in Figure 3.5B, and the dual peaks in the absorption spectrum move closer together. Conversely, increasing the NP radius within a small range (6 - 20 nm) reduces the interparticle gap, which enhances the energy splitting from 27 to 93 GHz. However, further increasing in the NP radius results in a reduction in absorption due to stronger radiative scattering[95].

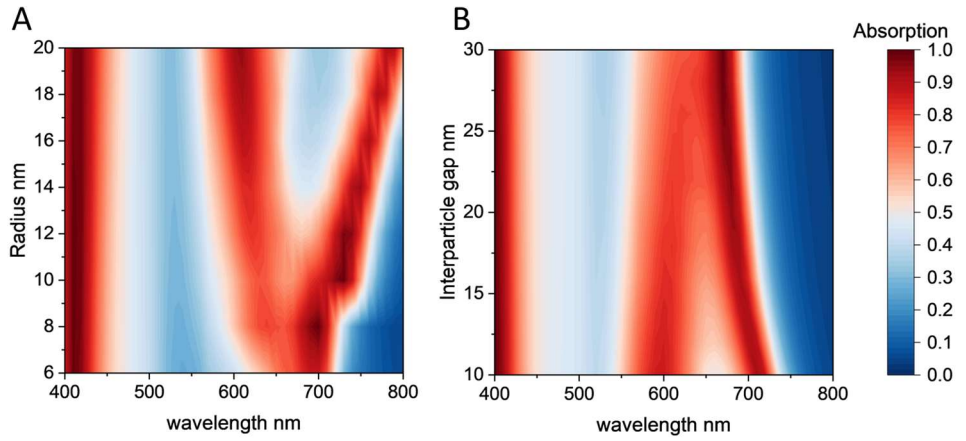

Figure 3.5 Simulated total absorption of Au NP-cavities with varying NP parameters: A) NP radius is shifted from 6 to 20 nm with h_{TiO2} = 200 nm and an interparticle gap of 8 nm. B) Interparticle gap varies from 10 to 30 nm with h_{TiO2} = 200 nm and R_{NP} = 14 nm.

Additionally, this variation in coupling strength is reflected in the absorption spectra for designs with different TiO_2 thicknesses and interparticle gaps at 8, 21 and 30 nm, as shown in Figure 3.6. A similar trend is observed for the splitting energy mode, which decreases with increasing interparticle gaps. The coupling strength obtained in these cases is 39 GHz (gap = 8 nm), 27 GHz (gap = 21 nm) and 17 GHz (gap = 30 nm). This behavior can be explained using Equation 3.2, where a reduction in the density of dipole moments leads to a decrease in the splitting[52,96]. Consequently, disorder in the Au NP array, which locally alters both the interparticle gap and NP radius, results in shifts in the plasmonic resonance wavelength and coupling strength, which might contribute to the differences observed between simulation and experimental measurements.

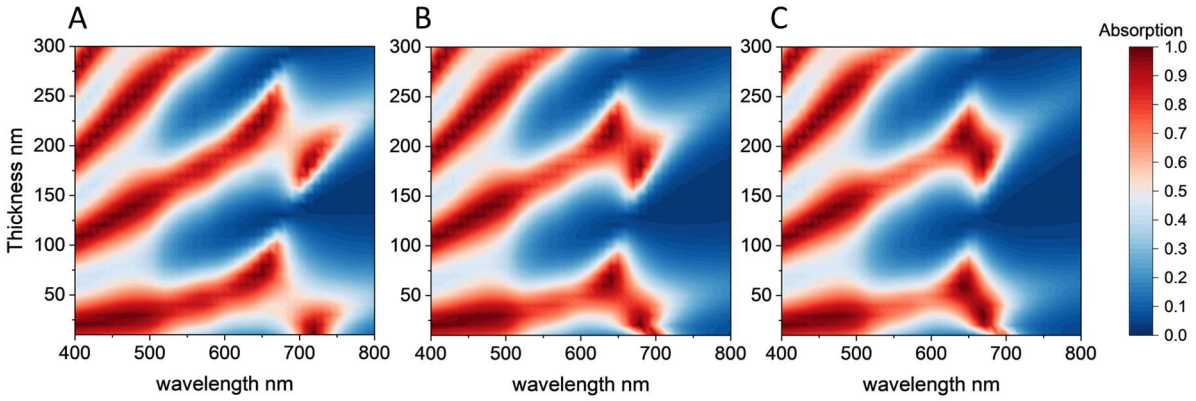

Figure 3.6 Simulated total absorption of Au NP-cavities at different NP gaps to demonstrate the changing coupling strength: A) Au NPs with R = 14 nm and gap = 8 nm; B) Au NPs with R= 14 nm and gap = 21 nm; C) Au NPs with R = 14 nm and gap = 30 nm. The thickness of TiO_2 cavities varies from 10 to 300 nm.

3.2. Nanofabrication of Au NP-cavities

3.2.1.Fabrication of Au NP-cavities

The Au NP-cavities were fabricated following the procedure illustrated in Figure 3.7. The samples were synthesized on 1 mm glass slide substrates, as shown in Figure 3.7A. Au mirror layers were deposited using a Temescal BJD-2000 electron beam (E-beam) evaporator, forming a mirror film with a thickness of 200 nm (Figure 3.7B). TiO_2 nanocavities were subsequently deposited onto the Au mirror by radio frequency (RF) sputtering (Figure 3.7C). The TiO_2 cavity thickness (h_{TiO2}) was precisely controlled by adjusting the sputtering duration, which determined the F-P resonance wavelength.

Thicknesses were measured using ellipsometry, and the results are summarized in Table 3.1. During deposition, the reflective spectrum was collected for both s- and p-polarized light at incident angles of 55°, 65°, and 75°. The measured amplitude ratio and phase shift of the complex reflectance were fitted using a model based on the measured refractive index of TiO_2 as shown in Figure 3.2. The table presents the average values obtained from three measurements at different sample locations. The TiO_2 cavity thickness increased uniformly with sputtering time, exhibiting an average deposition rate of approximately 0.17 Å/s. As the sputtering duration increased from 2 hours to 3 hours and 20 minutes, the TiO_2 cavity thickness increased from 105 to 197 nm, covering the F-P resonance peaks and nodes.

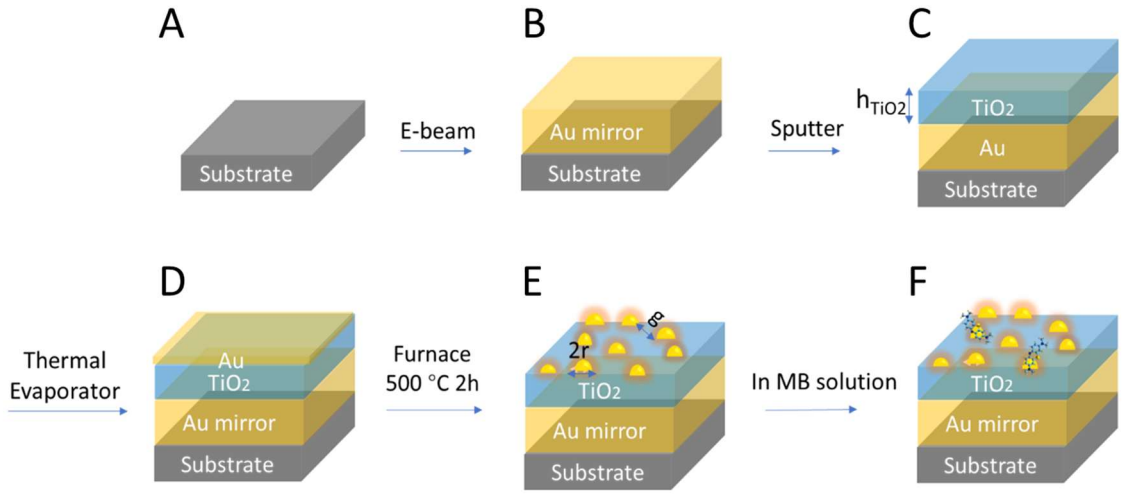

Figure 3.7 Fabrication process of Au NP-cavity designs for the MB reaction. The TiO_2 cavity thickness (h_{TiO2}) is controlled by adjusting the sputtering duration, while Au NPs are synthesized *via* a

self-assembly approach, with their radii (R) and interparticle gaps (g) determined by the thickness of the deposited Au layer.

Table 3.1 TiO_2 cavity thickness manipulated with sputter processing durations

NO.	Processing time of sputtering	Average TiO_2 thickness nm
1	2 h	106 ± 1.3
2	2 h 10 min	117 ± 2.3
3	2 h 20 min	135 ± 1.7
4	2 h 40 min	160 ± 1.4
5	3 h	182 ± 2.3
6	3 h 20 min	197 ± 1.5

Au NPs were subsequently fabricated using a self-assembly approach. First, a thin Au film was deposited onto the top surface of the TiO_2 cavity using a Kurt Lesker NANO 36 thermal evaporator at a deposition rate of 1 Å/s. And then, the samples were then annealed at 500°C for 2 hours to form segregated Au nanoislands. During this process, only the Au film on the top surface underwent morphological transformation. The size and distribution of the Au NPs can be tailored by adjusting the thickness of the Au layer[89,97], which was set to 5 nm in this study. The resulting Au NP parameters were further characterized using SEM. Finally, the samples were immersed overnight in a 5 ppm MB solution, allowing the molecules to attach to the Au NPs *via* weak dispersion forces[76]. The samples were cleaned with deionized (DI) water, removing the residual molecules from solution while retaining the molecules attached to Au NPs. This resulted in a random distribution of molecules oriented parallel to the surface[98], as illustrated in Figure 3.7F.

3.2.2.Analysis of disordered Au nanoparticles

The thermal stability of the Au mirror layer was evaluated using two reference samples: a bare Au mirror film and an Au film deposited with a 200 nm TiO_2 cavity layer[99]. The total absorption of each sample was measured before and after annealing, as shown in Figure 3.8. The annealing conditions were identical to those used in the self-assembly of Au NPs, conducted at 500°C for 2 hours. The absorption difference induced by the annealing process was found to be less than 8% at the same wavelength across the full spectrum, which is considered negligible. During the self-assembly process of the Au NP-cavity (Figure 3.7E), morphological changes are expected to occur only within the top 5 nm of the Au film forming the NPs.

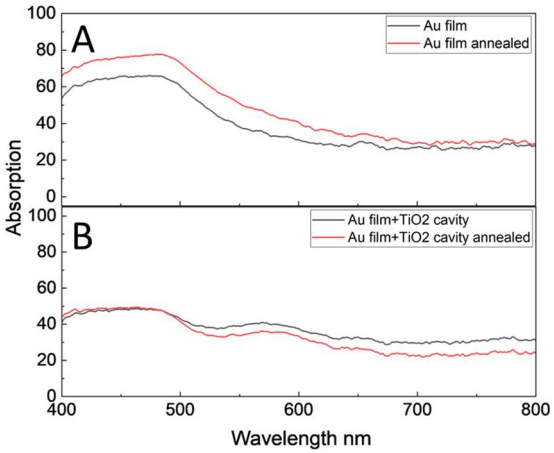

Figure 3.8 Annealing tests of reference samples: A) Absorption of the Au mirror layer on a glass substrate before and after annealing 500°C for 2 hours B) Absorption of the Au mirror layer with 200nm TiO_2 cavity on a glass substrate before and after annealing 500°C for 2 hours.

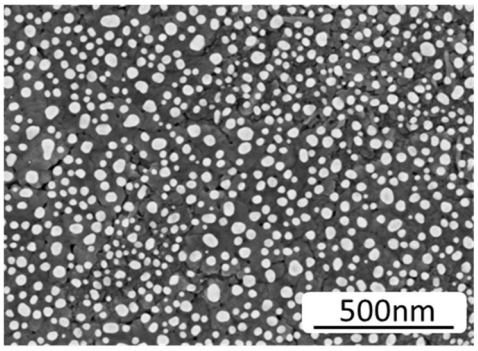

Figure 3.9 Example SEM image of the h_{TiO2} = 182 nm Au NP-cavity for morphology analysis of disordered NPs

Disordered arrays of Au NPs can be effectively represented by optical simulations of approximated periodic arrays of Au NPs to optimize the computational efficiency. However, as shown in Figure 3.5 and Figure 3.6, the plasmonic resonance is sensitive to the NP radius and interparticle gap, might resulting in broader resonances for disordered arrays with some size variation[52]. Figure 3.9 reveals the SEM image of Au NPs on the h_{TiO2} = 182 nm Au NP-cavity sample, which has a disordered distribution and Au NPs show random quasi-circular shapes. To estimate the size parameters of the experimental arrays, the equivalent radius of each NP was determined based on equivalent circles with the same area as the NP observed in the 'top-view' SEM images. Threshold values were set for each sample in the software ImageJ to distinguish NPs from the background and determine their areas. The equivalent radius was then computed from these numerically measured areas. The histograms in Figure 3.10 show the radius distributions for the six samples, revealing a normal Gaussian distribution ranging

from 1 to 30 nm. The mean radius of each sample is slightly fluctuating and was determined as a total average value of 14 nm across all samples, which is the parameter applied in the simulations.

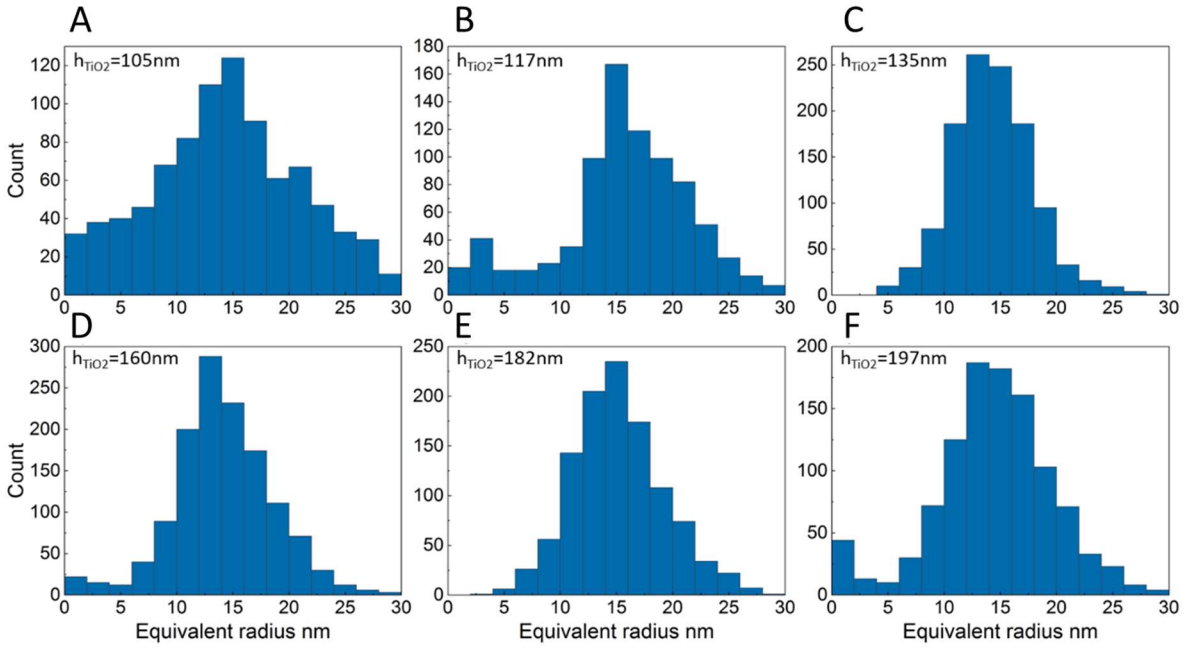

Figure 3.10 Histograms of the equivalent radius for the six fabricated samples. The average radii are 11.0 (h_{TiO2} = 105 nm), 11.7 (h_{TiO2} = 117 nm), 13.3 (h_{TiO2} = 135 nm), 14.1 (h_{TiO2} = 160 nm), 15.2 (h_{TiO2} = 182 nm), 14.4 (h_{TiO2} = 197 nm), respectively.

Similarly, Figure 3.11 presents histograms of the interparticle gaps across the six samples, calculated using the following equation:

$$\mathrm{gap}_{\mathrm{interparticle}} = d_{\mathrm{interparticle}} - r_1 - r_2 \tag{3.3}$$

where $d_{\mathrm{interparticle}}$ is the center-to-center distance between two neighboring NPs, and r_1 and r_2 are the equivalent radii of these particles. The parameters are determined from SEM images with a similar approach to the analysis of the equivalent radius in ImageJ. Figure 3.11 shows histograms of the interparticle gaps for the five closest neighbors in each sample. A normal distribution is observed in the interparticle gaps among samples as well. The interparticle gaps range from 10 to 50 nm, with uniform average values across the samples. The average gap sizes are calculated in each sample ranging from 19.7 to 24.4 nm. This slight difference is affiliated with the disordered distribution and fabrication uncertainties among samples. This parameter is further analyzed to determine the value for the simulation models.

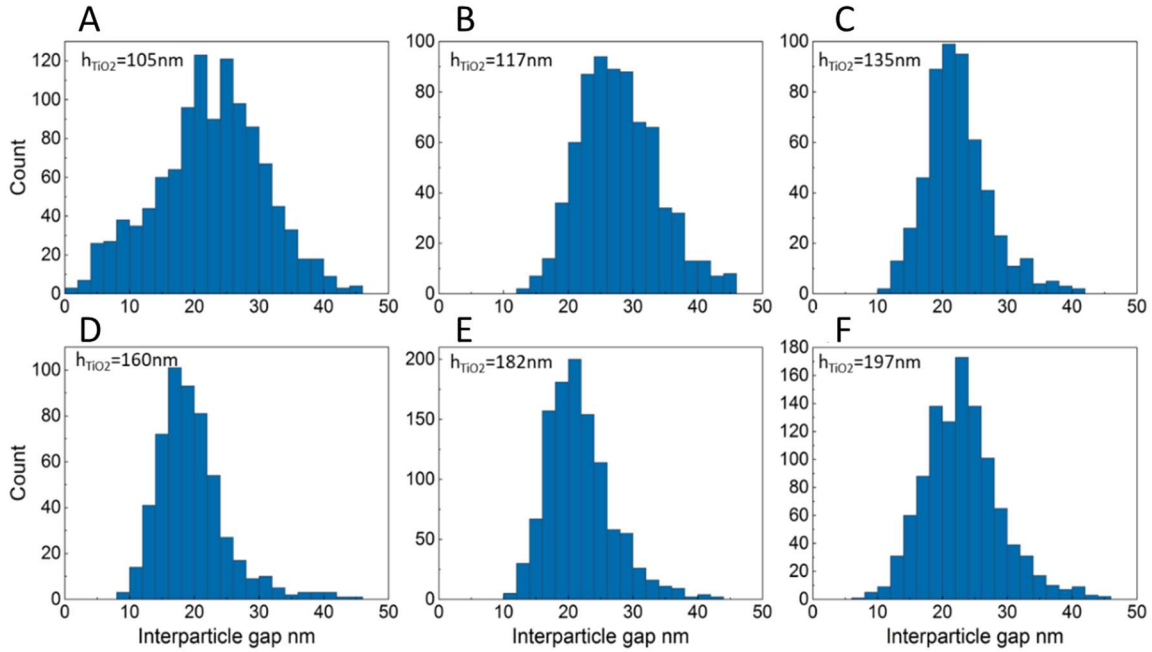

Figure 3.11 Histograms of the average interparticle gap for the six fabricated samples, evaluated based on the five nearest adjacent NPs. The average gaps are 24.4 (h_{TiO2} = 105 nm), 24.4 (h_{TiO2} = 117 nm), 21.9 (h_{TiO2} = 135 nm), 19.7 (h_{TiO2} = 160 nm), 21.7 (h_{TiO2} = 182 nm), 23.4 (h_{TiO2} = 197 nm), respectively.

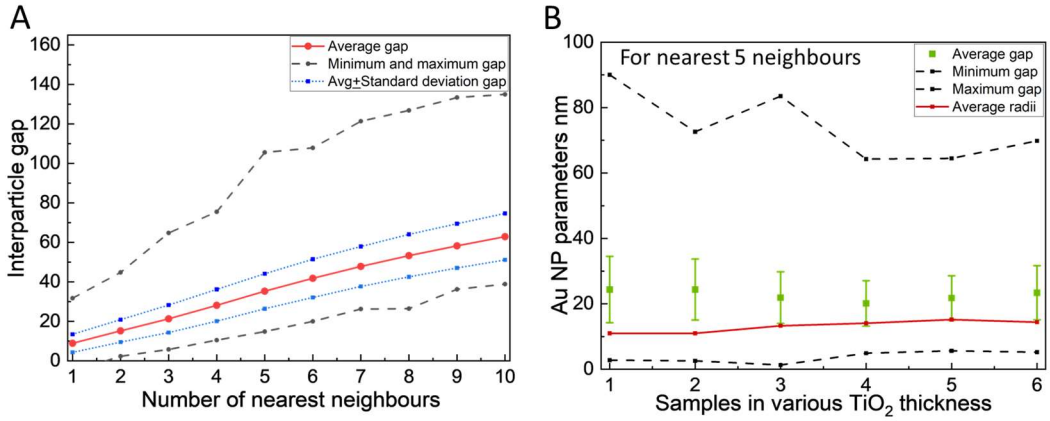

Figure 3.12 A) Interparticle gap of up to ten nearest neighbor particles on the h_{TiO2} = 182 nm sample, showing averaged values as the red solid curve, averaged values ± standard deviation as the blue dotted curves as well as minimum and maximum values as black dashed curves. The inset is an SEM image of this sample. B) Averaged interparticle gaps (green square dot) of five of the nearest neighbor NPs in the six samples. The error bar shows the standard deviation values of NPs. Maximum and minimum gap size (black dash curves) and averaged radii (red solid curve) of all six fabricated samples are given.

The statistical distribution of nanoparticle gaps is further illustrated in Figure 3.12. For the h_{TiO2} = 182 nm Au NP-cavity, the red curve in Figure 3.12A represents the average interparticle gap for up to ten nearest neighboring nanoparticles, which gradually increases from 8 to 50 nm as more neighbors are considered. Since interparticle coupling is significantly affected by the

distance between two particles, the average gap of the five nearest neighbors, 22 nm, is used for subsequent optical analyses. This value is determined by the number of surrounding nanoparticles for each NP. Due to the consistent fabrication conditions, variations in the geometric parameters of the NPs are minimal among all samples as shown in Figure 3.12B with average radius and gap size of a similar magnitude, suggesting that the plasmonic resonances are expected to occur at similar wavelengths[92].

3.3. Optical and catalytic characterization of Au nanoparticle-cavities

3.3.1.Tunable optical properties of Au NP-cavities

The optical properties of the Au NP-cavities were measured using a spectrophotometer, with the experimental setup schematically illustrated in Figure 3.13. A Xenon Arc light source (Thorlabs LPVISE100-A) was employed, providing a broadband spectrum from 240 to 2400 nm. The illumination was focused at the back focal plane of a 10× objective (Olympus Mplan N) using a series of lenses. A field stop and an aperture stop were used to adjust the illumination field and numerical aperture, while a neutral density filter with transmittance ranging from 1% to 100% controlled the light intensity. Mirror 1 was used to switch between reflection and transmission illumination optical paths to excite the Au NP-cavity samples. The reflected or transmitted signals were then collected again by the objective. By flipping in Mirror 4, the sample could also be imaged with Camera 2 for accurate focusing. By flipping out Mirror 4, the optical signal is coupled into an optical fibre connected to the spectrometer to record the spectrum by Camera 1. The effective wavelength range of the setup, determined by the light source, objective, and spectrometer, was 400 - 900 nm. For calibration, the spectrophotometer was referenced against a mirror with >99% reflectance. Each spectrum was acquired with a 50 s integration time and averaged over ten measurements to minimize random noise. The absorption of the samples A=1-T-R was subsequently calculated from the measured transmittance (T) and reflectance (R) spectra.

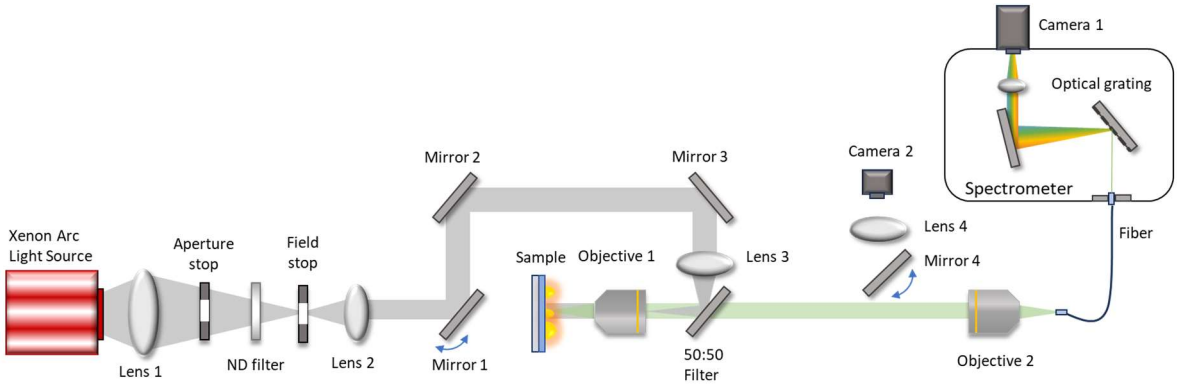

Figure 3.13 Optical layout of the spectrophotometric setup employed for optical property measurements of Au NP-cavity samples

The absorption spectra of the samples were experimentally measured and are presented in Figure 3.14 compared to the corresponding simulation results. In the simulation model, the Au NPs were assigned constant parameters of R = 14 nm and gap = 22 nm, representing the average values obtained from SEM analysis. Overall, the simulated spectra (dashed curves) reproduce the experimental trends (solid curves) with good agreement. For example, the h_{TiO2} = 105 nm Au NP-cavity exhibits suppressed absorption of only 4% at the target wavelength of 633 nm (marked by the red vertical line in Figure 3.14A). This suppression originates from the inhibition of the hybrid Au NP-cavity resonance, as the LSPR is calculated at 659 nm, coincides with the destructive interference node of the F-P cavity. A similar suppression (~4%) is observed in the simulated spectrum at 633 nm. The absorption peak at wavelengths below 450 nm arises from background absorption in both the Au mirror and TiO_2 cavity layer, while a cutoff is observed near 600 nm. As the cavity thickness increases (Figure 3.14B-F), the F-P resonance peak progressively red-shifts, enhancing the spectral and spatial overlap between the LSPR and the F-P resonance. This results in a stronger hybridized mode and, consequently, increased absorption at the target wavelength.

For the samples with cavity thickness h_{TiO2} = 160 nm or more (Figure 3.14D-F), the F-P resonance spectrally overlaps with the LSPR, resulting in strong coupling and the appearance of energy splitting, reversals as dual absorption peaks. For the h_{TiO2} = 160 nm sample (Figure 3.14D), the target wavelength aligns with the higher-energy peak ω_+ of the hybridized mode, whereas for the h_{TiO2} = 197 nm sample (Figure 3.14F), it coincides with the lower-energy peak ω_-. In the case of the h_{TiO2} = 182 nm sample (Figure 3.14E), the target wavelength lies between the F-P and LSPR peaks. As a result, absorption at the target wavelength reaches a maximum of 92%, with a slight reduction observed for the h_{TiO2} = 197 nm sample.

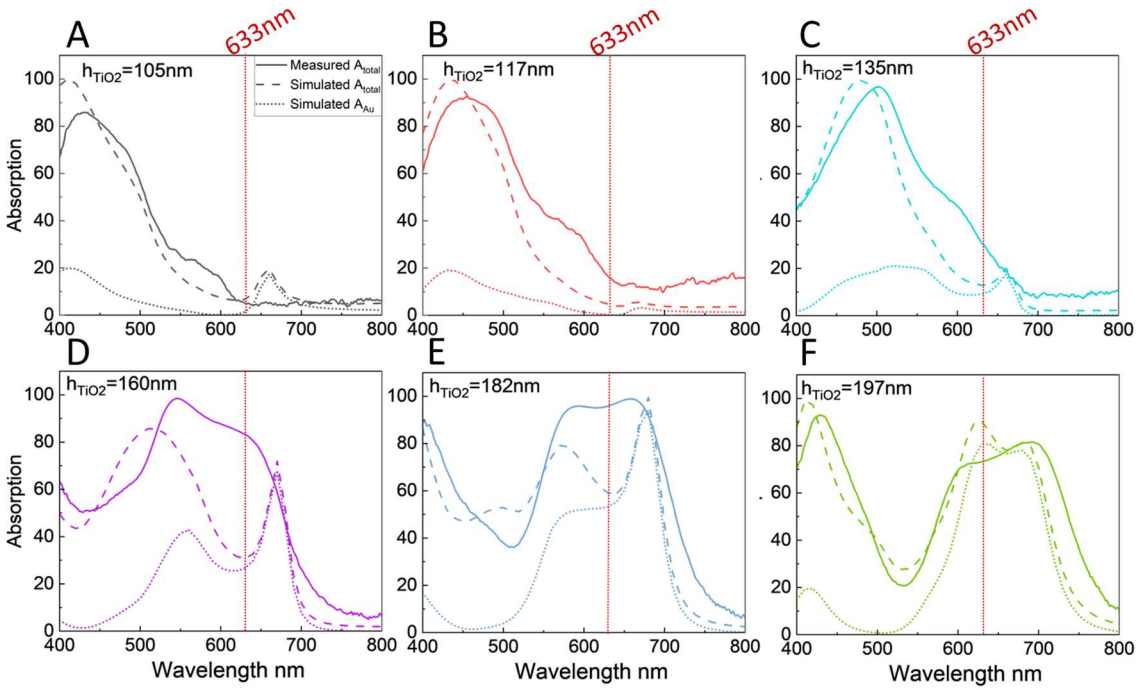

Figure 3.14 Measured (solid curves) and simulated (dashed curves) absorption spectra of six samples: A) h_{TiO2} = 105 nm, B) h_{TiO2} = 117 nm, C) h_{TiO2} = 135 nm, D) h_{TiO2} = 160 nm, E) h_{TiO2} = 182 nm and F) h_{TiO2} = 197 nm. The simulated absorption in solely the Au NPs (dotted curves) directly reveals the plasmonic resonance strengths.

The coupling strength Ω, defined as the absolute difference between the two resonance frequencies ($|\omega_+ - \omega_-|$), characterizes the efficiency of interaction between the plasmonic resonance and the F-P resonance and is given in Table 3.2 for three coupled samples. The maximum coupling strength of 79 GHz is observed for the h_{TiO2}=160 nm sample, where the plasmonic resonance exhibits optimal spatial and spectral overlap with the cavity mode, enabling the most efficient coupling. As the TiO_2 thickness increases, the cavity resonance undergoes redshift, leading to spectral misalignment with the plasmonic resonance. Consequently, the coupling strength decreases to 57 GHz and 51 GHz for h_{TiO2} =182 nm and h_{TiO2} = 197 nm, respectively. Moreover, the coupling strength is more significant in the simulation model compared with measured results, which can be explained as a non-ideal spatial overlap of the LSPR and F-P resonance in fabricated samples.

Table 3.2 Dual peak frequencies and coupling strength of three samples supporting strong coupling

h_{TiO2} nm	Upper resonance frequency ω_+ GHz	Lower resonance frequency ω_- GHz	Coupling strength Ω GHz
160	551	472	79

182	512	455	57
197	486	435	51

Furthermore, the simulated absorption spectra within the Au NPs are shown as dotted curves in Figure 3.14, providing insight into how the hybridized resonances contribute to the photocatalysis of MB molecules adsorbed on the NPs. NP absorption closely follows the trend of total absorption. Notably, absorption within the NPs is suppressed at the target wavelength for h_{TiO2} = 105 nm and h_{TiO2} = 117 nm samples, while it reaches a maximum of 81% for h_{TiO2} = 197 nm sample. For the h_{TiO2} = 160 nm sample, the simulated spectrum exhibits a slight redshift (~10 nm) of the lower-energy peak compared to the experimentally measured total absorption. This discrepancy likely arises from the simulation model, which assumes uniform NP radii and interparticle spacing, only approximating the behavior of randomly distributed Au NPs. Importantly, the fraction of NPs absorption in the total values, available to drive photocatalysis, depends on the spectral position of the dual peaks, with higher fractions generally observed at the lower-energy resonance. As a result, significant enhancements are achieved for the h_{TiO2} = 160 nm at lower-energy resonance, where the Au NPs exhibit absorption values of 74%.

3.3.2.Au NP-cavities in controlling MB reaction yield

The N-demethylation of MB is employed as a model reaction to investigate the mechanisms of plasmon-mediated photoreactions[26,76]. The excitation laser is 633 nm, a wavelength that overlaps both with the LSPR of the disordered Au NPs and the absorption spectrum of MB, and is accessible for our characterization equipment[77]. The reaction process was monitored in real-time using SERS, which was introduced in detail in Section 2.4. Specific Raman peak intensities were tracked to correlate with the molecular concentrations of reactants and products, while the vibrational fingerprints provided direct insight into the temporal evolution of the reaction[82,86].

Raman spectra were initially measured on reference sample as shown in Figure 3.15, demonstrating the role of light-induced catalysis in the model reaction. MB adsorbed on an h_{TiO2} = 170 nm bare TiO_2 film deposited on an Au mirror substrate. Due to the absence of a plasmonic resonance, the Raman signal intensity was significantly reduced, as shown by the black curve in Figure 3.15 (magnified by a factor of 10). A higher laser power (13.6 mW) and

longer integration time (20 s) were required to obtain a detectable spectrum. Only few characteristic Raman peaks were identified, including the C-C stretching of the benzene ring at 1622 cm^{-1} and the C-N-C skeletal vibration of MB at 448 cm^{-1}. Importantly, the product peak at 480 cm^{-1} was significantly suppressed in the sample without Au NPs, compared with that of the Au NP-cavity sample with the same TiO_2 thickness (green curve), measured under 0.68 mW laser at the 20 s (1 s integration per spectrum). Similarly, reactivity increases with rising laser intensity on a h_{TiO2} = 160 nm Au NP-cavity sample, as shown in Figure 2.8B, which illustrates a pronounced growth of the product peak under strong illumination at 0.68 mW. These results highlight the critical role of the plasmonic resonance in the Au NP-cavity, where light trapping and field enhancement at the NP interfaces drive the photocatalytic degradation of adsorbed MB molecules.

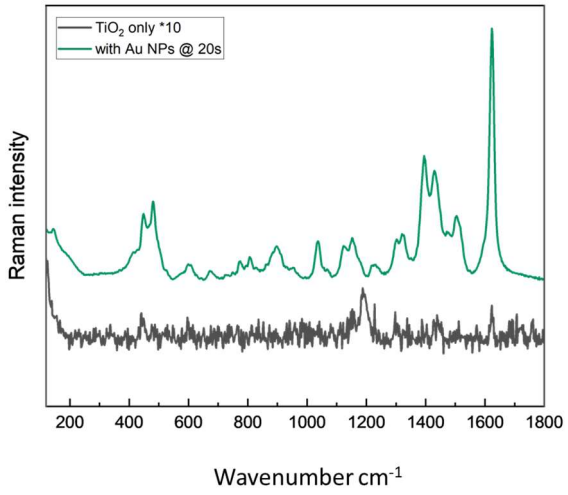

Figure 3.15 Raman spectrum of MB adsorbed on a h_{TiO2} = 170 nm TiO_2 film without Au NPs was measured using a 13.6 mW, 633 nm laser with a 20 s integration time (black curve). The result is compared with the signal from the h_{TiO2} = 160 nm Au NP-cavity sample under 0.68mW 633 nm laser at t = 20th s (green curve).

Raman signals were recorded for the samples over a 10 s period with a 0.1 s interval, which are shown as the blue to red curves in Figure 3.16. At the initial timestep (t = 0.1 s), the dark blue curve in Figure 3.16A displays the vibrational fingerprints of MB, providing detailed information about its chemical bonds. The peak at 448 cm^{-1} corresponds to the C-N-C skeletal deformation in MB[76], which undergoes cleavage during the N-demethylation photocatalytic reaction. By the final timestep (t = 10.0 s), a new vibrational peak appears at 480 cm^{-1}, assigned to the skeletal deformation mode of the product, N-demethylation deviations. Meanwhile, the

peak at 1622 cm^{-1}, associated with C-C stretching in the benzene ring[76], remains unchanged throughout the reaction, enabling normalization of the spectra across different timesteps.

To investigate the influence of tunable optical properties on photocatalytic performance, SERS measurements were performed on the six samples under identical illumination conditions (same wavelength, power and polarization), with tracking of specific Raman peaks associated with the reaction. Figure 3.16B presents the temporal Raman spectra for Au NP-cavity samples with TiO_2 thicknesses of h_{TiO2} = 105 nm, h_{TiO2} = 160 nm, and h_{TiO2} = 197 nm

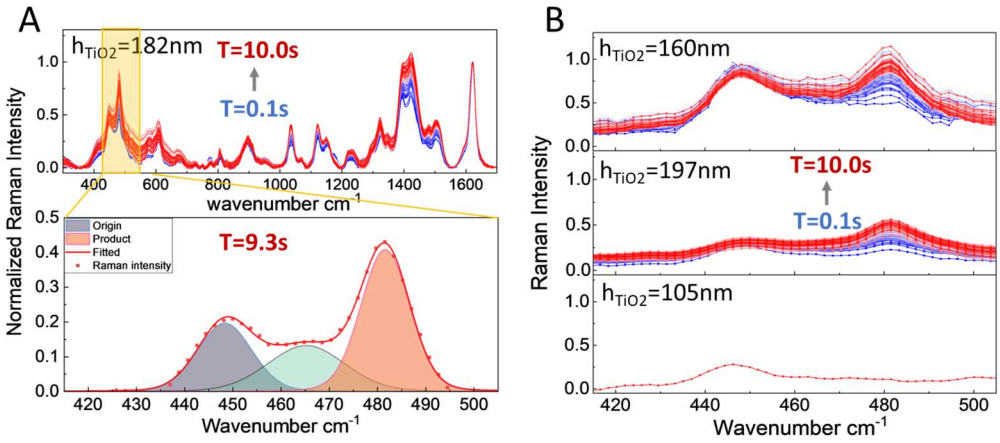

Figure 3.16 A) (top) Normalized SERS intensity from time-resolved measurements over a 10 s period (color gradient from blue to red) for the h_{TiO2} = 182 nm sample. (bottom) Fitted curves of the reactant (grey curve) and product (orange curve) peak in the Raman spectrum at timestep t = 9.3 s compared with measured data (red dots) including an auxiliary third peak for fitting (green curve). B) Raman spectrum of h_{TiO2} = 105 nm, h_{TiO2} = 197 nm and h_{TiO2} = 160 nm samples in the wavenumber range 410 - 520 cm^{-1}.

For the h_{TiO2} = 105 nm sample, negligible changes are observed in the Raman spectra during the 10 s measurement, indicating that the reaction is strongly suppressed. This suppression arises from the low absorption in the Au NPs caused by the overlap of the LSPR resonance with the destructive interference node of the F-P cavity. In contrast, the h_{TiO2} = 160 nm sample exhibits a measured absorption of 86% at the excitation wavelength of 633 nm (Figure 3.14D). Here, the normalized product peak intensity increases significantly from 0.49 to 1.14, demonstrating strong enhancement of the reaction enabled by the tuned optical properties of the Au NP-cavity. Similarly, for the h_{TiO2} = 197 nm sample, which exhibits 69% absorption at 633 nm, the product peak intensity increases from 0.22 to 0.55, indicating a moderate enhancement.

To quantitatively analyze the temporal evolution of the SERS signal intensity[26], the product yield was estimated for samples with varying cavity thicknesses with the approach introduced in Section 2.4.2. Baseline correction is first applied to each SERS spectrum, and peaks in the 415 - 505 cm^{-1} range are deconvoluted to fit with Gaussian-Lorentzian blend model. The lower plot of Figure 3.16A shows the fitted curves for the h_{TiO2} = 182 nm sample at t = 9.3 s as an example. The product yield is then quantified by integrating the area under the fitted curve with peak at ~480 cm^{-1}, highlighted as the shaded orange region in Figure 3.16A.

The estimated product yields as a function of time are presented in Figure 3.17A, illustrating the temporal evolution across the six samples. For the h_{TiO2} = 105 nm and h_{TiO2} = 117 nm samples, the yields remain negligible throughout the measurement period, as the suppressed plasmonic resonance is insufficient to provide the energy required to drive the reaction. In contrast, the other four samples show rapidly increasing yields within the first 5 s, followed by stabilization over time, with the magnitude of the final timestep yield varying according to the tailored hybridized resonance modes of each sample.

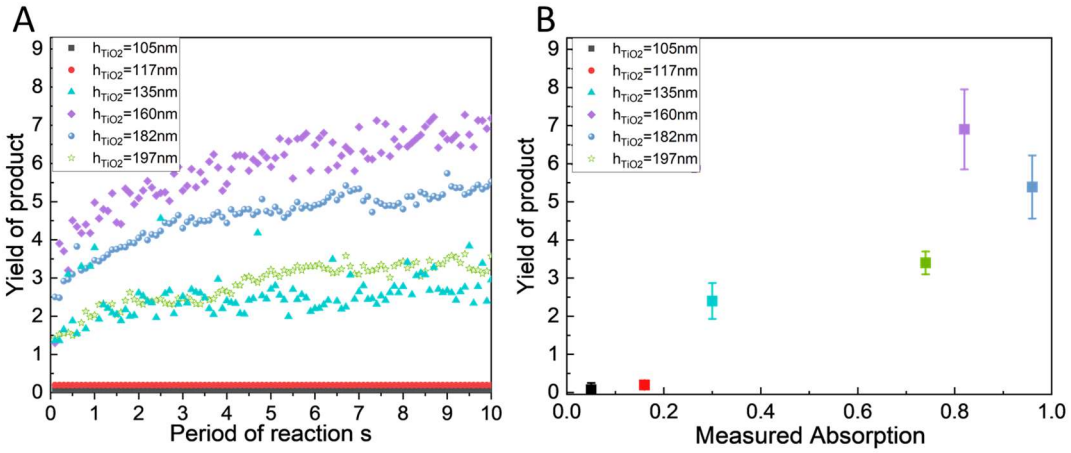

Figure 3.17 A) Time-dependent evolution of product yields for the six samples. B) Correlation between the average yield at the final timestep (t = 10 s) and the measured absorption. Error bars represent the standard deviation calculated from five independent measurements for each sample.

To elucidate the relationship between the optical and catalytic properties of the Au NP-cavities, Figure 3.17B presents the average product yield at the final timestep (t = 10 s) as a function of the measured absorption at the target excitation wavelength of 633 nm. Error bars represent the standard deviation from five independent SERS measurements collected at different positions on each sample. A clear positive correlation is observed between product yield and optical absorption. For the h_{TiO2} = 105 nm and h_{TiO2} = 117 nm samples, where absorption remains

below 10%, the reaction is strongly suppressed, yielding only 0.07 and 0.20, respectively. In contrast, samples with absorption exceeding 80% exhibit notably enhanced photocatalytic activity, with yields of 7.18 and 5.52 for the h_{TiO2} = 160 nm and h_{TiO2} = 182 nm samples, respectively. Overall, the relative reaction yield increases by more than two orders of magnitude when transitioning from samples with low optical absorption (<10%) to those with high optical absorption (~80%), highlighting the pivotal role of tailored optical resonances in driving plasmon-mediated photocatalysis.

It is important to note, however, that the relationship between absorption and product yield is not strictly monotonic. For example, the maximum yield is observed for the h_{TiO2} = 160 nm sample, despite its measured absorption being slightly lower than the h_{TiO2} = 182 nm sample. This discrepancy arises because the correlation is based on the measured *total* absorption rather than the absorption specifically occurring within the Au NPs, which more directly reflects the hot-electron transfer rate and near-field enhancement[26,38]. Unfortunately, direct experimental quantification of NP-specific absorption remains challenging with standard optical characterization techniques. Moreover, NP absorption is not expected to scale linearly with the total absorption at the excitation wavelength, as evidenced in the simulated spectra (Figure 3.14). In general, simulations reveal that the fraction of the total absorption occurring within the Au NPs is higher at the low-energy peak than at either the high-energy peak or the spectral dip between them. Consequently, a larger fraction of the measured total absorption at 633 nm is likely localized in the Au NPs for the h_{TiO2} = 160 nm sample, where the low-energy peak coincides with the excitation wavelength, compared to the h_{TiO2} = 182 nm sample, where the dip between the hybridized peaks aligns with the target wavelength. This explains the higher product yield in the former case. A consistent trend is also observed in simulations of non-thermal effects, including averaged near-field enhancement[74] and hot-electron generation rate[52,70]. As shown in Figure 2.3A and B, the low-energy peak exhibits both stronger near-field enhancement and a substantially higher hot-electron generation rate compared to the high-energy peak and the dip. Thus, the alignment of the low-energy peak with the excitation wavelength in the h_{TiO2} = 160 nm sample is expected to yield superior photocatalytic performance due to simultaneous enhancement of both non-thermal mechanisms.

These results demonstrate that reaction yields can be precisely controlled through the deliberate tuning of optical resonances. Importantly, all experimental conditions, catalyst composition, reactant species, and excitation light parameters, are held constant during the measurements of

all six samples. By modulating the optical properties *via* hybridization between the F-P cavity resonance and the LSPR of the Au NPs, we actively suppress or enhance the photocatalytic yield. In the specific photoreaction studied, the N-demethylation of MB, the degradation process can be selectively disabled, activated, or significantly enhanced by tuning the TiO_2 cavity resonance relative to the molecular resonance (*i.e.*, the HOMO-LUMO gap) of MB.

Moreover, this tunability is achieved without resorting to complex nanofabrication techniques. Shifting the resonance of the hybridized mode is accomplished simply by adjusting the TiO_2 film thickness *via* deposition time. This facile method offers fine control over the optical response while maintaining fabrication simplicity. In addition, the application of a self-assembly approach to form the Au NP arrays circumvents the size constraints inherent to top-down lithographic techniques, enabling scalable fabrication over large areas—an essential requirement for transitioning toward practical, device-level applications.

Hybridized modes can offer additional spectral tunability beyond what is demonstrated here**.** Previous studies have shown that these modes can be exploited to tailor quality factors Q and optimize absorption spectra for a range of applications[52]. By demonstrating the prescriptive suppression and enhancement of photoreactions in this study, this results suggest that this enhanced spectral flexibility could be applied to more complex catalytic systems, such as multi-pathway CO_2 reduction reactions (CO2RR)[5].

In summary, we designed a series of self-assembled Au NP cavities to precisely control plasmonic resonance strength *via* the coupled F-P resonances by tuning the TiO_2 cavity thickness. The strong coupling between plasmonic and F-P modes can be strategically employed to either enhance or suppress a model reaction, the photodegradation of MB, through two non-thermal effects of LSPR: near-field enhancement and hot electron transfer. By tuning the F-P node or peak to achieve optimal spatial and spectral overlap with the plasmonic resonance, the reaction can be efficiently facilitated and enhanced. Specifically, this approach increases the product yield from 0.07 to over 7.18 in our samples, as quantified by the integration of the product vibrational peak at 480 cm^{-1} in the Raman spectrum. Although disordered Au NPs pose a challenge in predicting their optical properties, the sample demonstrates scalability to the device level. These findings demonstrate that plasmonic hybridized nanostructures enable optically precise control over chemical reactions to selectively enhance or suppress product yields.

Chapter 4. Morphology of metasurfaces for light-driven reactions

Photocatalytic reaction manipulation has been demonstrated using a series of Au NP-cavity samples, in which the plasmonic resonance of Au NPs is tuned *via* mode hybridization with cavity modes[73]. However, the optical tunability is constrained by the inherent uncertainties and limited resolution of current nanofabrication techniques, reducing the flexibility in controlling reaction reactivites[33,100]. Structural variations among samples introduce additional uncertainty in estimating optical properties, further complicating metasurface design. To address these limitations, a strategy employing a single metasurface configuration is proposed to enable high-precision and dynamically controllable photocatalytic reactivity[101]. In this chapter, we present an approach in which the light-driven reaction is actively tuned *via* morphology engineering, leveraging a polarization-dependent metasurface to tailor the optical properties.

4.1. Design of polarization-dependent metasurfaces

4.1.1. Elliptical Au-TiO_2 nanopillar arrays

Polarization-dependent metasurfaces can support resonances across a range of wavelengths, enabling the tuning of optical properties through polarization state switching[44,102,103]. Asymmetric nanopillars exhibit polarization-dependent resonances[45], which when arranged in a regular array can be employed in effectively modulating light-driven reactions[41]. In this study, an array of elliptical Au and TiO_2 nanopillars (Au-TiO_2 NPil), illustrated in Figure 4.1, was designed with independently defined major and minor axes (R_x and R_y), allowing precise control of resonance wavelengths under switching between two orthogonal polarization states of the incident light. This polarization-sensitive optical response at specific wavelengths is crucial to achieve tunability in photocatalytic processes, enabling deliberate shifts in product

yield[36] and demonstrating the capability to enhance desired reactions or pathways while simultaneously suppressing undesired byproduct formation.

In the design of elliptical Au-TiO_2 NPil metasurfaces, the nanopillar array is fabricated on an Au mirror layer with a thickness of 200 nm, which acts as a reflecting background. Each TiO_2 nanopillar is capped with an Au nanodisk (ND) that concentrates incident light, supporting strong localized plasmonic resonances and light trapping at each individual nanopillar. Both the NPil and ND feature elliptical base geometries, with independently tailored radii along each axis to tune the LSPR wavelength individually. The optical properties, such as near-field enhancement (green dash square in Figure 4.1) and hot-electron generation rate (red dash square in Figure 4.1), are optimized under a specific polarization and deliberately detuned under the orthogonal polarization[44]. The TiO_2 NPils and Au NDs have heights of 100 nm and 15 nm, respectively, providing robust plasmonic resonances under the optimized polarization and enhancing the overall tunability. More detailed criteria for the morphological parameter selection will be discussed in Section 4.1.2.

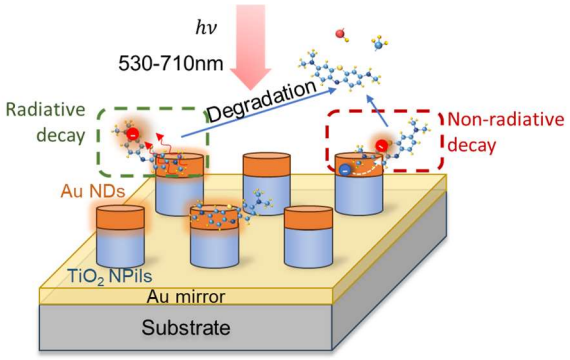

Figure 4.1 Schematic of a Au-TiO_2 elliptical nanopillar array for MB degradation *via* two nonthermal effects: (green) near-field enhancement from radiative decay and (red) hot-electron injection from non-radiative decay.

As introduced in Section 2.3, the catalytic performance is evaluated using a model reaction: the N-demethylation of MB (see Figure 2.6). The photocatalytic activity of light-driven reactions is strongly wavelength-dependent, primarily determined by the HOMO-LUMO energy gap of the reactant molecules, which in turn guides the metasurface design. For MB, and considering the available SERS laser sources, the target excitation wavelength is set to 633 nm, corresponding to the effective range of its catalytic activity.

In the metasurface design, the plasmonic resonance is engineered to match the molecular electronic transitions under TM light excitation[66]. This resonance alignment enables both photons and hot electrons to efficiently populate the LUMO of MB, thereby enhancing the reaction rate[39]. In contrast, under TE polarization, the elliptical nanostructures induce a detuning of the resonance peak from the HOMO-LUMO gap. As a result, the localized electric field strength at 633 nm is significantly reduced, leading to diminished non-thermal effects and suppressed catalytic activity. Thus, the Au-TiO_2 elliptical nanopillar array supports polarization-sensitive photocatalytic reactivity, enabling active modulation of product yield.

4.1.2.Simulation of Au-TiO_2 nanopillar arrays and parameter design

The elliptical Au-TiO_2 NPil metasurface was designed and analyzed through optical simulations using *COMSOL Multiphysics* under two orthogonal polarization states TM and TE. When the light is incident vertically on the sample, the TM polarization state corresponds to the electric field polarized along the x-direction, whereas the TE polarization state corresponds to the electric field polarized along the y-direction. The underlying simulation principles and technical procedures are detailed in Section 2.1. In this work, both the electric near-field distribution and far-field optical properties were modeled using the FEM. Due to the asymmetry of the elliptical nanopillar geometry, the radii along the two elliptical axes differs and were systematically varied to investigate their effects under different polarization states. The refractive index of TiO_2, which influences the resonance wavelength of Mie scattering in the nanpoillars[103], was obtained from ellipsometry measurements as shown in Figure 3.2. Floquet periodic boundary conditions were applied to all four lateral surfaces to replicate an infinite periodic array of NPils. The incident light was normally coupled to the nanostructure *via* a wave excitation port, with polarization defined at the source. The polarization-dependent optical response of the metasurface was then examined as a function of the NPil radius along the x- and y-directions.

To investigate the effect of structural asymmetry, the nanopillar radius along the y-direction (R_y) was varied from 30 to 70 nm, while the x-direction radius (R_x) was fixed at 30 nm, as shown in Figure 4.2A. Under TM polarized excitation, the metasurface supports a stable plasmonic resonance in the range of 630 - 650 nm, exhibiting peak total absorption primarily governed by the Au ND radius along the x-direction[45,104]. As the parameter is varying in the perpendicular direction, the absorption peak is slightly blue-shifted by up to 20 nm in the

investigated range, providing a continuous plasmonic resonance[68]. In contrast, when the excitation is switched to TE polarization, the peak absorption wavelength exhibits a pronounced redshift from 620 to 950 nm with increasing R_y. For the model reaction, the morphological design is optimized for a target wavelength of 633 nm. For example, in the configuration with R_y = 60 nm, the absorption at the target wavelength increases dramatically from 27.9% (TE) to 99.9% (TM), as illustrated in Figure 4.2A. This pronounced polarization-dependent absorption behavior provides a versatile mechanism for tunable metasurface design.

To further evaluate the plasmonic resonance strength, the near-field distribution is shown as a cross-sectional map of the electric field enhancement (E^2/E_0^2) for the Au-TiO_2 NPil unit cell in Figure 4.2B. The arrows in the figure represent the time-averaged Poynting vector $\boldsymbol{S}$, normalized to the incident Poynting vector $\boldsymbol{S}_0$, indicating the magnitude and direction of energy flow. For the Au-TiO_2 NPil with R_x = 30 nm and R_y = 60 nm, Figure 4.2B(i) and B(ii) depict the near-field distribution at the target wavelength of 630 nm under TM and TE polarization, respectively, highlighting the optical tunability of metasurface. In addition, under TE polarization, the peak field enhancement occurs at 820 nm, as shown in Figure 4.2B(iii), revealing a potential for catalytic activity at longer wavelengths[105].These results also demonstrate the contribution of TiO_2 NPil in providing a polarization-dependent optical response.

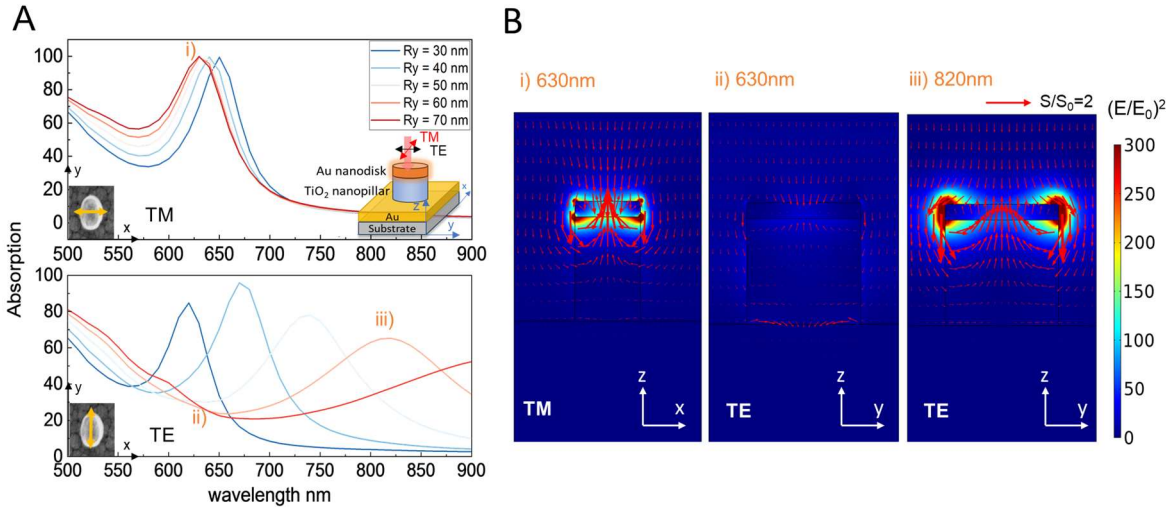

Figure 4.2 Simulations of Au-TiO_2 NPil arrays with increasing radius along the y-direction. A) Total absorption spectra for R_y ranging from 30 to 70 nm, with R_x fixed at 30 nm. Incident light is linearly polarized in TM (top) and TE (bottom) modes; polarization directions are defined in the insets from SEM images. (B) Electric field enhancement (color scale) and normalized Poynting vectors (red arrows) for a unit cell of the array with R_x = 30 nm and R_y = 60 nm: (i) under TM polarization at 630

nm in the xz-plane; (ii) under TE polarization at 630 nm in the yz-plane; and (iii) under TE polarization at 850 nm in the yz-plane.

Localized electric fields are strongly enhanced at 630 nm under TM-polarized irradiation, with the intensity concentrated near the Au ND due to strong plasmonic effects, as shown in Figure 4.2B(i). The maximum electric field enhancement ($E^2_{\mathrm{TM\ 630nm}}/E_0^2$) reaches 1517 at the Au ND surface. This substantial enhancement is corroborated by the corresponding Poynting vector distribution, which reveals strong, circulating energy flows surrounding the Au ND, efficiently concentrating light around the metal structure indicating a significant plasmonic resonance[45]. In contrast, under TE polarization, the target wavelength drops into a spectral absorption dip. The electric field enhancement ($E^2_{\mathrm{TE\ 630nm}}/E_0^2$) reduced to 33, nearly 1/50th of the value observed under TM polarization at the same wavelength. The associated Poynting vector distribution exhibits markedly weaker energy flow, and partial propagates into the mirror layer and substrate, inducing diminished resonance within the ND.

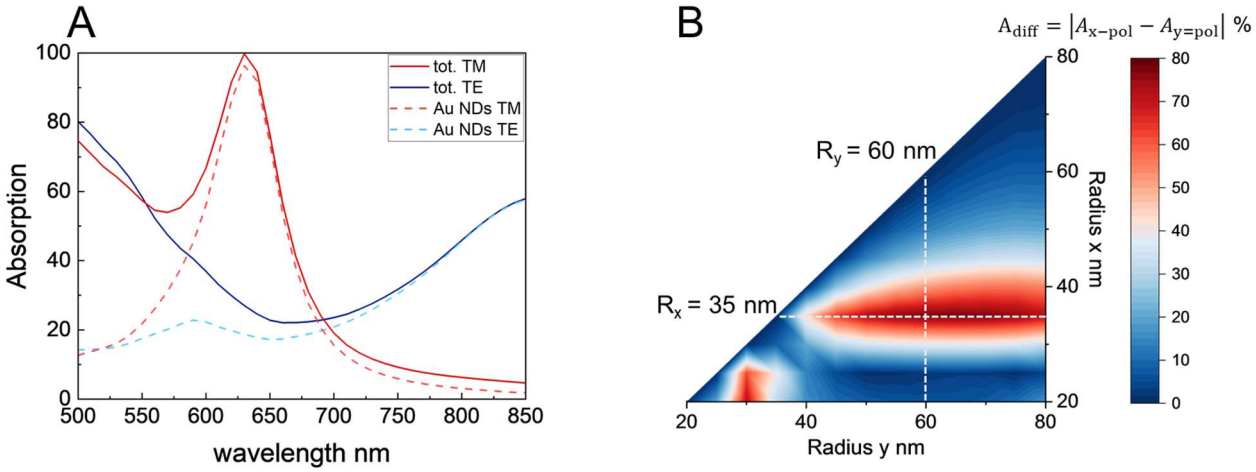

Figure 4.3 A) Absorption in Au NDs and the total absorption of the Au-TiO_2 NPil array (R_x = 35 nm, R_y = 60 nm) under TM and TE polarizations. B) Absorption difference (A_{diff}) as a function of nanopillar radii in the x- and y-directions, representing the variation in absorption between TM and TE illumination. The maximum A_{diff} values are selected as the design parameters for fabricated samples.

This phenomenon can be explained by examining the contribution of the Au ND, as shown in Figure 4.3A. Under specific illumination conditions at peak wavelength, the plasmonic ND accounts for nearly 96% of the peak total absorption. However, at the total absorption dip, such as for the TE mode at 630 nm, the Au ND contributes only 18%. These results confirm that the metasurface is purposefully engineered to tune the peak plasmonic resonance *via* polarization state control, tailoring the wavelength-dependent field enhancement. Additionally, the lattice

resonance among the Au NDs also contributes to the enhanced absorption and plasmonic resonance. As illustrated in Appendix 5, increasing the gap distance reduces the LSPR and total absorption, revealing the role of inter-coupling between neighboring Au NDs. The significant difference in optical response between the two orthogonal polarization states will offer a remarkable tunability. The population of electrons in unoccupied molecule orbitals are tailored through the tuning in near-field enhancement and hot electron generation rate, which reveals in Appendix 5. It is particularly advantageous for applications such as photocatalytic reactions, where strong and selective light-matter interactions at target wavelengths are essential.
Additionally, high absorption under TE polarized light occur at the peak wavelength of 820 nm, results in a pronounced electric field enhancement as well with $E^2_{\mathrm{TE\ 820nm}}/E^2_0$ reaching 1768, as shown in Figure 4.2B(iii). The near-field enhancement is concentrated near the Au NDs, consistent with the energy concentration indicated by the Poynting vector distribution. At this peak, the total absorption spectrum closely overlaps with the Au ND absorption spectrum as shown in Figure 4.3A, highlighting the dominant contribution of the plasmonic resonance. This peak absorption demonstrates the potential for driving resonance-enhanced catalytic reactions at longer wavelengths, which can be applied to control multiple reactions[8].

To optimize the tunability of the Au-TiO_2 NPils, the metasurface is designed to maximize the difference in absorption between the two orthogonal polarization states. This parameter is quantified as the absolute difference (A_{diff}) in the values under TM and TE modes at the target wavelength of 633 nm, as shown in Figure 4.3B, and guides the morphology engineering of metasurface. The maximum absorption difference occurs at R_x = 35 nm and R_y = 60 nm, exceeding 60%, indicating that these elliptical dimensions provide the greatest tunability in polarization-sensitive response.

4.2. Nanofabrication of elliptical Au-TiO_2 nanopillar arrays

The Au-TiO_2 NPil array was fabricated using a top-down lithographic approach, as outlined in Figure 4.4. Sample preparation began with the deposition of a Au mirror layer with thickness of 200 nm onto a 1 mm glass slide substrate under a vacuum pressure of 1×10^{-5} Torr (Figure 4.4A and B). Subsequently, an anatase TiO_2 layer was sputtered onto the Au mirror under a chamber pressure below 4×10^{-6} Torr (Figure 4.4C), with a deposition rate of approximately 0.17 Å/s. The height of the TiO_2 nanopillars was determined by the layer thickness, set to 100 nm, which was precisely controlled by the sputtering duration.

In Figure 4.4D, the pattern was defined using a Raith 150 electron-beam lithography (EBL) system with a bilayer PMMA photoresist consisting of PMMA 495 A2 and PMMA 950 A4. The bilayer PMMA photoresist can improve the quality of the lift-off process to clearly pattern the samples. The quality of the lithography can be controlled by the electron beam dose, with a base dose of 50 $\mu C/cm^2$ and a dose factor ranging from 2.5 to 3.2. The axes lengths of the elliptical pillars were also adjustable in a small range through variations in the EBL dose. Subsequently, 14 nm of gold and 30 nm of nickel (Ni) were sequentially deposited *via* E-beam evaporation, followed by lift-off in acetone for over 4 hours, as shown in Figure 4.4E. The Ni and Au NDs applied as masks for plasma etching. The TiO_2 film was etched using Ar and CHF_3 plasma with inductively coupled plasma (ICP) devices at room temperature for 6.5 minutes to form the NPil array. The process pressure of etching plasma is 0.1 Pa. Finally, as illustrated in Figure 4.4F, the Ni masks were removed by immersion in an $FeCl_3$ solution for 1 minute. The Au-TiO_2 NPil array was formed with each TiO_2 nanopillar capped by an Au NDs. To characterize its catalytic performance, the Au-TiO_2 NPil array was immersed in an MB solution overnight to allow adsorption of the molecules onto the Au NDs surface *via* van der Waals interactions[88].

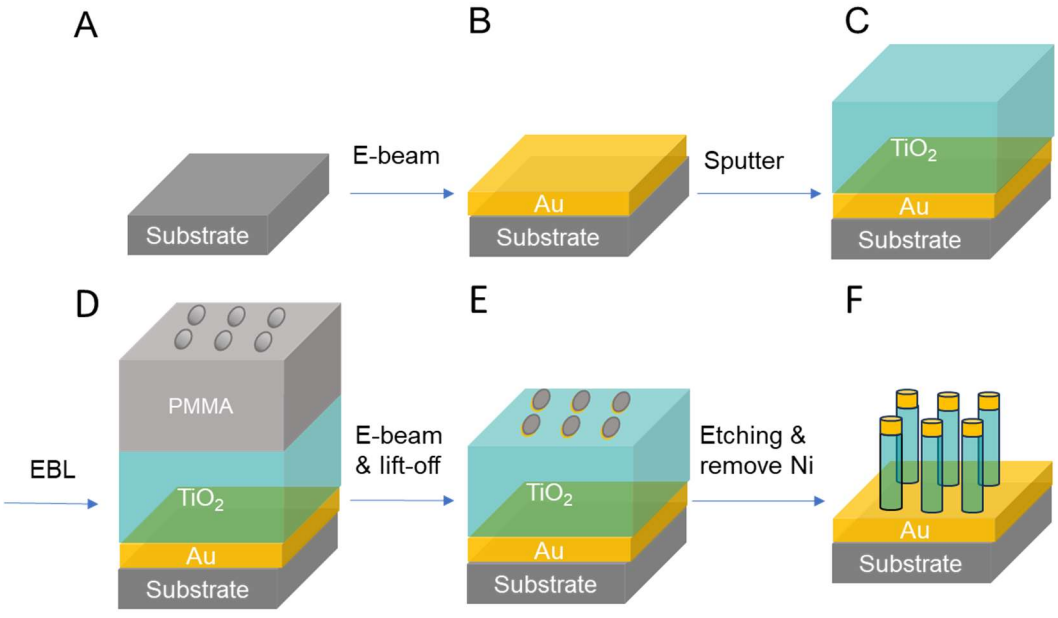

Figure 4.4 Fabrication process of the Au-TiO_2 NPil array with top-down lithography forming the nanopillar array

As demonstrated in Figure 4.2, the morphology of the Au-TiO_2 NPils significantly influences their optical properties, particularly the lengths of the major and minor axes (R_x and R_y). Precise

morphological engineering enables optimal alignment of the plasmonic resonance with the target wavelength, maximizing the tunability of the metasurface. The morphological parameters of the fabricated samples were characterized using SEM micrographs, which reveal the geometric tailoring achieved under increasing EBL doses, as shown in Figure 4.5. All nanopillar arrays exhibit an elliptical shape in the top-view images (Figure 4.5A-D). With increasing dose factors, the radius expands in both the x- and y-directions while the array periodicity remains constant at 200 nm. Since the radius directly affects the plasmonic resonance wavelength, the average values for four dose factor groups were evaluated from the top-view SEM images and are summarized in Table 4.1.

Table 4.1 Measured averaged radius of Au-TiO_2 NPils with increasing EBL dose (reference dose is 50 $\mu C/cm^2$)

Dose factor	2.5	2.6	2.7	2.8	3.1	3.2
R_x nm	27	31	34	36	40	42
R_y nm	49	50	52	55	56	58

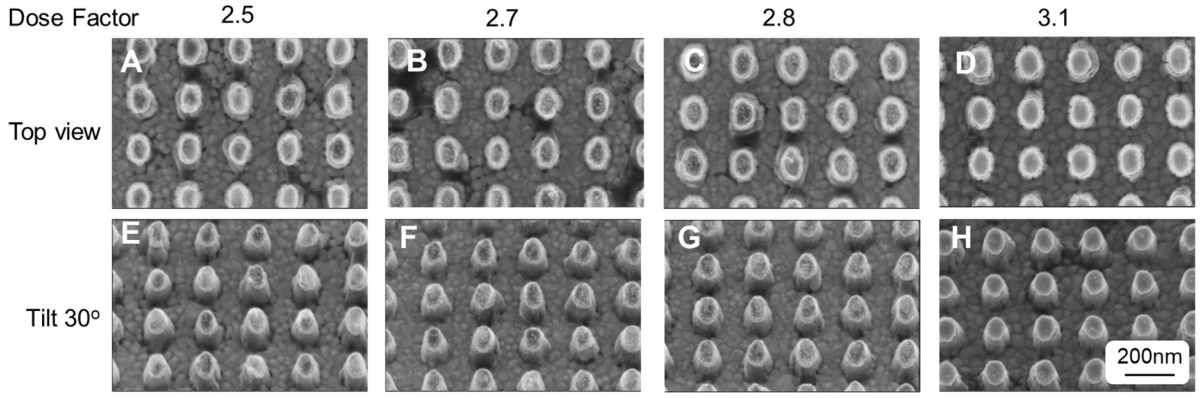

Figure 4.5 SEM image of the Au-TiO_2 NPil arrays prepared with increasing exposure dose factors of EBL from 2.5 to 3.1. The nanopillar radius is enlarged in both x- and y-direction with higher dose. The reference dose is 50 $\mu C/cm^2$.

The minor axis in the x-direction (R_x) primarily determines the resonance wavelength under TM polarization, contributing to absorption enhancement[106]. With the EBL dose increases, R_x grows from 27 to 42 nm. The designed parameters align with the dose factor in the range of 2.7 - 2.8, where R_x approaches 35 nm. A similar trend is observed in the y-direction (R_y), where the radius increases from 49 to 58 nm. Although the designed R_y = 60 nm is slightly beyond this range, the dose factors consider to be determined based on the parameter R_x, since no specific resonance mode is supported under TE polarization. And the design pattern of EBL is

adjusted in R_y to improve the alignment. Moreover, EBL parameters are not the only factors influencing the radius of the Au-TiO_2 NPils. During plasma etching, several parameters, including process pressure[107], plasma bias, and gas flow rate[108], also affect etching quality and thus the final nanopillar geometry.

The sample with the target design geometry was fabricated using an EBL dose factor of 2.7. The morphology of the nanopillar array was analyzed using SEM images, as shown in Figure 4.6. The asymmetric elliptical shape of the nanopillars is evident in the top-view images, with measured radii of $R_x = 35 \pm 3$ nm and $R_y = 60 \pm 4$ nm, determined from the average values of twenty measurements. Based on the simulation results, the metasurface is expected to support a plasmonic resonance under TM polarized light, corresponding to the x-direction radius, while polarization switching enables tunable absorption by shifting the peak wavelength under TE polarization.

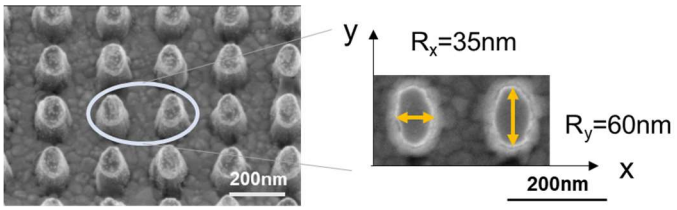

Figure 4.6 SEM images of fabricated Au-TiO_2 NPil with optimized design parameters, shown at a 30° tilt. A top view zooming in two nanopillars measured radius in R_x = 35 nm, R_y = 60 nm.

Additionally, in SEM images tilted by 30°, the TiO_2 NPils exhibit a noticeable defect, namely tapering in both the x- and y-direction radii (both in Figure 4.5E-H and Figure 4.6). The radius at the base of the NPils is larger than at the top, indicating that top-view measurements alone do not fully capture the pillar geometry[29,32]. In Figure 4.6, radius R_x increases from 35 nm at the top to 50 nm at the base, while R_y rises from 60 to 74 nm. Although the designed radii differ in the two directions, the magnitude of tapering is similar for both axes. Since the optical properties are highly sensitive to NPil morphology, particularly the radius, total absorption spectra were simulated to analyze the impact of this tapering[109], as a function of the base radius in Figure 4.7. In this modified model, the radius expands symmetrically in both directions, such that $R_{xtop} - R_{xbottom} = R_{ytop} - R_{ybottom}$. The total absorption peak exhibits a slight redshift (<5 nm) as $R_{xbottom}$ increases to 57 nm and $R_{ybottom}$ to 87 nm. This minimal shift occurs because the total absorption is primarily governed by the plasmonic resonance of the Au NDs which has a constant radius. However, an increase in the full width at half maximum (FWHM)

of the plasmonic resonance peak is observed with increasing base radius, reveals a broadening of the resonance[109].

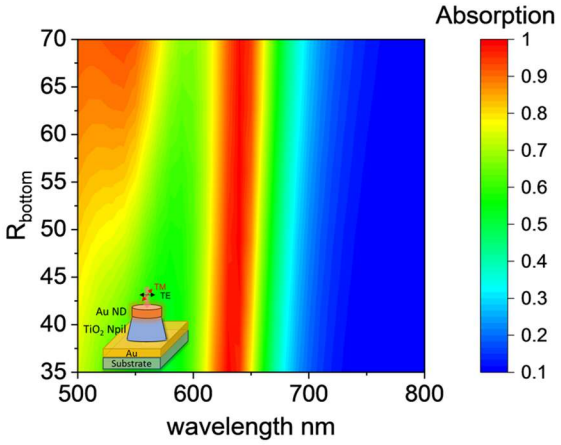

Figure 4.7 Total absorption of the Au-TiO_2 NPil array with a tapered TiO_2 nanopillar (inset) as a function of the bottom radius. The plasmonic resonance wavelength exhibits a negligible redshift of 5 nm, accompanied by a bandwidth broadening from 49 nm to 56 nm.

4.3. Optical and catalytic characterization of Au-TiO_2 nanopillar arrays

4.3.1.Polarization-dependent optical properties

Polarization-dependent absorption spectra were measured using a micro-spectrophotometer equipped with polarization-sensitive components. As illustrated in Figure 4.8, a rotatable linear polarizer (Thorlabs LPVISE100-A) was used to control the polarization of the incident light, which was varied systematically from 0° to 90° to probe the polarization-sensitivity of the metasurface. The measurement area was defined by a square aperture matched to the metasurface array dimension of 100×100 μm. Reflectance (R) and transmittance (T) were independently recorded by flipping Mirror 1, and the absorption was calculated as A = 1 - R - T. To ensure high accuracy and reduce random noise, the spectrometer camera was set to an exposure time of 100 s, and each measurement was averaged over five repetitions. This setup directly links the polarization state of the incident light to the measured absorption, enabling quantitative characterization of the polarization-dependent optical response.

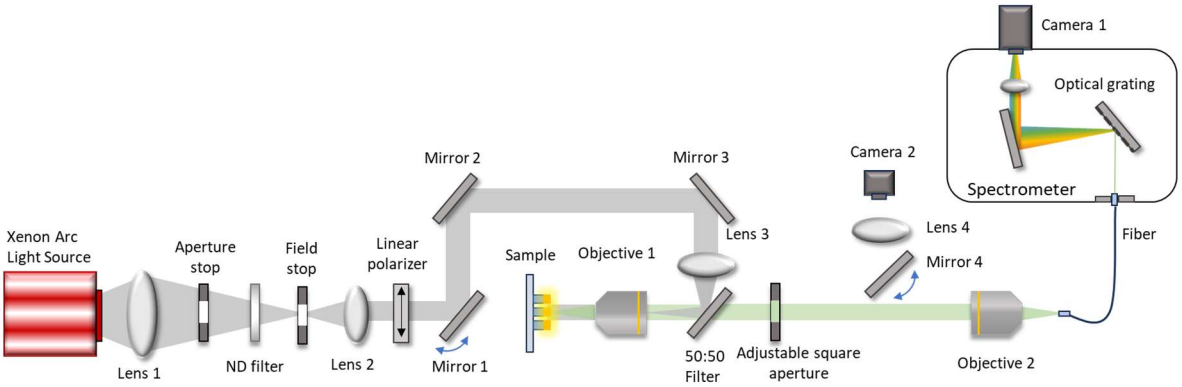

Figure 4.8 Optical layouts of micro-spectrophotometer for reflectance and transmittance measurement of Au-TiO_2 NPils

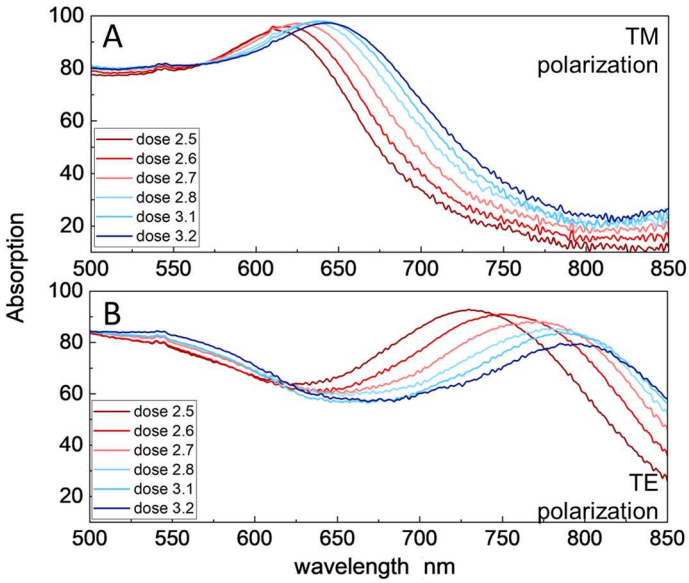

Figure 4.9 Measured absorption of Au-TiO_2 NPil arrays with various dose factor of EBL. The reference dose is 50 $\mu C/cm^2$. The radius increases with the dose factor and induces a redshift in peak wavelength under both TM and TE polarization.

The optical properties of Au-TiO_2 NPil arrays are firstly characterized to analyze as the function of the radius in the x- and y-directions. The Au-TiO_2 NPil arrays with increasing radius in both direction is fabricated with varying EBL doses factor as discussed in Section 4.2, Figure 4.5 and Table 4.1. As shown in Figure 4.9, the increase of NPil size with EBL does induces a redshift of the absorption peak under both TM and TE polarized light. For example, under TM mode, the peak wavelength red-shift from 610 to 655 nm as the average NPil radius R_x grows from 27 to 42 nm. Similarly, under TE mode, the radius R_y increase from 49 to 58 nm resulting in a peak wavelength shift from 730 nm to 810 nm. These absorption spectra shift highlight the morphology engineering contributed to plasmonic resonance wavelength corelated to catalytic

performance and behaving as the increase in total absorption. Also, by appropriately selecting the EBL dose, the absorption peak can be finely tuned to match the target resonance wavelength of MB reactions.

In the metasurface design with R_x = 35 nm and R_y = 60 nm, shown in Figure 4.10, the absorption spectrum under TM polarization (dark red curve) exhibits a peak near 650 nm with absorption reaching up to 97%. In contrast, under TE-polarized light, the larger radius in the y-direction induces a peak red-shifted to approximately 850 nm. These two plasmonic resonances, occurring at distinct wavelengths, correspond to the x- and y-components of the incident electric field, arising from the difference in the major and minor axis lengths of the Au-TiO_2 NPils. With the increase of polarization angle, the 650 nm resonance gradually diminishes, while a longer-wavelength resonance becomes more prominent, reaching its maximum under TE polarization. At the target reaction wavelength of 633 nm, tunable absorption is achieved, varying from 89% to 58% depending on the polarization angle. The most significant change occurs near a polarization angle of 45°, with the rate of variation decreasing as the angle approaches 0° or 90°, consistent with Malus' law.

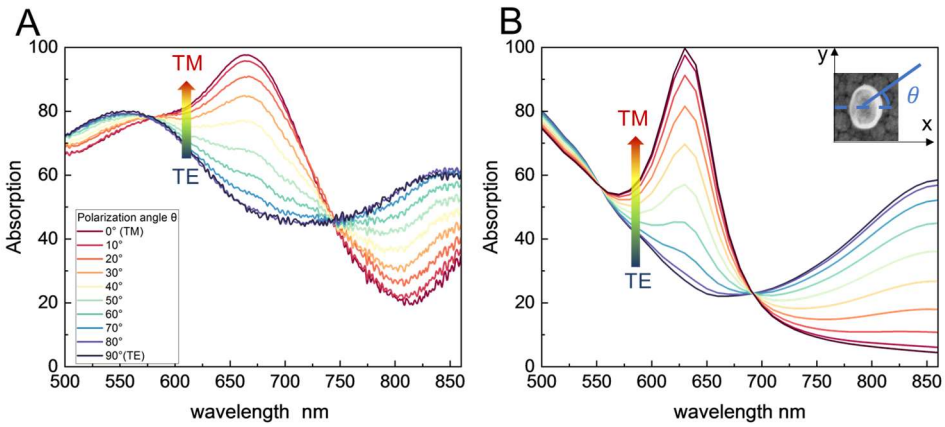

Figure 4.10 Total absorption of the Au-TiO_2 NPil array measured (A) with a micro-spectrophotometer under various polarization angles from 0° (dark red, TM) to 90° (dark blue, TE), compared with simulated spectra (B). The inset shows the definition of the polarization angle.

The simulated results for the Au-TiO_2 NPil array model with dimensions R_x = 35 nm and R_y = 60 nm exhibit spectra consistent with experimental measurements. The plasmonic resonance of the Au NDs primary contributes to absorption at 633 nm and shows a strong dependence on the polarization state of the incident light. Under TM polarization, the Au ND absorption reaches 96%, accounting for approximately 99% of the total absorption, demonstrating strong

near-field enhancement with potential for photocatalytic applications. A slight discrepancy in the absorption peak, shifting from 630 nm in simulations to 650 nm in measurements, is attributed to fabrication-induced dimensional variations. Furthermore, the measured spectra show FWHM broadening across all polarizations, which can be explained by several factors, including TiO_2 nanopillar tapering as evidenced in the simulations shown in Figure 4.7, dimensional variations within the array, and the finite size of the fabricated array compared to the infinite, perfectly periodic structure assumed in simulations. Despite these deviations, the Au-TiO_2 NPil metasurface exhibits pronounced polarization-dependent absorption and achieves tunability exceeding 30% at the target wavelength, primarily driven by the LSPR of the Au NDs.

Furthermore, achieving better alignment between the absorption peak wavelength and the resonance of the reactant molecules can further enhance polarization-dependent tunability. For instance, at the TM mode peak wavelength of 650 nm, the Au-TiO_2 NPil arrays modulate absorption from 52% (TE) to 97% (TM), enabling a tunability range of 45%. Similarly, at the TE mode peak wavelength 850 nm, absorption shifts from 61% (TE) to 27% (TM). Notably, the maximum absorption at 850 nm occurs under the polarization state perpendicular to that of the maximum at 650 nm, and *vice versa*. These characteristics highlight the strong potential of the metasurface for tuning catalytic reactivity. However, achieving precise control over the peak wavelength requires reducing fabrication-induced uncertainties, which inherently increases fabrication complexity.

4.3.2. MB reaction yield control on a single metasurface configuration

For photocatalysis characterization, the model reaction of MB degradation, occurring for MB molecules adsorbed onto the plasmonic-based metasurface, was used where light-induced cleavage of the C-N bond produces the reaction product. The reaction details and characterization procedures are described in Sections 2.3 and 2.4. The two primary non-thermal mechanisms in plasmonic photocatalysis, near-field enhancement and hot carrier transfer[26,110], enable tunable activation of specific chemical bonds, and facilitating the catalytic process. The reaction progress was *in-situ* monitored in real-time using SERS, which records the Raman spectra of samples under different polarization states. A 633 nm linearly polarized laser was employed as the excitation source, with the polarization angle adjusted by rotating the sample to 0°, 30°, 60°, and 90°. An Olympus LMPLFLN20X objective lens was used for focusing and signal collection, and a grating with 1200 lines/mm determined the spectral resolution of the

measured Raman spectrum. For temporal measurements, Raman signals were collected every 0.1 s over a total duration of 10 s.

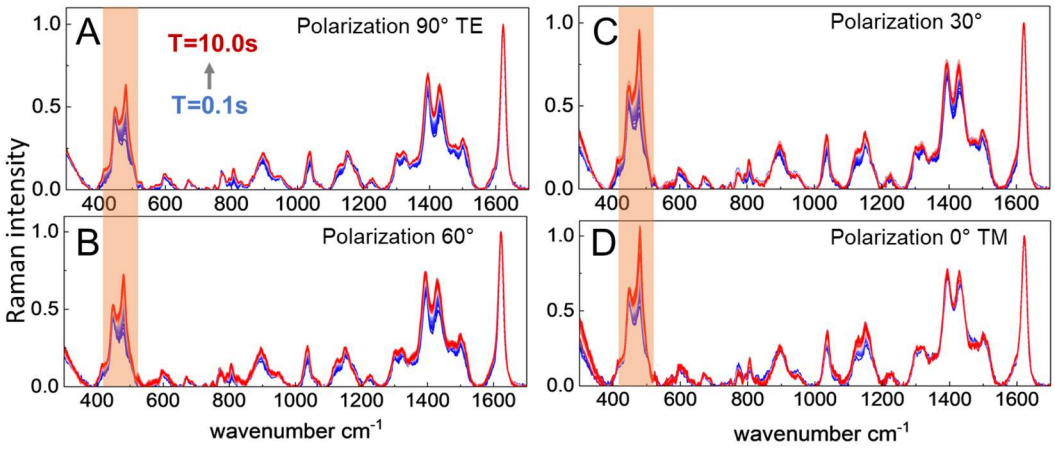

Figure 4.11 Temporal Raman spectra of Au-TiO_2 NPil arrays excited with a 633 nm laser in four polarization states: 90° (A, TE), 60° (B), 30° (C), and 0° (D, TM). Spectra were recorded at 0.1 s intervals over a 10 s period. The orange-shaded region highlights the wavelength range of interest (420 - 510 cm^{-1}) corresponding to characteristic features of the MB reaction.

The Raman spectra were post-processed by baseline removal and normalized to the C-C stretching peak of the benzene ring at 1622 cm^{-1}. The reaction product was identified and quantitatively analyzed by tracking its characteristic Raman peak at approximately 480 cm^{-1}. The normalized Raman spectra of the MB photocatalytic reaction under four polarization states are shown in Figure 4.11. In Figure 4.11A, illumination under TE mode produced a modest increase in the product peak, with Raman intensity rising from 0.40 to 0.65, indicating product formation with a limited rate. In contrast, under TM mode (Figure 4.11D), the Raman intensity increased more substantially, from 0.45 to 1.11, consistent with the stronger plasmonic resonance in the Au NDs. Intermediate polarization states at 30° and 60° also showed proportional increases in the product peak, reflecting the polarization-dependent enhancement of the catalytic reaction.

The temporal evolution of the product peak intensity was further analyzed *via* deconvolution fitting, as described in Section 2.4.2. For the Raman spectra of the Au-TiO_2 NPil arrays, the original reactant and product peaks were independently fitted, shown as the blue and orange curves in Figure 4.12. The total fitting error was maintained below 4%. The integrated area under each fitted curve was used as a quantitative measure of the MB photodegradation yield.

This time-resolved yield analysis provides further insight into the progression of photocatalytic reaction.

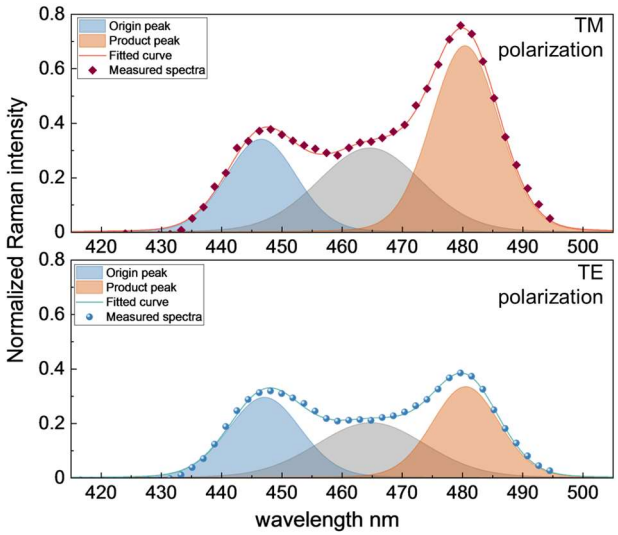

Figure 4.12 Peak fitting of the Au-TiO_2 NPil arrays at 10 s under TE (bottom) and TM (top) laser excitation. The reactant peaks (blue) and product peaks (orange) appear at approximately 445 and 480 cm^{-1}, respectively. The fitted curves (cyan and red), obtained from fitting to a three-peak structure, show strong agreement with the measured spectra (blue and dark red symbols), with residual errors below 4%.

Figure 4.13A presents the product yield as a function of reaction time, revealing the photocatalytic dynamics under four distinct polarization states: 0° (TM), 30°, 60°, and 90° (TE). Under TE polarization (dark blue dotted curve), the yield rises rapidly from 2.76 at 0.1 s to 3.89 within the first 3 s, then gradually levels off, reaching approximately 4.81 at 10 s. When the polarization is switched to the perpendicular TM mode (dark red curve), a similar temporal trend is observed; however, the final yield more than doubles, reaching 9.94. A reference yield was calculated with the Raman spectrum measured on Au mirror substrate under same illumination condition with TM mode. With the same illumination period in 10 s, the yield of this reference sample is only 0.19, attributing to the self-photodegradation. This clear enhancement correlates with the polarization-dependent absorption, indicating that the stronger plasmonic resonance under TM polarization directly contributes to the more than 50-fold increase in MB photodegradation yield compared with the reference sample after a 10 s period.

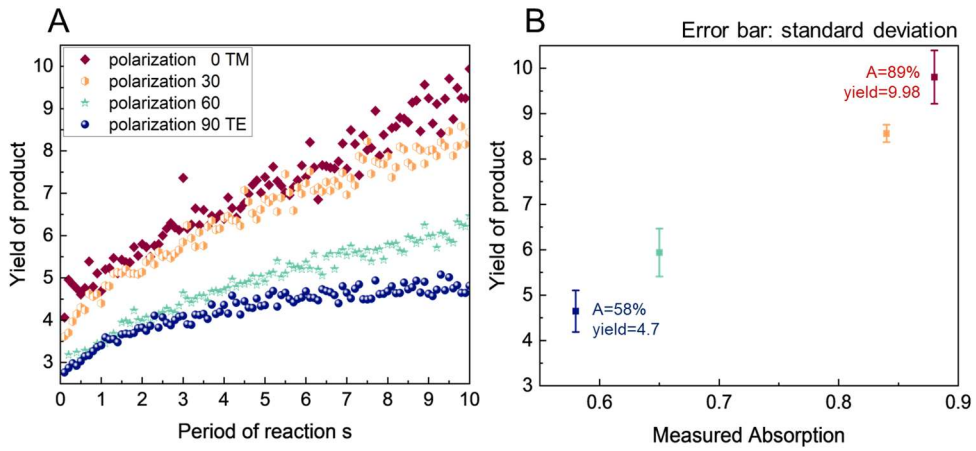

Figure 4.13 A) Reaction yield of Au-TiO_2 NPil arrays as a function of processing time for four polarization states. B) Average yield at the final timestep (t = 10 s) correlated with the measured absorption. Error bars represent the standard deviation from five measurements.

To further correlate the optical and catalytic behaviors, the average product yield at 10 s was plotted against the total measured optical absorption of the Au-TiO_2 NPil metasurfaces, as shown in Figure 4.13B. For each polarization state, five independent Raman measurements were taken at different positions on the metasurface. The corresponding time evolution of these yields is shown in Figure 4.14, confirming the stability of the end-product yield across repeated measurements. The standard deviations are indicated in Figure 4.13B calculated with the results of these five measurements as well. A pronounced tunability in catalytic yield is observed when switching the laser polarization from TE to TM, which gradually increases the plasmonic resonance strength evidenced by the absorption spectra. Under TM polarization, the yield reaches 9.98, driven by the strong LSPR at the target wavelength of 633 nm. Similarly, at 30° polarization, the yield rises to 8.6, approaching the TM value, demonstrating close agreement between the optical and catalytic responses. In contrast, for 60° polarization (green data point in Figure 4.13B), the absorption reduces to 65%, accompanied by a yield of 6.1. Under TE polarization, the photocatalytic reaction is suppressed, with the yield limited to 4.7 due to low plasmonic absorption. These results show that catalytic reactivity can be continuously tuned within our metasurface design by gradually rotating the light polarization, enabling precise control over reaction yield.

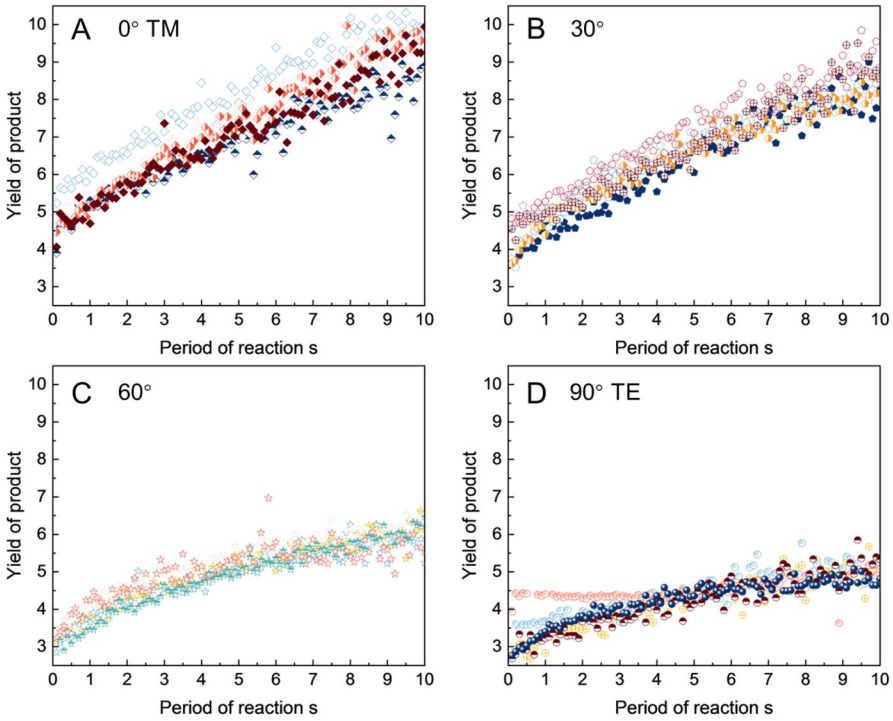

Figure 4.14 Reaction yield evolution of Au-TiO_2 NPil arrays over processing time under four polarization states: 0° (A), 30° (B), 60° (C), and 90° (D). For each polarization condition, five measurements were performed at different positions within the array, confirming the stability and reproducibility of the results.

These findings collectively demonstrate that the yield of the MB photocatalytic reaction can be dynamically modulated by the Au-TiO_2 NPil metasurface through optical tuning of the plasmonic resonance strength *via* polarization control of the incident light. The enhancement of plasmonic resonance, as revealed in the total absorption analysis at the target wavelength, provides direct insight into the catalytic activity. Morphological engineering enables the design of a metasurface to support strong near-field and hot-electron effects under TM polarization and to align with the electronic transition of MB (HOMO-LUMO gap), resulting in a significant enhancement of photocatalytic yield. Conversely, switching the polarization induces a misalignment between plasmonic and molecular resonances, red-shifting the plasmonic peak with increasing NPil radius and thereby reducing catalytic efficiency. As shown in Figure 4.13B, a proportional relationship exists between catalytic yield and measured optical absorption, highlighting the ability to gradually modulate reactivity through tunable optical properties. In the current model reaction (MB degradation), a slight mismatch remains between the metasurface peak resonance and the molecular resonance due to fabrication uncertainties. With improved alignment, an even greater tunability in catalytic yield is anticipated.

More broadly, the elliptical Au-TiO_2 NPil metasurfaces provide an effective reaction environment that not only adsorbs reactants[76,88] but also plasmonically tailors photocatalytic performance. The photocatalytic yield is actively controlled by modulating the strength of the LSPR. Reactant molecules typically adsorb onto the surfaces of Au NDs *via* van der Waals interactions, where they interact with incident photons or hot electrons. Achieving active control over such reactions requires metasurfaces with tunable properties enabled by specific structural designs. Here, we employed elliptical Au-TiO_2 NPil arrays that achieve resonance tunability through a highly compact, asymmetric morphology, while maintaining identical illumination conditions (*e.g.*, wavelength and power). The only variable is the polarization state of the incident light.

Beyond the current model system, the elliptical Au-TiO_2 NPil metasurface has the potential to extend the application to reactions with multiple competing pathways. By tailoring the morphology, the metasurface can be engineered so that its plasmonic resonances under TM and TE polarizations align with the molecular resonance energies of two reaction pathways[5,111]. Under TM polarization, the wavelength-dependent resonance can selectively catalyze reactions whose molecular resonances match the shorter-wavelength peak. Also, switching the polarization to TE shifts the resonance toward longer wavelengths while suppressing the original peak's intensity, thereby activating a different pathway and simultaneously suppressing the competing one enhanced under TM mode, which effectively promotes the selected pathways.

In summary, this wavelength-dependent plasmonic resonance enables selective enhancement of specific photocatalytic reactions while suppressing those that are spectrally misaligned within an elliptical Au-TiO_2 NPil array. Although periodic nanopillar array size constraint by the lithography technology, the optical property is predictable with simulation. Polarization-dependent tunability of the resonance peak offers a flexible strategy for continuously controlling reaction yields from 4.80 to 9.98 in 10 s period, with desired yields achievable through fine optical tuning—linearly correlated with catalytic performance. And this capability allows optical performance tailor targeting of two different wavelength ranges and selectively activated by orthogonal polarizations, each corresponding to distinct photocatalytic reactions with varied resonance molecule energies. A single metasurface configuration thus serves as a compact and versatile platform for selectively photocatalyzing reactions[31,40].

Chapter 5. Phase-change material in light-driven reactions

Phase-change materials offer a novel approach for designing tunable metasurfaces, which are applied to the manipulation of light-driven reactions. In this chapter, a phase-change material is employed as the nanocavity, coupled with the plasmonic resonance of a Au ND array, to actively tune the yield of aligned photocatalytic reactions. The tunable optical properties arise from refractive index modulation induced by switching the material between its amorphous and crystalline phases. A dynamic strategy is provided for controlling photocatalysis within a single metasurface configuration.

5.1. Background of phase-change materials

5.1.1.Phase-change material principles

Phase-change materials (PCMs) are emerging as promising candidates for tunable metasurface design, due to their reversibly switchable refractive index between amorphous and crystalline phase[112–115]. These materials exhibit sub-nanosecond switching ability and can maintain stable phase states at room temperature, making them suitable for dynamic optical modulation[116]. In light-driven reactions, PCM-based metasurfaces enable real-time tuning of the optical properties of nanostructures without the need for complex lithography-based adjustments[113,117]. This is achieved through the use of nanostructures with identical morphologies. In this study, we demonstrate that PCM thin films, when design as F-P cavities and coupled with plasmonic nanostructures, function as efficient and switchable photocatalytic materials.

Recently, various PCMs have gained attention as application-specific optical technologies due to their versatility and tunable optical properties. Their integration has shown significant promise in fields such as nanophotonics, metasurfaces, and neuromorphic photonics. For instance, $Ge_2Sb_2Te_5$ (GST) has been utilized in the development of switchable reflective color

display devices[118–120]. Another widely studied PCM, vanadium dioxide (VO_2), has been incorporated into photonic circuits owing to its relatively low phase transition temperature[121] and rapid electrical switching capabilities[122,123]. Additionally, antimony sulfide (Sb_2S_3) has demonstrated excellent potential as a solar cell material, attributed to its suitable bandgap of approximately 1.2 eV, strong visible-light absorption, and low toxicity[124].

For photocatalysis applications, we focus on the integration of Sb_2S_3 as a functional material within F-P cavities, where it serves to enhance light resonance and couple effectively with plasmonic nanostructures. The tunable refractive index of this material enables a spectral shift in the resonant peak wavelength, modulating the plasmonic resonance strength in a controllable resonator. The selection of Sb_2S_3 is primarily driven by its potential to enhance the resonance in the "switch-on" state and its favorable phase-switching tunability. Amorphous Sb_2S_3 (a-Sb_2S_3), owing to its relatively large bandgap, exhibits lower optical loss at the plasmonic resonance wavelength of gold nanostructures (~600 nm) compared to other PCMs[113,125]. Moreover, the significant refractive index contrast $|\Delta n|$[112,119,126] between the amorphous and crystalline phases introduces substantial tunability in the optical response. The crystallization switching time of Sb_2S_3, measured at approximately 70 ns, is comparable to that of GST, highlighting its potential for dynamic modulation in photocatalytic systems[113,127].

The enthalpy-structure order diagram of Sb_2S_3, presented in Figure 5.1, illustrates the fundamental principle of reversible phase switching. During crystallization, the material transitions from an amorphous state to an orthorhombic crystalline structure. Although the amorphous phase is thermodynamically less stable than the crystalline phase, the transition requires overcoming an energy barrier of approximately 2.0 eV [113]. This phase change process is governed by temperature- and time-dependent transformations[128]. Specifically, Sb_2S_3 must be heated above 573 K to surpass the activation energy barrier, followed by a sustained thermal treatment to promote crystal growth[113,128]. Conversely, during amorphization, crystalline Sb_2S_3 (c-Sb_2S_3) is heated beyond its melting point ($\sim 801\text{k} \pm 18\text{k}$) and then rapidly quenched to bypass recrystallization, resulting in an amorphous state[113].

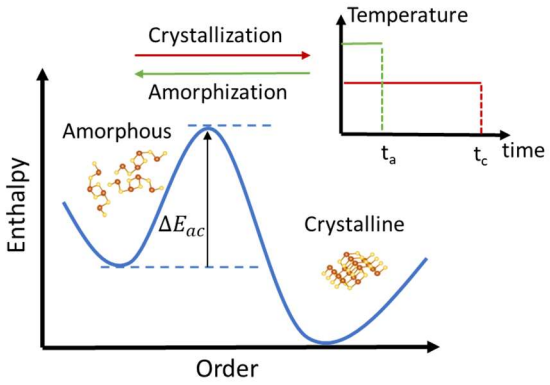

Figure 5.1 Enthalpy-order plot of a/c-Sb_2S_3 and temperature-time-dependent phase transformations: amorphization (green lines) and crystallization (red lines).

To investigate the phase transformations, both amorphous and crystalline Sb_2S_3 (a/c-Sb_2S_3) thin films (140 nm in thickness) were characterized using Raman spectroscopy before and after annealing crystallization. As shown in Figure 5.2, the Raman spectrum of the amorphous sample prior to annealing exhibits broad features centered around 70 and 290 cm^{-1}, corresponding to Sb-S and S=S vibrational modes, respectively[112]. Following annealing, the spectrum reveals sharper and more defined peaks associated with the symmetric groups A_g, notably at 70, 280, and 301 cm^{-1}, which are attributed to Sb-S stretching vibrations and $B1_g/B3_g$ modes. These features confirm the formation of the orthorhombic crystalline structure[129]. Thus, Raman spectroscopy verifies the phase transition induced by thermal treatment.

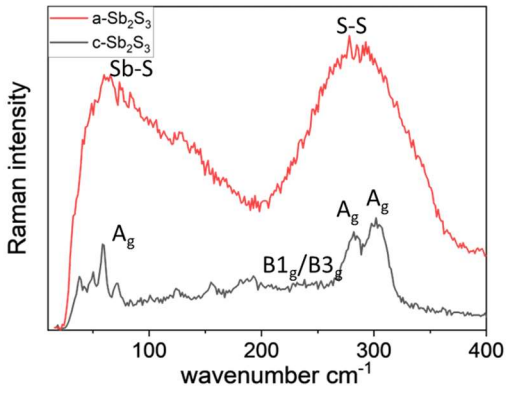

Figure 5.2 Raman spectra of amorphous (red) and crystalline (black) Sb_2S_3 before and after annealing

5.1.2.Thermal switching of Sb_2S_3 thin films

Based on the temperature- and time-dependent transformation principles illustrated in Figure 5.1, the crystallization process was investigated using a 160 nm a-Sb_2S_3 film deposited on an

Au mirror substrate. The a-Sb_2S_3 film was initially annealed with a hotplate at 300 °C for 30 min, following the recipe from previous studies[113,128]. However, after annealing, the Sb_2S_3 film became transparent, as shown in the inset of Figure 5.3C, and exhibited an increase in surface roughness exceeding 10 nm. It appears an outcome inconsistent with the expected optical properties from previous studies[126,127]. The SEM image in Figure 5.3C reveals the surface morphology of the annealed sample, where c-Sb_2S_3 appears crystalized and forms pyramid-shaped structures[129]. The Sb_2S_3 film is designed as a nanocavity and tunes the optical properties through mode hybridization. This discontinuous morphology poses challenges for its application as a resonance cavity in metasurface designs.

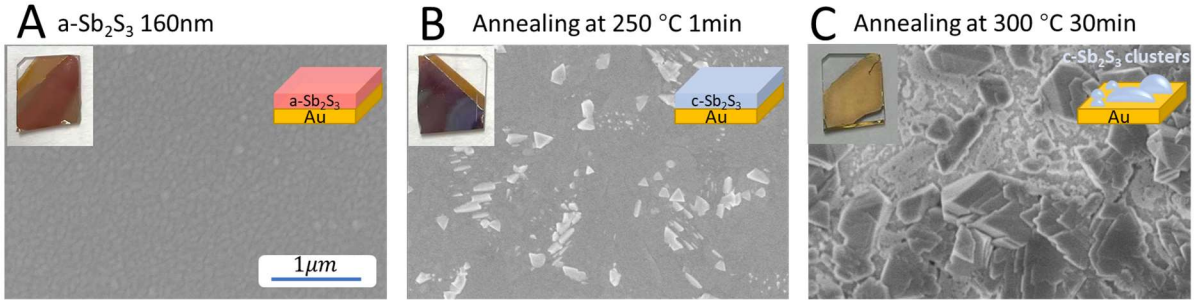

Figure 5.3 SEM images of 160 nm amorous Sb_2S_3 film before annealing (A), crystalline Sb_2S_3 film annealed at 250 °C for 1 min (B) and discontinued Sb_2S_3 crystal annealed at 300 °C for 30 min (C). The optical properties are various with Sb_2S_3 phases which induce the color difference in top left insets.

To address the issue of discontinued crystal during crystallization, the annealing temperature and duration were optimized to prevent the formation of discontinuous structures. As shown in Figure 5.3B, annealing the sample at 250 °C for 1 min resulted in a slight morphological change while maintaining a continuous and homogeneous Sb_2S_3 film. The difference in refractive index between amorphous and crystalline Sb_2S_3 induces a color change, attributed to a shift in the peak wavelength of the cavity's resonance. To further improve the annealing parameters, the morphology and structural evolution of the film were systematically characterized, as presented in Figure 5.4. The observed color changes in Figure 5.4A indicate that effective phase transformation occurs within the temperature range of 230 - 250 °C in 10 min. SEM images in Figure 5.4B-D reveal the morphology of the films at the various annealing temperatures. Based on these results, the optimal annealing condition for crystallization is determined to be 240 °C for 10 min, which ensures effective phase transformation while preserving a homogeneous film structure avoiding the formation of pyramid-shaped crystals.

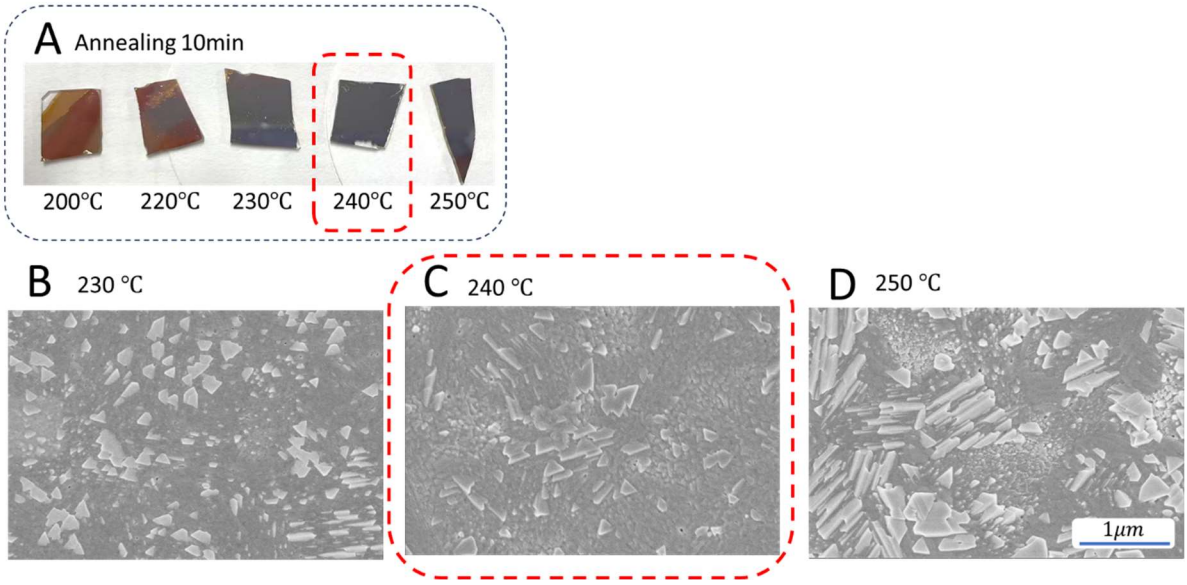

Figure 5.4 A) Sb_2S_3 film annealed at various temperatures from 200 to 250 °C in 10 min. The phase changes to crystalline with the temperature over 220 °C. SEM images reveal the crystalline Sb_2S_3 film annealed at 230 °C (B), 240 °C (C), 250 °C (D)

The crystallization process of a 140 nm a-Sb_2S_3 film deposited on an Au mirror substrate was monitored over time, as shown in Figure 5.5. Initially, the sample appears green due to F-P resonance effects (Figure 5.5A). Upon placement on a hotplate at 240 °C, the sample begins to change color induced by refractive index change, with red edge emerging at 1 min 9 s near the side closest to the center of the hotplate, as shown in Figure 5.5B. Due to the inherent temperature gradient of the hotplate, the phase transformation to c-Sb_2S_3 progresses gradually from the edge inward, and after 8 min, the entire sample appears red, indicating complete phase transformation (Figure 5.5D). To ensure a fully homogeneous crystalline phase, annealing was continued until 10 min, as confirmed in Figure 5.5E. The optical contrast between the amorphous and crystalline phases is clearly demonstrated through this color evolution (Figure 5.5F). The absorption spectra are further measured to analyze this optical property switching.

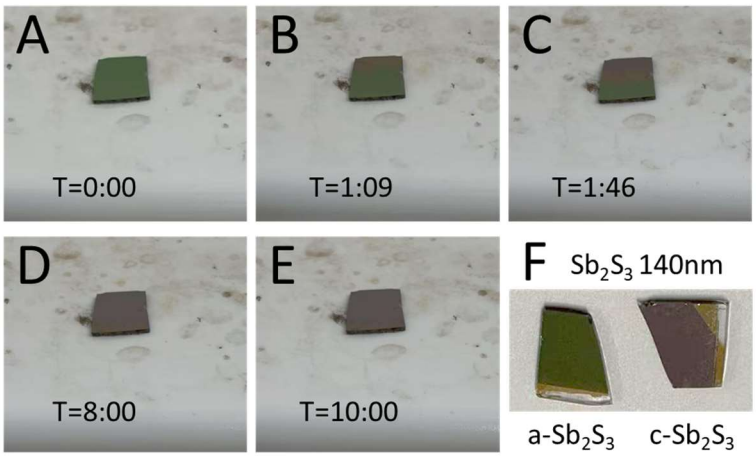

Figure 5.5 Annealing of a 140 nm Sb_2S_3 film at 240 °C in 10 min. Amorphous Sb_2S_3 shows in green (A). The phase change can be observed at 1 min 9 s at the side close to the center of the hotplate (B) and graduate to the other side (C). The sample completed to switch to the crystalline phase at 8 min (D). The annealing process ends at 10 min (E). The amorphous and crystalline Sb_2S_3 shows the color difference (F) due to different spectral peak positions.

5.1.3.Optical properties of amorphous/crystalline-Sb_2S_3

The refractive index of Sb_2S_3 in both amorphous and crystalline phases was measured across the wavelength range of 400 - 1600 nm using spectroscopic ellipsometry on 160 nm film samples, as shown in Figure 5.6. The results, represented by dash-dot curves for the amorphous phase and solid curves for the crystalline phase, reveal differences in both the real part (n, shown in red) and the imaginary part (κ, shown in blue) of the refractive index, which directly influence the resonance modes and absorption coefficients. In the wavelength range above 600 nm, the c-Sb_2S_3 exhibits a higher refractive index than the amorphous phase. At the target wavelength of 633 nm, the refractive index of a-Sb_2S_3 is approximately 3.1, resulting in a refractive index contrast $|\Delta n|$ greater than 1.0 compared to the crystalline phase. Additionally, the imaginary part κ indicates the material absorption during phase transformation. For a-Sb_2S_3, peak absorption occurs within the visible range, with an absorption cutoff near 650 nm. Upon crystallization, the κ spectrum exhibits a redshift due to the change in bandgap, extending the cutoff wavelength to approximately 910 nm. This distinct refractive index contrast between a/c-Sb_2S_3 enables tunable optical properties, which is advantageous for switchable photonic applications.

To investigate the effect of this refractive index variation on the optical behavior, simulations were conducted using COMSOL Multiphysics. A unit cell model was constructed consisting

of a thin Sb_2S_3 film deposited on a Au mirror substrate, forming a semi-open optical cavity, as illustrated in Figure 5.7A and B. The thickness of the Sb_2S_3 film was swept from 20 - 300 nm to tune the F-P resonance peak wavelength supported within the cavity. As shown in Figure 5.7A, the F-P resonance peak exhibits a redshift with increasing a-Sb_2S_3 film thickness. Resonances are observed at $h_{a\text{-}Sb2S3}$ = 32 nm (F-P resonance order m = 1) and $h_{a\text{-}Sb2S3}$ = 127 nm (F-P resonance order m = 2), corresponding to a target wavelength of 630 nm. However, the total absorption at these first- and second-order resonance modes is limited to 31% and 51%, respectively, due to the absorption cutoff of a-Sb_2S_3 near 650 nm. In these cases, the observed absorption primarily originates from the Au mirror layer. A stronger absorption peak is evident at wavelengths below 600 nm, where the material absorption coefficient of a-Sb_2S_3 is more significant.

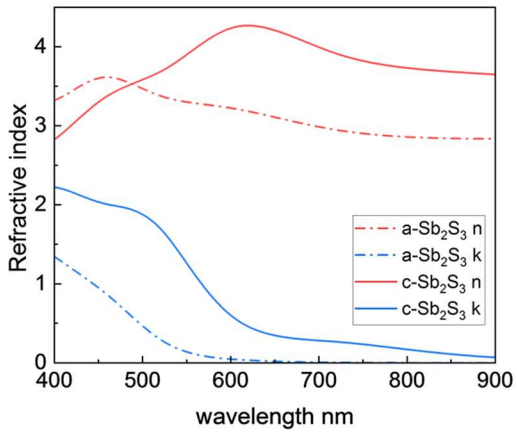

Figure 5.6 Refractive index of amorphous (dash-dot curves) and crystalline (solid curves) Sb_2S_3 with real part n in red and imaginary part κ indicating material absorption in blue.

In the simulation results for c-Sb_2S_3, the peak wavelengths of the cavities shift compared to the amorphous sample due to differences in the refractive index. At the target wavelength of 630 nm, peak absorptions occur at $h_{c\text{-}Sb2S3}$ = 20 nm (m = 1) and $h_{c\text{-}Sb2S3}$ = 96 nm (m = 2), corresponding to the first two F-P resonance modes, as shown in Figure 5.7B. Due to the extended absorption range of c-Sb_2S_3, the absorption increases significantly, reaching 78% and 91% for the first- and second-order modes, respectively. Strong cavity resonances are observed throughout the wavelength range below 760 nm, where the imaginary part κ of the refractive index remains substantial, indicating efficient optical absorption in the crystalline phase.

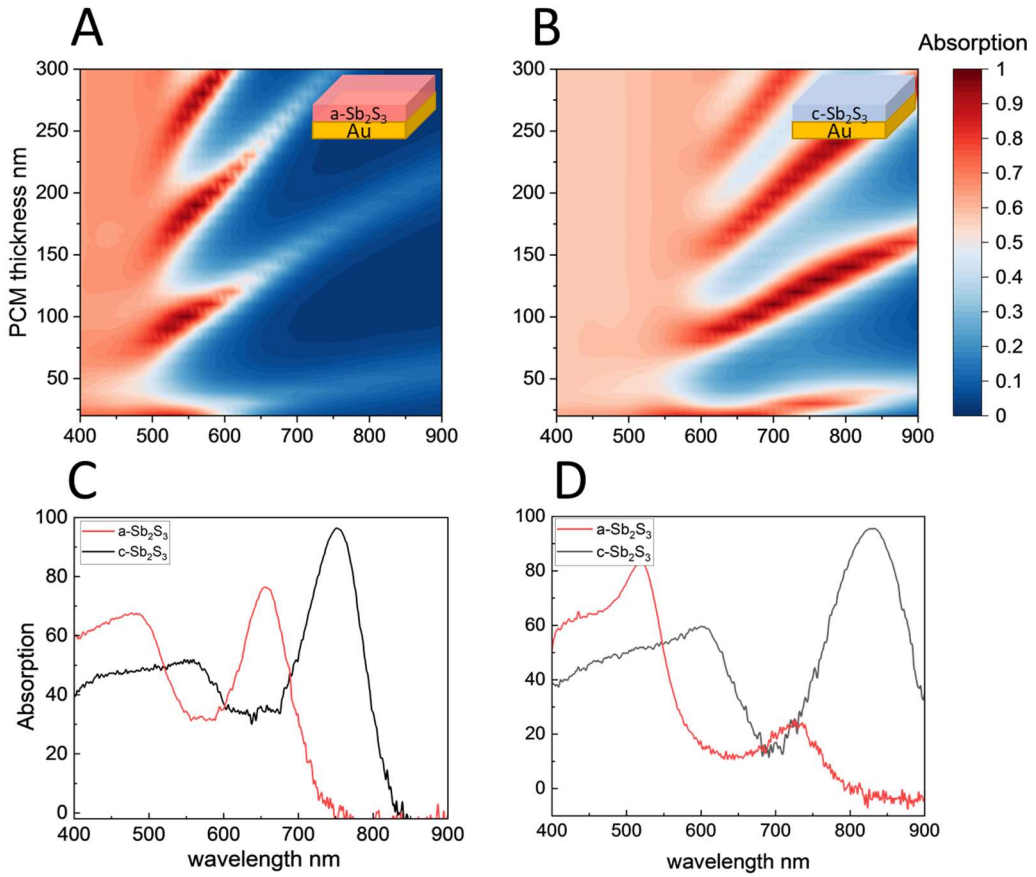

Figure 5.7 Simulated total absorption against amorphous (A) and crystalline (B) Sb_2S_3 film thickness on Au mirror substrate. The measured absorption of the Sb_2S_3 film samples is compared in two phases with h_{Sb2S3} = 140 nm (C) and 160 nm (D)

For the design of PCM cavities, the total absorption spectra were measured for samples with Sb_2S_3 film thicknesses of 140 and 160 nm, as shown in Figure 5.7C and D. The measurements were performed using a micro-spectrophotometer over the wavelength range of 400 - 900 nm, and spectra were compared for both the amorphous and crystalline phases. In the sample with h_{Sb2S3} = 140 nm, the absorption peak red-shifts from 653 nm in the amorphous phase to 751 nm in the crystalline phase, with corresponding absorption values of 76% and 96%, respectively. At the target wavelength of 630 nm, the absorption is modulated from 62% (amorphous) to 33% (crystalline), demonstrating effective tunability. Similarly, for the h_{Sb2S3} = 160 nm sample, the peak wavelength shifts from 740 to 882 nm upon phase transformation. However, in this case, the absorption in the amorphous phase is only 24% at 740 nm, beyond its absorption cutoff, resulting in poor alignment with the target wavelength and reduced efficiency.

The a-Sb_2S_3 cavity is specifically designed to enhance the photocatalytic reaction at 633 nm, minimizing cavity absorption losses based on the lower imaginary part κ of the refractive index, as shown in Figure 5.6. Upon crystallization, the resonance of the cavity red-shifts, weakening the plasmonic resonance due to detuning from the coupling condition. The c-Sb_2S_3 cavity are expected to actively suppress the cavity resonance and reduce the plasmonic resonance *via* mode hybridization with destructive node at this target wavelength. This phase-dependent shift enables dynamic modulation of optical properties through reversible phase switching, offering a pathway for tunable metasurface functionality.

5.2. Integrating Au nanodisk arrays on an Sb_2S_3 cavity

5.2.1. Design tunable metasurface with Au ND coupled Sb_2S_3 cavity

To integrate the PCM into a tunable metasurface, we designed an array of Au NDs coupled to an Sb_2S_3 optical cavity, as illustrated in Figure 5.8. An Sb_2S_3 film is designed on a 200 nm thick Au mirror layer with glass slide substrate, forming a semi-open cavity due to the high reflection at the interface between Au and Sb_2S_3 film. The thickness of the Sb_2S_3 layer is precisely tailored to engineer the desired resonance wavelength. A Au ND array is then developed on the Sb_2S_3 cavity, with a ND radius ($R_{Au\ ND}$) of 55 nm and an array periodicity ($a_{Au\ ND}$) of 150 nm. The LSPR of the Au NDs is designed with these two parameters to align with the resonance wavelength of the photocatalytic model reaction molecules specifically, for the MB degradation reaction with a 633 nm laser. The plasmonic resonance of the Au NDs is designed to strongly couple with the F-P resonance of the Sb_2S_3 cavity to enable modulation of the optical properties, thus achieve catalytic behavior controls.

Tuning the cavity resonance wavelength offers an effective strategy for controlling the strength of the plasmonic resonance through the mode coupling. In the design of the Au nanodisk-Sb_2S_3 cavity (Au ND-Sb_2S_3 cavity), the F-P resonance shifts as a result of refractive index changes induced by the phase transformation of Sb_2S_3, as demonstrate in the simulation and measured results in Figure 5.7. The optical tunability of Au ND-Sb_2S_3 cavity in both phases were analysis with *COMSOL Multiphysics* as well. The total absorption spectra were calculated as a function of cavity thickness, as illustrated in Figure 5.9A and B, while maintaining the design parameters of the Au ND array ($R_{Au\ ND}$ = 55 nm and $a_{Au\ ND}$ = 150 nm). Compared to simulations results of the PCM film only, the Au ND array extends the absorption range due to the LSPR,

covering the plasmonic resonance region of gold up to approximately 900 nm. The plasmonic resonance of the Au ND array is centered around 660 nm which is close to the target wavelength for the photocatalytic reaction. This wavelength is primarily determined by the parameters of the Au NDs, such as radius and array periodicity.

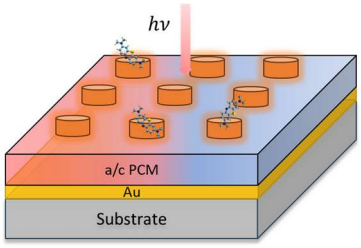

Figure 5.8 Au ND array coupled on Sb_2S_3 cavity which can shift its phase between amorphous and crystalline. The reactant molecules are adsorbed on the Au ND surface.

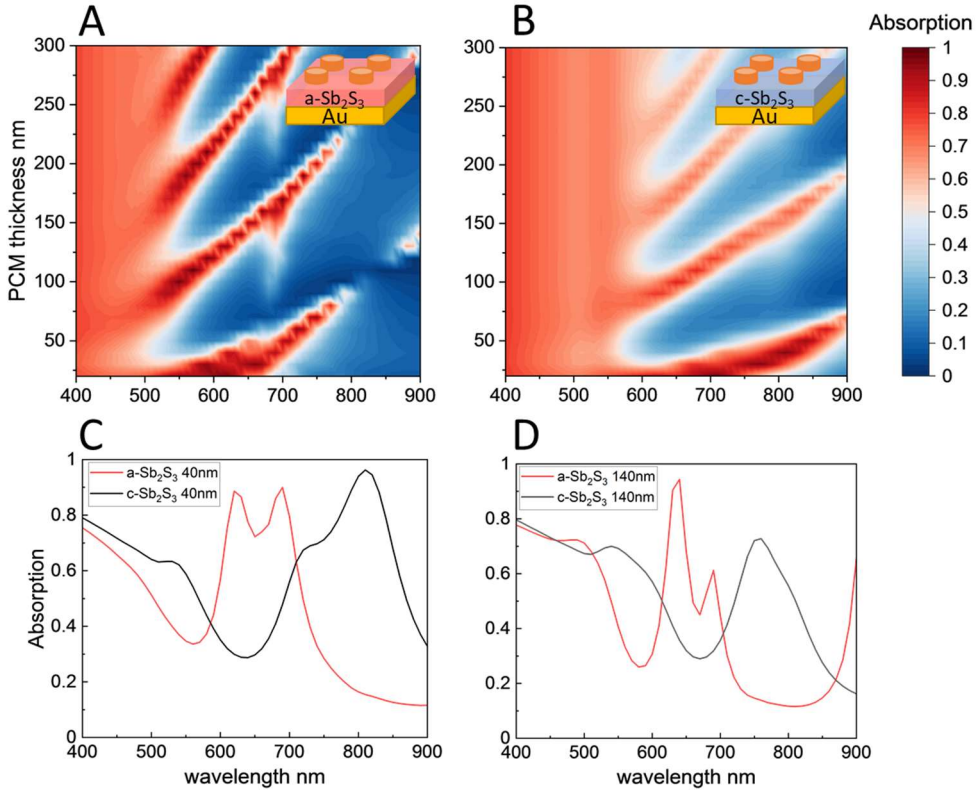

Figure 5.9 Simulated total absorption of Au ND-Sb_2S_3 cavity against amorphous (A) and crystalline (B) cavity thickness. The absorption is compared in the different phases for h_{Sb2S3} = 40 nm (C) and 140 nm (D)

In the amorphous configuration, this plasmonic resonance hybridizes with the F-P cavity resonance at particular Sb_2S_3 thicknesses, notably at h_{Sb2S3} = 40 nm and h_{Sb2S3} = 140 nm, corresponding to the first and second F-P resonance modes near the target wavelength. Spectral

splitting at these hybridization points indicates strong coupling between the LSPR and the cavity mode, enhancing the plasmonic response due to mode hybridization at constructive interference peak of this cavity. The plasmonic resonance strength is tunable with shifting of the cavity resonance. In contrast, for the c-Sb_2S_3 configuration, the refractive index change shifts the cavity resonance, and the higher absorption coefficient at the target wavelength (633 nm) also leads to significant optical losses. As a result, the spectral energy splitting is diminished, indicating weaker mode hybridization due to increased cavity absorption. The comparison clearly demonstrates a substantial change in absorption between amorphous and crystalline phases under the same structural design, highlighting the tunable optical properties at more than one wavelength ranges enabled by the phase transformation of Sb_2S_3.

The thickness of the Sb_2S_3 cavity is designed to match the coupled wavelengths of the first two F-P resonance modes in the amorphous phase, which means that samples with cavity thickness of h_{Sb2S3} = 40 nm and h_{Sb2S3} = 140 nm were designed. As shown in Figure 5.9C and D, effective mode hybridization is observed in both a-Sb_2S_3 metasurfaces. At the target wavelength of 630 nm, the absorption peaks reach 80% and 90% for the 40 nm and 140 nm thick samples, respectively. The coupling strength, Ω, is determined with the difference of two peak frequencies, which are 56.9 GHz (h_{Sb2S3} = 40 nm) and 40.1 GHz (h_{Sb2S3} = 140 nm), respectively. These absorption values can be actively tuned through the crystallization process. For the metasurface with h_{Sb2S3} = 40 nm, the resonance peak red-shifts to 810 nm in the crystalline phase, reducing the absorption at 630 nm to 29%. Similarly, in the h_{Sb2S3} = 140 nm sample, the peak red-shifts to 760 nm, resulting in a decrease in absorption at 630 nm from 90% to 41%. This tunability enables optical switching, which effectively tailors absorption at the target wavelength ‘on’ or ‘off’ through reversible phase transformation between a-Sb_2S_3 and c-Sb_2S_3. A similar trend can also be observed in the simulated spectra of the two non-thermal effects of LSPR, which are illustrated in Appendix 8. The electron population in the occupied molecular orbitals demonstrates the catalytic activity which is direct reflected in these two parameters. Notably, as a regional material phase switching can be achieved in sub-nanosecond scale, the metasurface has the potential to integrate with local temperature control approaches, which enable dynamically ‘switch on’ or ‘switch off’ in real-time to tailoring in plasmonic resonance.

Moreover, with the redshift of the cavity resonance in the crystalline phase, the metasurface can potentially catalyze reactions aligned with the new resonance peaks at 810 nm or 760 nm. Considering the availability of laser sources commonly used in photocatalytic characterization

with SERS, such as the 785 nm laser, the design can be adapted to target new reactions at this wavelength. For instance, in the h_{Sb2S3} = 40 nm sample, absorption at 785 nm increases from 19% (amorphous) to 83% (crystalline), while the h_{Sb2S3} = 140 nm sample shows an increase from 12% to 64% following crystallization. This capability enables selective activation of more than one distinct photocatalytic reactions, each operating in different spectral regions and controlled *via* phase transformation.

5.2.2.Fabrication of Au ND arrays on Sb_2S_3 cavity

The Au ND-Sb_2S_3 cavity was fabricated with a top-down lithographic process, as outlined in Figure 5.10. A 200 nm Au mirror layer was deposited onto a glass substrate using a Temescal BJD-2000 E-beam evaporator. The Sb_2S_3 cavity film was then deposited *via* thermal evaporation to the target thickness, forming an amorphous-phase film. To obtain crystalline-phase samples, the amorphous films were subsequently annealed at 240 °C for 10 min to induce phase transformation. The film thickness (h_{Sb2S3}) and surface roughness, which determines the F-P cavity resonance, was measured with ellipsometry both before and after annealing, as summarized in Table 5.1. The thickness change of the Sb_2S_3 cavity due to the crystallization process is negligible. The surface roughness is slightly increased in crystalline-phase samples, because the surface tension might increase in the crystalline structure. A greater thickness of the Sb_2S_3 cavity induce a larger surface tension, which in turn raises surface roughness and may degrade the quality of the F-P cavity resonance.

Table 5.1 Measured thickness and surface roughness of Sb_2S_3 film before and after annealing

NO.	Phase	Designed thickness nm	Measured thickness nm	Measured roughness nm
1	a- Sb_2S_3	40	39 ± 0.2	< 1 nm (0.2)
	c- Sb_2S_3	40	37 ± 0.2	< 1 nm (0.1)
2	a- Sb_2S_3	140	135 ± 0.1	< 1 nm (0.1)
	c- Sb_2S_3	140	131 ± 0.1	1.3
3	a- Sb_2S_3	160	162 ± 0.2	< 1 nm (0.1)
	c- Sb_2S_3	160	162 ± 0.5	4.3

Furthermore, the a/c-Sb_2S_3 cavity samples were patterned with Au ND arrays using EBL on a bilayer PMMA resist under a controlled electron beam dose. Precise dose selection was critical to ensure high-quality pattern definition. Subsequently, a 40 nm Au film was deposited to form

the ND arrays. The photoresist was then removed by immersing the samples in acetone for over six hours. Finally, the samples were immersed overnight in particular dye solution to facilitate molecular attachment onto the Au NDs.

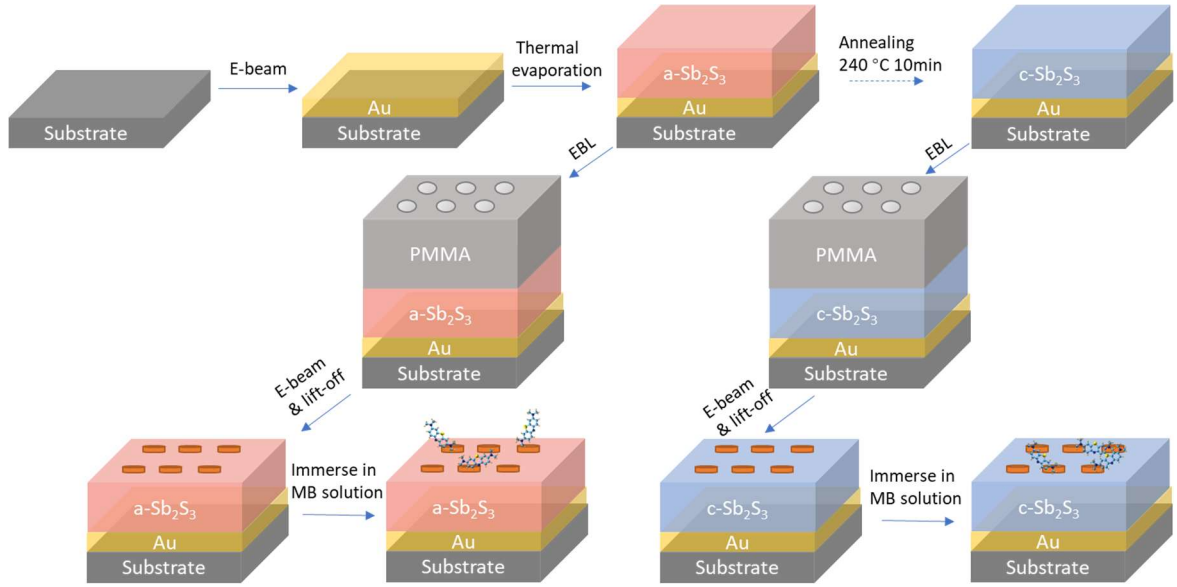

Figure 5.10 Fabrication process of Au ND-Sb_2S_3 cavity. The thermal evaporated Sb_2S_3 cavity is deposited with Au ND array. The Sb_2S_3 cavity switches to crystalline with annealing at 240 °C in 10 min and is deposited with Au ND array.

During the lift-off process of the photoresist, the strong metallic bonding characteristic of gold adversely can affect the complete removal of residual Au films. As illustrated in Figure 5.11A, residual gold adhering to the ND surfaces results in morphological defects that degrade the plasmonic resonance. This phenomenon is attributed to the EBL step, as depicted in Figure 5.11B. Electron beam scattering can induce a tapered profile with inclined sidewalls in the photoresist[130]. During deposition *via* E-beam evaporation, the Au film coats both the horizontal and sidewall surfaces of the photoresist because of the scattering, leading to the formation of continuous gold films that resist lift-off. To mitigate this issue, a higher acceleration voltage of 120 kV is employed during EBL to offer a more vertical sidewall and disrupt metallic bonding between NDs. And the ultrasonic cleaning is applied in lift-off step to assist with removing residual Au film. These adjustments effectively facilitate the complete removal of residual Au, enhancing the structural integrity and optical performance of the ND arrays.

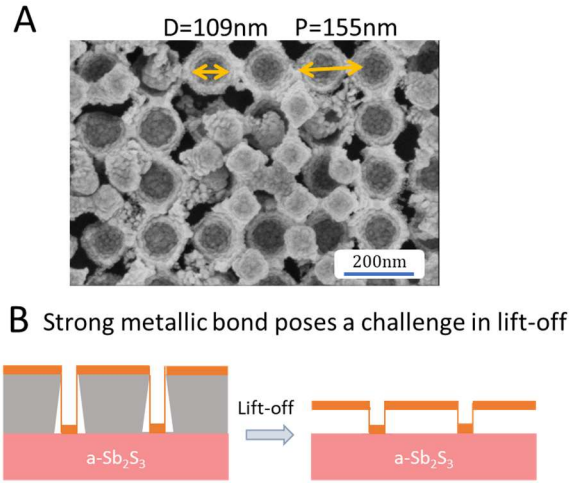

Figure 5.11 Fabrication defects in lift-off step. The strong metallic bond of gold challenges the removal of the residual gold film.

Moreover, the morphology of the Au NDs was analyzed with SEM across various electron-beam doses in EBL, as shown in Figure 5.12. With the increased EBL acceleration voltage, the residual Au was effectively removed, resulting in well-defined and uniform ND arrays. A slight variation in optimal electron-beam dose was observed between the a- and c-Sb_2S_3 phase samples, attributed to their different electrical conductivities. Especially, the ND array structures were fabricated within an electron-beam dose range of 650 - 700 $\mu m/cm^2$ for a-Sb_2S_3, and 725 - 775 $\mu m/cm^2$ for c-Sb_2S_3. While electron-beam doses are able to influence ND dimensions, the average ND radius does not reveal a significant difference across the effective dose ranges, which has approximately 59 nm for a-Sb_2S_3 and 58 nm for c-Sb_2S_3, as summarized in Table 5.2. Although the samples in each phase were patterned independently through separate EBL processes, the morphological variation between them is negligible. Therefore, the samples can be employed in investigating the tunability in optical performance attributed to the refractive index contrast between the amorphous and crystalline phases, rather than fabrication-induced discrepancies.

Table 5.2 Measured average radius of Au NDs in amorphous and crystalline Au ND-Sb_2S_3 cavities samples with various EBL doses

a-Sb_2S_3 EBL dose $\mu C/cm^2$	650	675	700
Average radius nm	59.5	59.1	59.2
c-Sb_2S_3 EBL dose $\mu C/cm^2$	725	750	775
Average radius	58.1	58.0	58.7

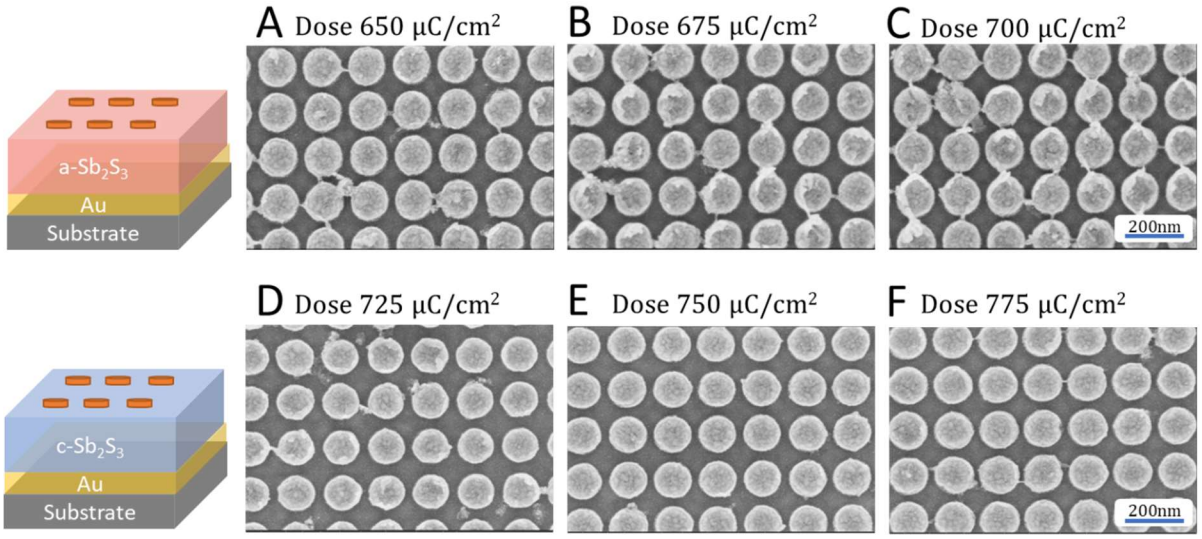

Figure 5.12 SEM images of Au ND-Sb_2S_3 cavities in amorphous phase are shown with EBL dose in 650 $\mu m/cm^2$ (A), 675 $\mu m/cm^2$ (B) and 700 $\mu m/cm^2$ (C). Au ND-Sb_2S_3 cavities in crystalline phase are shown with EBL dose in 725 $\mu m/cm^2$ (D), 750 $\mu m/cm^2$ (E) and 775 $\mu m/cm^2$ (F).

To demonstrate the dynamic tuning capability of the Au ND-Sb_2S_3 cavity sample, SEM images were taken before and after thermal annealing to assess the thermal stability of the Au ND array, as shown in Figure 5.13. The crystallization conditions applied to transform a-Sb_2S_3 did not alter the morphology of the ND array, confirming the thermal stability of the plasmonic metasurface. This result verifies that the nanostructure remains intact under the thermal conditions required for phase switching. Although dynamic phase switching is feasible, this study primarily focuses on evaluating the photocatalytic potential enabled by the tunable refractive index of the PCM. To ensure consistent and ideal characterization conditions for photocatalytic reactions, the Au ND arrays were fabricated through two independent EBL processes, corresponding to the amorphous and crystalline samples. Precise temperature control is also crucial in achieving dynamic modulation of the reaction yield, such as with laser induce heating and Joule heating, which can effectively control the local thermal distribution and improve the switching speed.

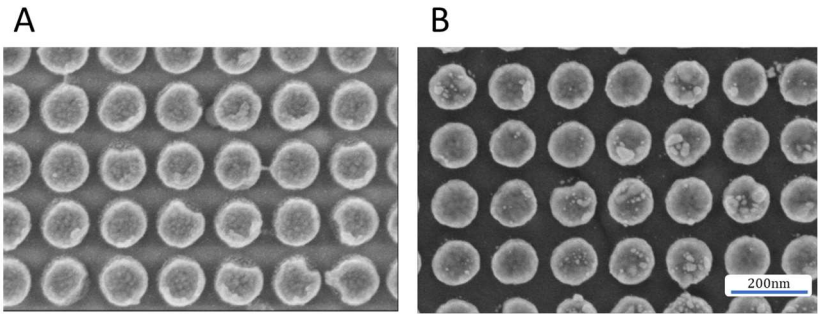

Figure 5.13 SEM images of Au ND arrays before (A) and after (B) annealing. The morphology of the array is kept stable during the crystallization.

5.3. Optical and catalytic manipulation of Au nanodisk-Sb_2S_3 cavity

5.3.1.Tunable optical properties of Au ND-Sb_2S_3 cavity

The optical properties of both amorphous and crystalline samples were measured using a micro-spectrophotometer with a similar optical layout in Figure 3.13. Figure 5.14A and B present the absorption spectra, illustrating the tunability of the optical response induced by phase switching in Au ND-Sb_2S_3 cavity samples with a cavity thickness of 40 nm. The measurements were conducted over a patterned area of $100\ \mu m \times 100\ \mu m$, defined by the ND array.

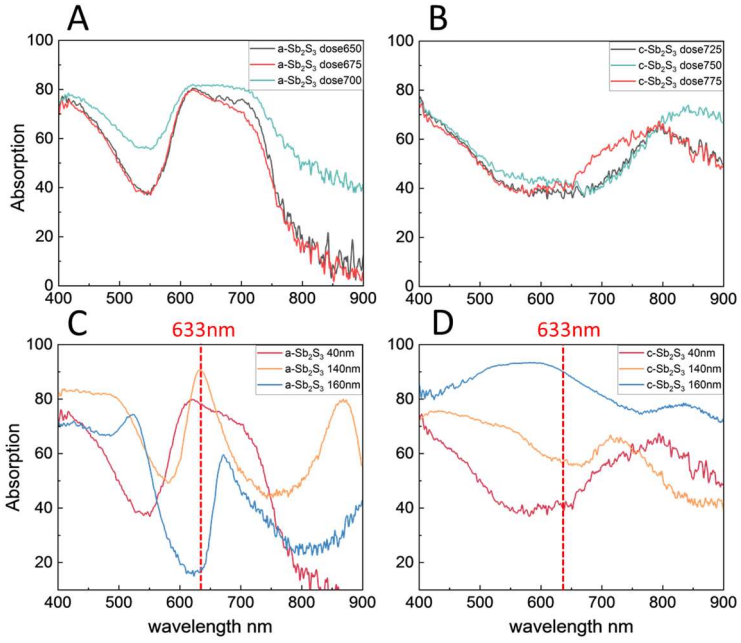

Figure 5.14 Measured total absorption of Au ND-Sb_2S_3 cavities in amorphous (A) and crystalline (B) phase with various EBL doses. The total absorption spectra are shown against Sb_2S_3 thickness 40 (red), 140 (yellow) and 160 (blue) nm in the two phases (C and D).

For the amorphous samples, significant absorption is observed in the wavelength range of 600 - 700 nm, as shown in Figure 5.14A. This response arises from the coupling between the LSPR of the Au NDs and the F-P resonance of the a-Sb_2S_3 cavity, resulting in spectral peak splitting and the appearance of dual absorption peaks. Variations in the electron beam dose of EBL slightly affects the peak positions and spectral shapes due to minor changes in ND morphology. The sample fabricated with a $675\ \mu C/cm^2$ dose exhibits strong absorption at the target wavelength for MB reactions, reaching 78%. The sample fabricated with a $700\ \mu C/cm^2$ dose shows enhanced absorption beyond 750 nm, attributed to fabrication-induced defects that reduce inter-disk gaps. However, the other two samples show limited absorption in this spectral region.

For the crystalline samples, the absorption peak red-shifts to approximately 800 nm, as shown in Figure 5.14B, consistent with the refractive index change upon crystallization. In the sample fabricated with a $775\ \mu C/cm^2$ dose, absorption at the original target wavelength (633 nm) decreases to 39%. However, this sample exhibits 68% absorption at that wavelength 800 nm enabling the potential application of this metasurface in photocatalytic reactions operating at this wavelength, which was selected for subsequent photocatalysis experiments. Slight spectral variations across different doses are observed due to changes in ND geometry and periodicity, which is negligible.

A similar phenomenon is observed in the sample with an Sb_2S_3 cavity thickness of 140 nm, where the plasmonic resonance of the Au NDs is coupled with the second-order F-P resonance mode (m = 2). In the amorphous state, Figure 5.14C, the sample exhibits a tunable absorption peak of 95% at the target wavelength of 633 nm, which decreases to 59% upon phase transformation to the crystalline state, see Figure 5.14D. As the nanocavity thickness increases, the resonance peak redshifts; in the amorphous sample with a thickness of 160 nm, the peak shifts to 665 nm. This shift aligns the F-P resonance node with the desired reaction wavelength. Considering the tunability across all available laser wavelengths applied for photocatalytic characterization, the Au ND-Sb_2S_3 cavity is ultimately designed with a cavity thickness of 40 nm to optimize resonance alignment and switching performance.

In Figure 5.15, the absorption spectra of the Au ND-Sb_2S_3 cavity with a cavity thickness of 40 nm are compared in both the amorphous and crystalline phases, highlighting the optical tunability achieved through phase transformation. At the target wavelength for MB

photocatalytic reactions (633 nm), the absorption decreases from 78% in the amorphous state to 39% in the crystalline state following crystallization. The measured absorption spectra exhibit a trend consistent with the simulation results. However, peak splitting observed in simulations is less pronounced in the experimental data, which may be attributed to the fact that the spatial mode distribution is not perfectly superposed caused by fabrication uncertunity[35]. Rather than displaying distinct dual peaks, the amorphous samples exhibit a broadened absorption band, indicating enhanced plasmonic resonance near the F-P resonance peak. Especially, at the peak wavelength of c-Sb_2S_3 metasurface, a considerable discrepancy occurs between simulation and experimental results which reduce the peak of absorption at about 800 nm. A possible reason is that the F-P resonance strength is weaker than expected due to the roughness increased at the interface of cavity and air, which reduces the quality of resonance and coupling.

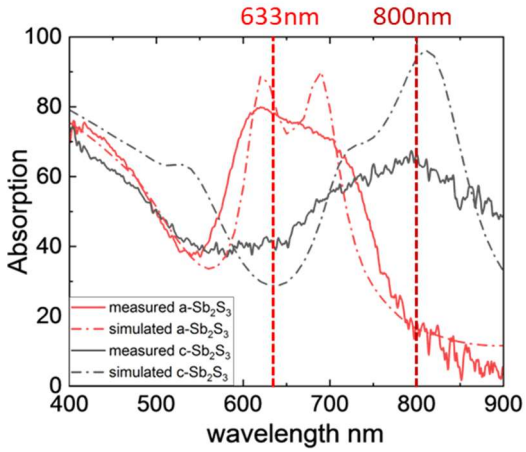

Figure 5.15 Measured (solid lines) and simulated (dash dot lines) absorption of amorphous (red) and crystalline (black) Au ND-Sb_2S_3 cavities with h_{Sb2S3} = 40 nm.

Additionally, at another peak wavelength at 800 nm, the crystalline Au ND-Sb_2S_3 cavity shows an enhancement in absorption of 68%, which is reduced to 17% upon amorphization. It provides another potential wavelength for photocatalysis manipulation. The absorption can be tune in the range of 51% which can be employed in catalyzing aligned reaction, and an excellent manipulation in reactivity can be expected due to this significant variation. Overall, the h_{Sb2S3} = 40 nm Au ND-Sb_2S_3 cavity is optimized to support tunable absorption across a range of operational wavelengths, demonstrating strong potential for dynamically catalyzing diverse light-driven reactions.

5.3.2. Yield Control of MB degradation reaction

For catalytic performance characterization, real-time Raman spectroscopy is employed to monitor the reaction process and quantitatively analyze product yield, following the methodology introduced in Section 2.4. In short, the available laser wavelengths used in the Raman system include 532, 633, and 785 nm, which define the excitation conditions for different resonance modes. The spectrometer is equipped with diffraction gratings of varying groove densities, 1200 and 2400 g/mm, allowing for selection of the desired spectral range and resolution. Temporal Raman measurements are conducted to monitor the time-dependent evolution of product formation by tracking specific Raman peaks associated with the target molecules. Quantitative yield analysis is performed by calculating the integrated area of the fitted peaks which are calculated by spectral deconvolution methods.

In the Au ND-Sb_2S_3 cavity structure, the phase of the Sb_2S_3 film can undergo thermal-induced transitions, making it unstable in high-temperature environments, particularly in the amorphous phase. In addition, phase switching can also be triggered by the laser *via* photothermal effects. As shown in Figure 5.16, laser-induced crystallization occurs in the amorphous Au ND-Sb_2S_3 cavity when the laser power exceeds 3.30 mW during a 10 s illumination period, resulting in a visible color change that marks the localized phase transition. With increasing laser power or extended exposure time, the crystallized region expands correspondingly. During catalytic performance measurements, the laser-induced crystallization leads to a phase transition that reduces absorption at the target wavelength for MB degradation, thereby limiting photocatalytic reactivity. To mitigate this effect, the sample is measured under a controlled low-temperature environment at 15 °C using a Linkam LTS420 thermal stage. Additionally, the excitation laser power is reduced to 1.4 mW using a 20× objective lens to prevent unintentional phase switching during measurement. These parameters guarantee not only a stable phase during the measurement but also a considerable Raman intensity.

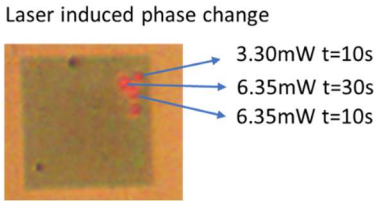

Figure 5.16 Laser in Raman spectrometer induces the phase change of amorphous Au ND-Sb_2S_3 cavity sample

Normalized Raman spectra were recorded over a 100 s period with a time interval of 1 s for both amorphous and crystalline Au ND-Sb_2S_3 cavity samples. The characteristic product peak appears at approximately 480 $cm^{-1}$and serves as an indicator of reaction yield. In the crystalline sample, shown in Figure 5.17B, the product peak exhibits a modest increase to 0.13, indicating suppressed catalytic activity. In contrast, the amorphous Au ND-Sb_2S_3 cavity sample (Figure 5.17A) demonstrates significantly enhanced reactivity, attributed to the stronger plasmonic resonance. The product peak intensity increases markedly, reaching a normalized value of 0.24.

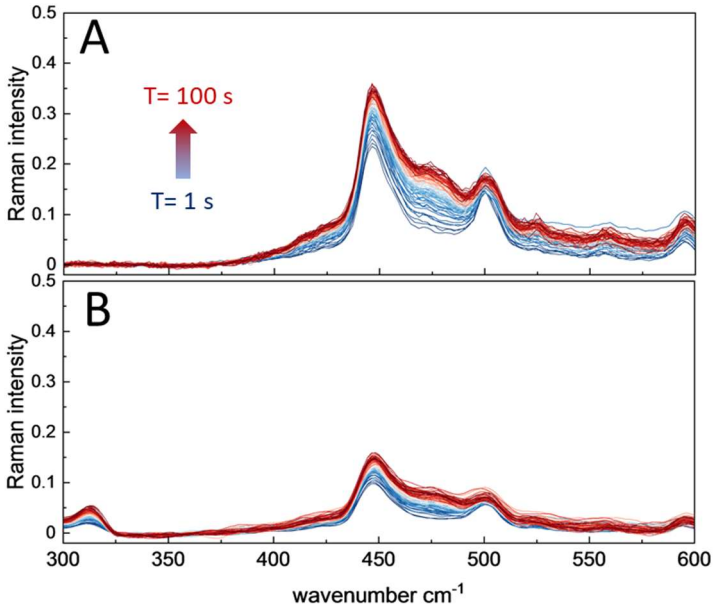

Figure 5.17 *in-situ* Raman spectra of amorphous (A) and crystalline (B) Au ND-Sb_2S_3 cavity for MB degradation reactions in 100s period. The peak intensity reveals the MB degradation process.

Moreover, quantitative analysis of the reaction yield reveals the time evolution of the product formation, as shown in Figure 5.18. Under experimental conditions, a noticeable increase in yield is observed around the 5s mark for both amorphous and crystalline samples. A rapid enhancement occurs within the first 20 s, followed by a steady increase throughout the 100 s measurement period. At the final timestep, the yield of the crystalline Au ND-Sb_2S_3 cavity reaches approximately 0.45. In contrast, the amorphous Au ND-Sb_2S_3 cavity achieves a significantly higher yield of 1.09, attributed to enhanced plasmonic resonance. And the repeatability of the product yields are revels in Appendix 7. Thus, under identical experimental conditions, the light-driven reaction demonstrates a two-fold increase in yield due to phase switching, highlighting the dynamic tunability of a single metasurface configuration.

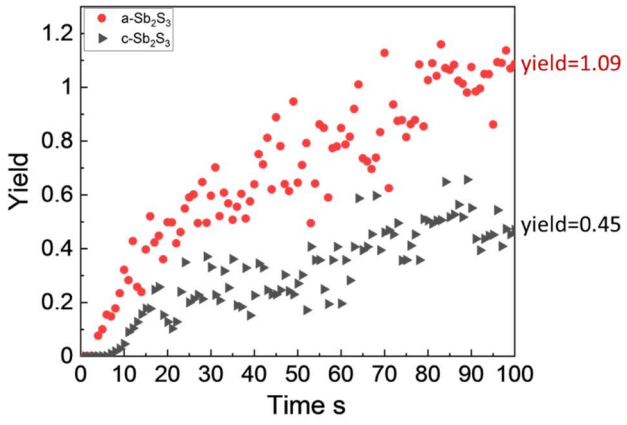

Figure 5.18 Yield of amorphous (red) and crystalline (black) Au ND-Sb_2S_3 cavity against the reaction processing time.

5.3.3.Temperature-dependent MB degradation and selective catalysis enhancement

To guarantee the stabilization of the Sb_2S_3 cavity material phase, the environmental temperature was reduced using a thermal stage. This stabilization is crucial for maximizing the reaction yield of the "switch-on" samples with the amorphous phase. Due to the photothermal effects of the laser, the local temperature of the sample is positively correlated with the laser power. With increasing laser power, the maximum achievable temperatures during SERS measurements are -60 °C (13.6 mW), -50 °C (6.8 mW) and 15 °C (1.4 mW). Temperature also has a significant effect on reactivity, influencing microscopy factors such as collision frequency and activation energy[131].

In Figure 5.19A, the yield of the MB reaction was measured and analyzed on a 140 nm amorphous Au ND-Sb_2S_3 cavity sample at various laser powers. The measurement period and time interval were kept the same values as in the characterization experiment described above. However, under SERS measurement at 13.6 mW, the material phase remained stable for only 30 s, even when the temperature was reduced to -60 °C. In these experiments, the laser power gradually increased from 1.4 to 13.6 mW to accelerate the reaction rate (as shown in Appendix 9). Despite this, the final yields decreased as the environmental temperature was lowered under the same illumination period. The maximum yield was obtained at 100 s with the lowest laser power (1.4 mW) at 15 °C, reaching 9.94. A similar phenomenon is observed in the SERS results at various temperatures in Figure 5.19B. The yield, calculated from the results measured on the 140 nm amorphous Au ND-Sb_2S_3 cavity sample with a 1.4 mW laser at -20 to 15 °C, increased

from 0.41 to 9.94 as the temperature rose. This can be explained by the increase in the kinetic energy of the reactant molecules.

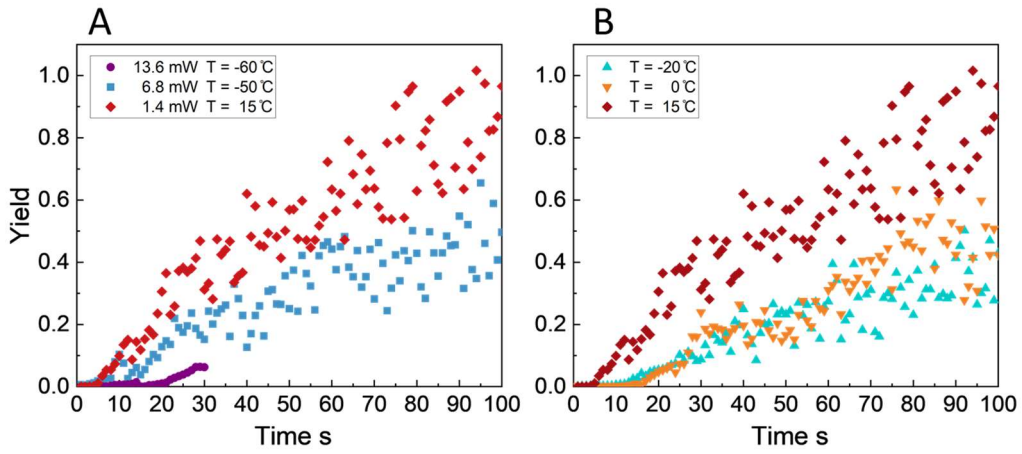

Figure 5.19 Yield of MB reaction products measured on Au ND-Sb_2S_3 cavity with 140 nm thickness amorphous cavity. The period is 100 s with 1 s as time intervals. A) The laser power is adjusted with neutral density filter in SERS. The environmental temperatures of sample are set as the height value to guarantee the Sb_2S_3 phase stability, which are -60 °C (power 13.6 mW), -50 °C (power 6.8 mW), 15 °C (power 1.4 mW). B) At the sample characterization laser power of 1.4 mW, the yields are measured from -20 to 15 °C.

Previous studies from our group demonstrated that the contribution of plasmon-mediated catalysis to MB degradation is primarily attributed to near-field enhancement and hot-carrier transfer[26]. In particular, for plasmonic-based metasurfaces, the local temperature increase does not exceed 8 °C due to the photothermal effect of LSPR excitation with a 6.6 mW, 633 nm laser. Even when heating MB powder up to 61 °C, no product fingerprints were observed in the SERS spectra. Thus, temperature increases up to 61 °C is not sufficient to drive the reaction. However, in the case of amorphous Au ND-Sb_2S_3 cavity samples, the results reveal considerable temperature-dependent reactivity within only a 15 °C variation. A possible explanation for this phenomenon is that temperatures enhance collisional frequency, thereby promoting the reaction. In this *in-situ* measurement system, both environmental temperature and laser excitation contribute to promoting MB reactions. The reaction is activated by LSPR, which involves near-field enhancement and hot-carrier transfer. Nevertheless, neither environmental temperature change nor photothermal effects are sufficient to induce the reaction. Therefore, the tunability of yield observed in Figure 5.18 is attributed to the plasmonic resonance of the metasurfaces.

Furthermore, as Au ND-Sb_2S_3 cavity reveals a tunable optical property in various wavelength range, which holds the catalytic potential of the across multiple reactions. It can be applied to

light-driven reactions involving molecular resonances that align with the other resonance peaks. Currently, we investigated catalytic activity at 633 nm using MB degradation. Additionally, the Au ND-Sb_2S_3 cavity exhibits tunable absorption at 800 nm, indicating its potential for photodegradation of dyes with molecular resonance energies aligned in the NIR range. Such dyes include Rhodamine 800 [132,133], IR-792 [134] and IR-813 [72] *et al*. These molecules possess HOMO-LUMO energy gaps near the NIR region, allowing reactant molecules to effectively absorb near-field photons and interact with hot electrons, enhancing and modulating photodegradation reactions[135,136]. In this design, the crystalline metasurface is expected to promote the reaction, enhance the product yield. And during the phase switching, a wider tunable range in absorption (51%) can be supported at this wavelength, which can optimize the manipulation. However, the lower photon energy at NIR limits the selection of dyes that can perfectly match the plasmonic resonance, making performance validation more challenging. Nevertheless, NIR photocatalysis holds promise for advanced applications, including systems involving two-photon absorption molecules or cascaded systems[129,135].

Moreover, the Au ND-Sb_2S_3 cavity can also support considerable absorption at specific wavelengths in both material phases. For instance, at 532 nm, both the amorphous and crystalline metasurfaces exhibit ~40% absorption. This allows aligned reactions to be catalyzed during phase switching. As an example, Rhodamine 6G (R6G) exhibits a fluorescence peak at 556 nm. Photocatalytic degradation of this molecule has been measured using SERS under 532 nm laser excitation[137,138], as shown in Appendix 10. In applications involving sequential reaction systems, this enhancement may be applied to activate and promote the initial reaction while achieving selectivity in the subsequent reactions.

The phase-induced modulation of light-driven reaction yields under various excitation wavelengths demonstrates the selective catalytic behavior of the metasurface toward reactions with different activation energies. In particular, MB degradation is effectively ‘switched on’ in the amorphous phase, showing an enhanced catalytic yield. However, this activity is significantly suppressed upon crystallization, while NIR photocatalysis is conversely enhanced in the crystalline phase. This phase-dependent behavior enables the selective production of different reaction products, highlighting the potential of phase-switchable metasurfaces to dynamically control chemical selectivity. Moreover, by tailoring the resonance peak wavelengths to align with specific reaction intermediates or pathways, the system holds the potential to selectively drive desired products in complex or multibranched reaction networks.

This study offers a promising strategy for tunable, light-driven control in chemical reactions, which can be employed in photo-regulated catalytic systems[139].

In summary, we have developed a tunable phase-change metasurface, the Au ND-Sb_2S_3 cavity system, that offers a predictable, reversible and dynamic platform for engineering the plasmonic resonance strength of Au NDs array *via* phase transitions of the cavity material. This tunability arises from tailored plasmonic resonance strength through mode hybridization with cavity resonances, enabled by high-speed refractive index changes during phase transformation between amorphous and crystalline. The reactivity of light-driven reactions can be selectively enhanced or suppressed depending on the phase state of the Sb_2S_3 cavity, which modulates resonance strength at particular wavelength in relation to the molecular HOMO-LUMO bandgap. For the model photodegradation reaction of MB, this controllable catalytic response enables precise yield modulation from 0.45 to 1.09 under identical illumination conditions using the single metasurface configuration. The proposed metasurface highlights a promising route for controlling reaction yields and achieving selective catalysis in multiple chemical systems.

Chapter 6. Summary and Outlook

6.1. Summary of metasurface strategies in light-driven reaction manipulation

Manipulating the reactivity of light-driven reactions requires strategies that precisely tune the strength of LSPRs, with particular focus on two non-thermal effects: localized electric field enhancement and hot-electron generation. To achieve this, various metasurface configurations have been developed to modulate plasmonic resonances through modes hybridization, polarization-dependent control, and phase-change material switching. By tailoring plasmonic resonances, it becomes possible to either suppress or enhance photocatalytic reactivity, enable to adjust product yields. Moreover, to reach targeted product generation rates, the relationship between measured absorption and product yield was systematically characterized in a model reaction, which are essential steps for achieving selective, proportional, and dynamic control over photocatalytic processes.

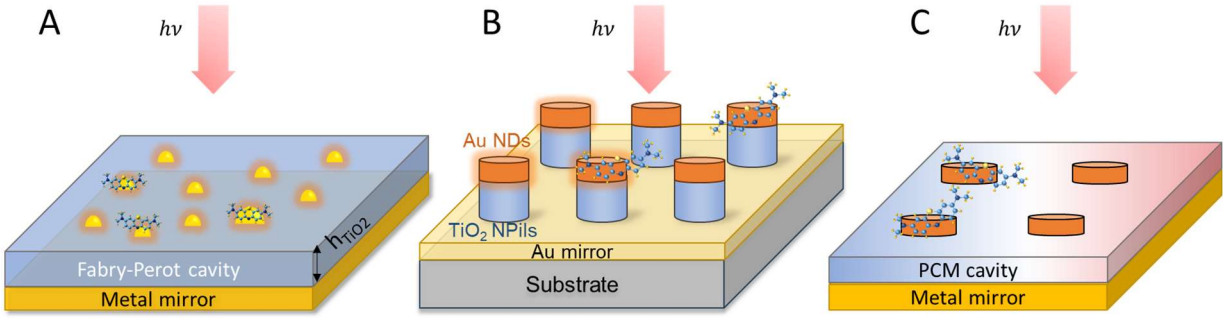

Figure 6.1 Metasurface designs for manipulating light-driven reactions, which support tunable plasmonic resonances *via* (A) strongly coupled resonance modes, (B) polarization-dependent switching and (C) material phase-changing.

According to these three strategies, metasurfaces were designed, fabricated and characterized as follows: Au nanoparticles coupled with a TiO_2 cavity (Au NP-cavity) in Chapter 3, an elliptical Au nanodisk capped TiO_2 nanopillar array (Au-TiO_2 NPil) in Chapter 4, and an Au

nanodisk array coupled with a phase-change material cavity (Au ND-cavity) in Chapter 5, as illustrated in Figure 6.1. Plasmonic resonances are supported by the Au nanostructures, whose morphological parameters, such as radius, periodicity (ordered or disordered), and thickness, are precisely engineered to tune the resonance wavelength toward the target spectral region. The tunable optical properties are further influenced by the semiconductor nanostructures, including TiO_2 and Sb_2S_3, which are adjusted through cavity thickness, nanostructure morphology, and the refractive index determined by the material phase. Measured absorption spectra reveal this tunability and directly reflect the strength of the plasmonic resonance. In light-driven reactions, reactant molecules attached to the surface undergo bond cleavage when energetic electrons are injected into their unoccupied molecular orbitals. This process is facilitated by near-field excitation and the diffusion of hot electrons from the plasmonic nanostructures. Across all three strategies, manipulation of product yield was demonstrated, effectively enabling both suppression and enhancement of photocatalytic reactions to achieve desired outcomes. Optical measurements were supported by simulations allowing to quickly assess the relevant parameter space, target sizes and shapes in the different designs.

Firstly, the Au NP-cavity nanostructures allow tuning the optical properties through the hybridization between the LSPR of the Au NPs and the F-P resonance of the TiO_2 cavity. The F-P resonance couples with the plasmonic mode, shifting it from a destructive node to a constructive peak, and thereby inducing tunable absorption ranging from 4% (h_{TiO2} = 105 nm) to 92% (h_{TiO2} = 182 nm) at the target wavelength of 633 nm, which is aligned with the effective range of the photocatalytic reaction. The yield of the model reaction product was monitored in real time *via* SERS, evaluated from the integrated area of the characteristic vibrational peak at 480 cm^{-1}. This yield increases from 0.07 in samples with suppressed absorption to a maximum of 7.18 in h_{TiO2} = 160 nm samples where the hybridized mode optimally overlaps with the molecular resonance (HOMO-LUMO gap). It is thus demonstrated that the yield of the product generation can be controlled in photocatalysis using a group of Au NP-cavities through plasmonic resonance modulation with strong mode coupling.

With this hybridization strategy, catalytic reactivity can be tuned over a wide range, enabling suppression, activation, or strong enhancement of product yields. This broad tunability arises because the plasmonic resonance can be shifted to lead to either suppressed or enhanced local fields at the target wavelength, depending on whether it couples at the node or peak of the F-P resonance, respectively. Furthermore, unlike lithographically fabricated nanostructures, these

samples are not limited by dimensional constraints: the scalable self-assembly of Au NPs ensures that this approach is suitable for practical devices. However, self-assembly approaches introduce a disordered distribution in nanoparticle size and interparticle spacing, resulting in difficulties to precisely predict the optical properties by using conventional simulations. Accurate modelling is possible by incorporating nanoparticle parameters extracted from AFM images, but computational speed significantly decreases due to the enlarged unit model size. Additionally, since tunability is achieved across a series of samples, the fraction of Au NP absorption does not perfectly align across samples, because of variations in coupling strength and fabrication uncertainty. As a result, the correlation between measured absorption and reaction yield is not strictly proportional. The best yield is obtained at the h_{TiO2} = 160 nm sample, corresponding to the second-highest measured absorption, which exhibits the plasmonic resonance peak closest to the target wavelength though, as confirmed by simulation results of near-field enhancement and hot electron generation rates. This mismatch reveals a challenge of reliably predicting catalytic performance based solely on experimentally measured optical properties in the group of samples.

Moreover, to overcome these limitations, tunable properties are realized within a single metasurface configuration: elliptical Au-TiO_2 NPil arrays. The asymmetric radii of the elliptical Au NDs and TiO_2 NPils support polarization-sensitive plasmonic resonances at different wavelengths under two orthogonal polarization states. Through morphology engineering, this metasurface achieves absorption of 89% under TM polarization and 58% under TE polarization at the target wavelength of 633 nm. The resulting near-field enhancement and hot-electron generation shift accordingly to efficiently interact with reactant molecules, controlling the product yield from 9.98 to 4.7 within a 10 s duration. At a longer wavelength of 850 nm, absorption can also be tuned from 61% (TE) to 27% (TM), enabling control over other reactions with aligned HOMO-LUMO gaps. Importantly, a linear proportional relationship is observed between measured absorption and reaction yield. These results highlight that by tuning the plasmonic resonance strength through structural asymmetry, resonance-driven photocatalytic reactions can be precisely controlled by switching the polarization state of the incident light. This provides a compact and adaptable strategy for continuously modulating chemical reactivity.

This morphological engineering approach enables a linear and predictable control over reaction yields, providing an effective route to achieve targeted catalytic performance. Different from

the Au NP-cavity systems, where mismatched coupling strengths complicate yield prediction, this design supports similar resonances under TE and TM polarizations at different wavelengths, avoiding such discrepancies. Tunability is realized within a single metasurface under identical illumination conditions, same light power, wavelength and illuminating duration, requiring only a change in polarization state and optimized with a highly compactable configuration. The metasurface also features a periodic, precisely tunable array structure, exhibiting excellent agreement with simulation results supporting predictable outcomes. However, due to the top-down lithographic fabrication process, the sample size is limited to ~$100 \times 100\ \mu m$. Scaling to larger samples increases fabrication complexity, requiring longer lithography times and introducing alignment uncertainties. In addition, compared with the Au NP-cavity design, the achievable absorption tuning range is narrower, since off-resonance absorption persists in the nanodisks, which are not designed to be actively suppressed.

Finally, Au ND-Sb_2S_3 cavity metasurfaces enable both enhancement and suppression of absorption within a single configuration as well using a different mechanism based on PCMs. Leveraging the phase-change properties of Sb_2S_3, whose refractive index shifts between the amorphous and crystalline states, the cavity resonance can be tuned to span both constructive peaks and destructive nodes. Measured absorption reveals a wide tuning range: from 78% (amorphous) to 39% (crystalline) at the target wavelength. Similar to the polarization-dependent metasurface, resonance tuning is also observed at longer wavelengths because of the redshift of the plasmonic peak, for example, at 785 nm the absorption increases from 19% (amorphous) to 65% (crystalline). In photocatalytic applications, the model reaction of MB degradation is modulated from 0.45 to 1.09 at 15 °C. Optical tunability at various wavelengths demonstrates the potential of the phase-change metasurfaces for multiple light-driven reactions with broad applicability for tuning reactivity at various molecular resonance energies.

By coupling plasmonic resonances with the PCM cavity, absorption can be tuned over a wider range around the desired laser wavelengths of 633 and 785 nm, effectively modulating the plasmonic resonance strength for reaction control. This design interacts with light of all polarization states, enhancing conversion efficiency under solar illumination. Although the lithographic fabrication of Au NPs still limits the overall array size, the cavity structure simplifies processing by avoiding uncertainties and challenges typically encountered during the etching step. However, the low thermal stability of the amorphous phase imposes constraints on environmental temperature and laser power during characterization, limiting the

acceleration of photocatalytic reactions. As a result, the yields of both amorphous samples (reactivity enhancement) and crystalline samples (reactivity suppression) are lower compared with those of polarization-dependent metasurfaces over the same time scale. But the ratio of maximum to minimum yield increases to 2.4, due to the broader tuning range of the plasmonic resonance enabled by strong coupling with the cavity resonance. At present, amorphous and crystalline Au ND-cavity metasurfaces are fabricated separately. The morphological stability of Au ND arrays has been evaluated under crystallization conditions, confirming their robustness. These results highlight the potential of the Au ND-Sb_2S_3 cavity strategy for high-speed switching and dynamic manipulation of light-driven reactions.

Table 6.1 Features of the three tunable metasurface strategies for light driven reaction control presented in this thesis.

Au NP-cavity	Au-TiO_2 NPil	Au ND- Sb_2S_3 cavity
disordered Au NPs	elliptical Au-TiO_2 array	regular Au ND array
additional uncertainty in simulation	simulation predictable	simulation predictable
mode hybridization	polarization switching	material phase change
enabling scalable fabrication	size constraint ($100 \times 100\ \mu m$) by lithographic techniques	size constraint ($100 \times 100\ \mu m$) by lithographic techniques
large tuning range in absorption	limited tuning range in absorption	considerable tuning range in absorption
no strictly linear correlation, correlation misalignment for two samples with largest absorption demonstrated	linear and proportional correlation	proportional correlation with the potential of high-speed switching

In summary, the key features of the three photocatalysis manipulation strategies are presented in Table *6.1*, providing guidance for optimizing catalytic performance and selecting application environments for these metasurface designs. In the Au NP-cavity design, light-driven reactions exhibit the widest tunability in product yield, enabling active suppression, activation, or promotion of reactions across a series of samples. By selecting specific samples, catalytic properties can be tailored to achieve desired reactivity. To improve the precision and resolution of control within a highly compactable design, metasurfaces with a single configuration, such as polarization-dependent designs, are employed to achieve tunable optical responses. In these systems, the linear relationship between measured absorption and product yield ensures precise modulation. Continuous tailoring of absorption allows gradual modulation of light-driven reactions to achieve targeted yields. However, the overall manipulation range remains limited

by the achievable absorption contrast, which requires further enhancement. The Au ND-Sb_2S_3 cavity design addresses this limitation by enabling tuning over a wider absorption range through coupling plasmonic resonances to cavity peaks and nodes at two material phases, improving the rate of yield modulation. Notably, the phase-switching property of Sb_2S_3 occurs on the nanosecond timescale, allowing instantaneous "switch on/off" control of photocatalytic activity. This approach achieves high-speed switching between suppressed and enhanced states of light-driven reactions. Moreover, due to the tunability of resonance wavelengths, multiple reactions can be selectively activated or modulated within the same configuration.

Future improvements may enhance catalytic performance by integrating these strategies. For example, Au ND arrays can be reshaped into elliptical nanodisks to introduce polarization-dependent resonances. Combining this morphology engineering with Sb_2S_3 material phase switching would broaden the range of yield modulation. Such hybrid designs could exploit both polarization switching and material phase switching to dynamically and proportionally control reaction outcomes. In addition, applying these metasurfaces to reactions with diverse reactant resonance energies would extend catalytic performance characterization across the full light spectrum, enabling investigation of the catalytic behavior for multiple reaction systems. The metasurface can be further engineered, for example with mode hybridization, to support advanced resonance modes at multiple wavelengths to meet the particular requirements of complex multistep reactions[140].

6.2. Light-driven reaction manipulation potential in multibranched reaction system

In multibranched reactions, multiple pathways compete through intermediate steps, as in CO_2 reduction and ammonia (NH_3) synthesis. It is crucial to selectively enhance specific pathways to determine the dominant product and suppress undesired byproducts, which is essential for enabling large-scale renewable fuel production. Catalysts play a key role in directing selectivity by promoting or suppressing particular intermediate steps, which both effectively enhance the conversion rates. In plasmon-assisted photocatalysis, plasmonic metasurfaces act locally as nanoresonators that strongly interact with incident light through both photothermal and non-thermal effects, catalyzing multiple reactions. In particular, the two non-thermal effects discussed in this thesis, near-field enhancement and hot-carrier generation[141], can be

engineered to supply energy to unoccupied adsorbate states, facilitating targeted reaction pathways[5] in multibranched systems.

Previous work by our group has demonstrated the potential of achieving product selectivity in CO_2 reduction. Density functional theory simulations showed that orbital hybridization between Au clusters and CO_2 mediates OH groups, creating more accessible electronic states, initiating the reaction and modulating electron transfer processes through plasmon resonance[142]. This reveals a promising route for selectivity control. Similarly, Cu dendritic nanostructures have been shown to promote the formation of multi-carbon species in photoelectrocatalytic reactions[143,144]. These results highlight the potential of plasmonic catalysis in harvesting and converting solar energy into valuable C_2^+ products with significant yield and selectivity.

Additionally, *in situ* characterization approaches are crucial for monitoring catalytic processes in real time, providing essential insights into the complexity of multibranched reactions. As introduced in this thesis, SERS can be applied not only for real-time monitoring but also for enhancing sensitivity through plasmonic resonance, making it particularly promising for studying multibranched systems. For example, CO_2 reduction and its products have recently been dynamically investigated using a microfluidic flow cell combined with SERS measurements[145] to understand the reaction process. Similarly, other vibrational and electron spectroscopies, such as FTIR spectroscopy and XPS, offer powerful tools for *in situ* characterization as well[25]. With advances in temporal and spatial resolution, these techniques make it possible to directly observe transient structures and morphologies, enabling the monitoring of active sites during multi-pathway reaction processes.

Within the three strategies presented in this work, reactivities can be tailored to further achieve selectivity in multibranched light-driven reactions. By integrating plasmonic metasurfaces with catalytic processes, precise computational methodologies in optical properties can be employed to predict and design catalytic performance. Advances in nanofabrication, particularly lithographic methods, enable precise tailoring of plasmonic resonances to support complicated resonance modes aligning with the requirements of multibranch reaction systems, such as initiating energies, reactant or intermediate molecular resonance energies *etc*. At the same time, self-assembly approaches provide a solution to overcome the size limitations of lithography-based nanofabrication, promoting efficient energy conversion. Product yields can also be

proportionally and dynamically controlled, increasing flexibility in product generation. When combined with *in situ* catalytic characterization, these approaches open opportunities to track the dynamic evolution of real active sites, actively modulating the reactivity to promote selectivity. Overall, these strategies hold the potential to achieve multidimensional selectivity, meeting the increasingly complex and precise design requirements of multibranched reaction systems.

Abbreviations

AFM	atomic force microscopy
a-Sb_2S_3	amorphous Sb_2S_3
Au ND-Sb_2S_3 cavity	gold nanodisk-Sb_2S_3 cavity
Au NP-cavity	gold nanoparticle-cavity
Au-TiO_2 Npil	Au and TiO_2 nanopillars
BIC	bound states in the continuum
CB	conduction band
CO2RR	CO_2 reduction reactions
c-Sb_2S_3	crystalline Sb_2S_3
DI	deionized
E-beam	electron beam
EBL	electron-beam lithography
EM	electromagnetic
FEM	finite element method
F-P	Fabry-Pérot
FTIR	Fourier transform infrared
FWHM	the full width at half maximum
HOMO	highest occupied molecular orbital
ICP	inductively coupled plasma
LSPR	localized surface plasmon resonance
LUMO	lowest unoccupied molecular orbital
MB	methylene blue
ND	nanodisk
NIR	near-infrared
NP	nanoparticle
Npil	nanopillar
PCM	phase-change material
PEC	photoelectrochemical
PML	perfectly matched layer
PRET	plasmon-induced resonant energy transfer
R	reflectance
RF	radio frequency
RT-TDDFT	real-time time-domain density functional theory
SEM	scanning electron microscopy
SERS	surface enhanced Raman spectroscopy
SNR	signal to noise

SPP	surface plasmon polariton
SPR	surface plasmon resonance
T	transmittance
TE	transverse electric
TM	transverse magnetic
UV	ultraviolet
VB	valence band
XRD	X-ray diffraction

Bibliography

1. Tu, W., Zhou, Y. & Zou, Z. Photocatalytic Conversion of CO_2 into Renewable Hydrocarbon Fuels: State-of-the-Art Accomplishment, Challenges, and Prospects. *Adv. Mater.* **26**, 4607–4626 (2014).
2. Habisreutinger, S. N., Schmidt-Mende, L. & Stolarczyk, J. K. Photocatalytic Reduction of CO_2 on TiO_2 and Other Semiconductors. *Angew. Chem. Int. Ed.* **52**, 7372–7408 (2013).
3. Halpe, P., Adams, M. & Walker, T. R. Challenges and opportunities for ports in achieving net-zero emissions in maritime transport. *Transp. Res. Interdiscip. Perspect.* **30**, 101379 (2025).
4. Fusco, Z., Edirisooriya, A., Lyu, N., David, C. & Beck, F. J. Metasurfaces for photochemistry. in *Semiconductors and Semimetals* vol. 115 149–179 (Elsevier, 2024).
5. Fusco, Z. & Beck, F. J. Advances in fundamentals and application of plasmon-assisted CO_2 photoreduction. *Nanophotonics* **13**, 387–417 (2024).
6. White, J. L. *et al.* Light-Driven Heterogeneous Reduction of Carbon Dioxide: Photocatalysts and Photoelectrodes. *Chem. Rev.* **115**, 12888–12935 (2015).
7. Fujishima, A. & Honda, K. Electrochemical Photolysis of Water at a Semiconductor Electrode. *Nature* **238**, 37–38 (1972).
8. Zhou, B. *et al.* Light-driven synthesis of C2H6 from CO2 and H2O on a bimetallic AuIr composite supported on InGaN nanowires. *Nat. Catal.* **6**, 987–995 (2023).

9. Camargo, P. H. C. & Cortés, E. *Plasmonic Catalysis: From Fundamentals to Applications*. (Wiley, 2021). doi:10.1002/9783527826971.

10. Huang, H. *et al.* Unraveling Surface Plasmon Decay in Core–Shell Nanostructures toward Broadband Light-Driven Catalytic Organic Synthesis. *J. Am. Chem. Soc.* **138**, 6822–6828 (2016).

11. Zhang, Y., Chen, Z., Luo, M., Ye, S. & Chen, S. Surface engineering strategies for particulate photocatalysts toward photocatalytic H_2 O_2 production. *Mater. Horiz.* 10.1039.D5MH00697J (2025) doi:10.1039/D5MH00697J.

12. Cushing, S. K. *et al.* Photocatalytic Activity Enhanced by Plasmonic Resonant Energy Transfer from Metal to Semiconductor. *J. Am. Chem. Soc.* **134**, 15033–15041 (2012).

13. Zhang, W. *et al.* Progress and Perspective of Electrocatalytic CO_2 Reduction for Renewable Carbonaceous Fuels and Chemicals. *Adv. Sci.* **5**, 1700275 (2018).

14. Ma, Y. *et al.* Titanium Dioxide-Based Nanomaterials for Photocatalytic Fuel Generations. *Chem. Rev.* **114**, 9987–10043 (2014).

15. Fujishima, A., Rao, T. N. & Tryk, D. A. Titanium dioxide photocatalysis. (2000).

16. Meng, A. *et al.* TiO2/polydopamine S-scheme heterojunction photocatalyst with enhanced CO2-reduction selectivity. *Appl. Catal. B Environ.* **289**, 120039 (2021).

17. Linic, S., Christopher, P. & Ingram, D. B. Plasmonic-metal nanostructures for efficient conversion of solar to chemical energy. *Nat. Mater.* **10**, 911–921 (2011).

18. Linic, S., Aslam, U., Boerigter, C. & Morabito, M. Photochemical transformations on plasmonic metal nanoparticles. *Nat. Mater.* **14**, 567–576 (2015).

19. Li, J. *et al.* Plasmon-induced photonic and energy-transfer enhancement of solar water splitting by a hematite nanorod array. *Nat. Commun.* **4**, 2651 (2013).

20. Mascaretti, L. & Naldoni, A. Hot electron and thermal effects in plasmonic photocatalysis. *J. Appl. Phys.* **128**, 041101 (2020).

21. Sun, J. & Wang, G. Achieving Near Infrared Photodegradation by the Synergistic Effect of Z-Scheme Heterojunction and Antenna of Rare Earth Single Atoms. *Small* **21**, 2412148 (2025).

22. Keasling, J. *et al.* Microbial production of advanced biofuels. *Nat. Rev. Microbiol.* **19**, 701–715 (2021).

23. Bharath, G. & Banat, F. High-Grade Biofuel Synthesis from Paired Electrohydrogenation and Electrooxidation of Furfural Using Symmetric Ru/Reduced Graphene Oxide Electrodes. *ACS Appl. Mater. Interfaces* **13**, 24643–24653 (2021).

24. Yang, D. *et al.* Selective electroreduction of carbon dioxide to methanol on copper selenide nanocatalysts. *Nat. Commun.* **10**, 677 (2019).

25. Li, X., Wang, S., Li, L., Sun, Y. & Xie, Y. Progress and Perspective for In Situ Studies of CO_2 Reduction. *J. Am. Chem. Soc.* **142**, 9567–9581 (2020).

26. Fusco, Z., Catchpole, K. & Beck, F. J. Investigation of the mechanisms of plasmon-mediated photocatalysis: synergistic contribution of near-field and charge transfer effects. *J. Mater. Chem. C* **10**, 7511–7524 (2022).

27. Sun, Y. & Tang, Z. Photocatalytic hot-carrier chemistry. *MRS Bull.* **45**, 20–25 (2020).

28. Zhao, J. *et al.* Modulation of *CH_xO Adsorption to Facilitate Electrocatalytic Reduction of CO_2 to CH_4 over Cu-Based Catalysts. *J. Am. Chem. Soc.* **145**, 6622–6627 (2023).

29. Hu, H. *et al.* Catalytic Metasurfaces Empowered by Bound States in the Continuum. *ACS Nano* **16**, 13057–13068 (2022).

30. Mao, Z. *et al.* Tuning Redox Potential of Gold Nanoparticle Photocatalysts by Light. *ACS Nano* **14**, 7038–7045 (2020).

31. Wang, W. *et al.* Generation of Hot Electrons with Chiral Metamaterial Perfect Absorbers: Giant Optical Chirality for Polarization-Sensitive Photochemistry. *ACS Photonics* **6**, 3241–3252 (2019).

32. Yalavarthi, R. *et al.* Enhancing Photoelectrochemical Energy Storage by Large-Area CdS-Coated Nickel Nanoantenna Arrays. *ACS Appl. Energy Mater.* **4**, 11367–11376 (2021).

33. Wang, Y. *et al.* Hot Electron-Driven Photocatalysis Using Sub-5 nm Gap Plasmonic Nanofinger Arrays. *Nanomaterials* **12**, 3730 (2022).

34. Liu, Y.-E. *et al.* Quantum-Coherence-Enhanced Hot-Electron Injection under Modal Strong Coupling. *ACS Nano* **17**, 8315–8323 (2023).

35. Shi, X. *et al.* Enhanced water splitting under modal strong coupling conditions. *Nat. Nanotechnol.* **13**, 953–958 (2018).

36. Yuan, L. *et al.* A Quasi-Bound States in the Continuum Dielectric Metasurface-Based Antenna–Reactor Photocatalyst. *Nano Lett.* **24**, 172–179 (2024).

37. Cortés, E. *et al.* Optical Metasurfaces for Energy Conversion. *Chem. Rev.* **122**, 15082–15176 (2022).

38. Besteiro, L. V., Kong, X.-T., Wang, Z., Hartland, G. & Govorov, A. O. Understanding Hot-Electron Generation and Plasmon Relaxation in Metal Nanocrystals: Quantum and Classical Mechanisms. *ACS Photonics* **4**, 2759–2781 (2017).

39. Zhan, C., Moskovits, M. & Tian, Z.-Q. Recent Progress and Prospects in Plasmon-Mediated Chemical Reaction. *Matter* **3**, 42–56 (2020).

40. Herran, M. *et al.* Plasmonic bimetallic two-dimensional supercrystals for H2 generation. *Nat. Catal.* **6**, 1205–1214 (2023).

41. Dutta, A. *et al.* Gap-plasmon enhanced water splitting with ultrathin hematite films: the role of plasmonic-based light trapping and hot electrons. *Faraday Discuss.* **214**, 283–295 (2019).

42. Mayer, K. M. & Hafner, J. H. Localized Surface Plasmon Resonance Sensors. *Chem. Rev.* **111**, 3828–3857 (2011).

43. Yang, J. *et al.* Manipulation of the dephasing time by strong coupling between localized and propagating surface plasmon modes. *Nat. Commun.* **9**, 4858 (2018).

44. Li, Z., Clark, A. W. & Cooper, J. M. Dual Color Plasmonic Pixels Create a Polarization Controlled Nano Color Palette. *ACS Nano* **10**, 492–498 (2016).

45. Kumar, K. *et al.* Printing colour at the optical diffraction limit. *Nat. Nanotechnol.* **7**, 557–561 (2012).

46. Xu, R. *et al.* Programmable Multiple Plasmonic Resonances of Nanoparticle Superlattice for Enhancing Photoelectrochemical Activity. *Adv. Funct. Mater.* **30**, 2005170 (2020).

47. Loh, J. Y. Y. *et al.* Near-Perfect Absorbing Copper Metamaterial for Solar Fuel Generation. *Nano Lett.* **21**, 9124–9130 (2021).

48. Gao, H., Liu, C., Jeong, H. E. & Yang, P. Plasmon-Enhanced Photocatalytic Activity of Iron Oxide on Gold Nanopillars. *ACS Nano* **6**, 234–240 (2012).

49. Chung, T., Lee, S.-Y., Song, E. Y., Chun, H. & Lee, B. Plasmonic Nanostructures for Nano-Scale Bio-Sensing. *Sensors* **11**, 10907–10929 (2011).

50. Yan, J., Liu, X., Ma, C., Huang, Y. & Yang, G. All-dielectric materials and related nanophotonic applications. *Mater. Sci. Eng. R Rep.* **141**, 100563 (2020).

51. Sinelnik, A. *et al.* Ultrafast all-optical second harmonic wavefront shaping. *Nat. Commun.* **15**, 2507 (2024).

52. Zhao, S., Fusco, Z. & Beck, F. J. Strong and tunable absorption in coupled nanoparticle–cavity systems for plasmonically enhanced hot electron devices. *Optica* **9**, 1084 (2022).

53. El-Helou, A. J. *et al.* Optical Metasurfaces for the Next-Generation Biosensing and Bioimaging. *Laser Photonics Rev.* **19**, 2401715 (2025).

54. Guan, J. *et al.* Light–Matter Interactions in Hybrid Material Metasurfaces. *Chem. Rev.* **122**, 15177–15203 (2022).

55. Volakis, J. L., Chatterjee, A. & Kempel, L. C. *Finite Element Method Electromagnetics: Antennas, Microwave Circuits, and Scattering Applications*. (Wiley-Interscience, IEEE Press, Piscataway, New Jersey, 1998). doi:10.1109/9780470544655.

56. Kim, S.-S. *Fundamentals and Principles of Electromagnetic Wave Absorbers: From Theory, Design, and Materials to Measurement*. (Springer, Singapore, 2025).

57. Kao, K. C. Optical and Electro-Optic Processes. in *Dielectric Phenomena in Solids* 115–212 (Elsevier, 2004). doi:10.1016/B978-012396561-5/50013-X.

58. Ren, Z., Kalscheuer, T., Greenhalgh, S. & Maurer, H. A goal-oriented adaptive finite-element approach for plane wave 3-D electromagnetic modelling. *Geophys. J. Int.* **194**, 700–718 (2013).

59. Ciuprina, G., Ioan, D. & Sabariego, R. V. Electric circuit element boundary conditions in the finite element method for full-wave passive electromagnetic devices. *J. Math. Ind.* **12**, 7 (2022).

60. Bielak, J. *The Finite Element Method: A Primer*. (Springer International Publishing, Cham, 2024). doi:10.1007/978-3-031-56369-0.

61. Busch, K., König, M. & Niegemann, J. Discontinuous Galerkin methods in nanophotonics. *Laser Photonics Rev.* **5**, 773–809 (2011).

62. Duczek, S., Duvigneau, F. & Gabbert, U. The finite cell method for tetrahedral meshes. *Finite Elem. Anal. Des.* **121**, 18–32 (2016).

63. Navarro, E. A., Gimena, B. & Cruz, J. L. Modelling of periodic structures using the finite difference time domain method combined with the Floquet theorem. *Electron. Lett.* **29**, 446–447 (1993).

64. Ainsworth, M. Essential boundary conditions and multi-point constraints in finite element analysis. *Comput. Methods Appl. Mech. Eng.* **190**, 6323–6339 (2001).

65. Saini, R. K., Kumar, A., Goyal, V., Agarwal, A. & Prajesh, R. Evaluating EM-field enhancement of different shapes of metallic nanoparticles using COMSOL multiphysics for SERS-based sensors. *Mater. Today Proc.* **76**, 383–387 (2023).

66. Devaraj, V., Lee, J.-M., Kim, Y.-J., Jeong, H. & Oh, J.-W. Engineering Efficient Self-Assembled Plasmonic Nanostructures by Configuring Metallic Nanoparticle's Morphology. *Int. J. Mol. Sci.* **22**, 10595 (2021).

67. Neumann, K. *et al.* A Stochastic Large-Signal Model for Printed High-Frequency Rectifiers Used for Efficient Generation of Higher Harmonics. *IEEE Trans. Microw. Theory Tech.* **68**, 2151–2160 (2020).

68. Zhang, J., Zhang, L. & Xu, W. Surface plasmon polaritons: physics and applications. *J. Phys. Appl. Phys.* **45**, 113001 (2012).

69. Schirato, A. *et al.* Quantifying Ultrafast Energy Transfer from Plasmonic Hot Carriers for Pulsed Photocatalysis on Nanostructures. *ACS Nano* **18**, 18933–18947 (2024).

70. Fang, Y., Verre, R., Shao, L., Nordlander, P. & Käll, M. Hot Electron Generation and Cathodoluminescence Nanoscopy of Chiral Split Ring Resonators. *Nano Lett.* **16**, 5183–5190 (2016).

71. Zhang, J. *et al.* Photothermal effect and application of photothermal materials in photocatalysis and photoelectric catalysis. *Microstructures* **4**, (2024).

72. Launay, V. *et al.* NIR Organic Dyes as Innovative Tools for Reprocessing/Recycling of Plastics: Benefits of the Photothermal Activation in the Near-Infrared Range. *Adv. Funct. Mater.* **31**, 2006324 (2021).

73. Lyu, N. *et al.* Coupled Au Nanoparticle-Cavity Nanostructures for Precise Control in Resonance-Driven Photocatalytic Reactions. *ACS Nano* **19**, 25821–25829 (2025).

74. David, C. TiO_2 Self-Assembled, Thin-Walled Nanotube Arrays for Photonic Applications. *Materials* **12**, 1332 (2019).

75. Baffou, G. *Thermoplasmonics: Heating Metal Nanoparticles Using Light*. (Cambridge University Press, 2017). doi:10.1017/9781108289801.

76. Tesema, T. E., Annesley, C. & Habteyes, T. G. Plasmon-Enhanced Autocatalytic N-Demethylation. *J. Phys. Chem. C* **122**, 19831–19841 (2018).

77. Khan, I. *et al.* Review on Methylene Blue: Its Properties, Uses, Toxicity and Photodegradation. (2022).

78. Tesema, T. E., Kafle, B., Tadesse, M. G. & Habteyes, T. G. Plasmon-Enhanced Resonant Excitation and Demethylation of Methylene Blue. *J. Phys. Chem. C* **121**, 7421–7428 (2017).

79. Zhou, L., Johnson, R., Habteyes, T. & Guo, H. Adsorption of methylene blue and its N-demethylated derivatives on the (111) face of coinage metals: The importance of dispersion interactions. *J. Chem. Phys.* **146**, (2017).

80. Pezzi, L. *et al.* Photo-thermal study of a layer of randomly distributed gold nanoparticles: from nano-localization to macro-scale effects. *J. Phys. Appl. Phys.* **50**, 435302 (2017).

81. Smith, E. & Dent, G. *Modern Raman Spectroscopy: A Practical Approach*. (Wiley, 2019). doi:10.1002/9781119440598.

82. Flanagan, A. R. & Glavin, F. G. Open-source Raman spectra of chemical compounds for active pharmaceutical ingredient development. *Sci. Data* **12**, 498 (2025).

83. Shao, L. & Griffiths, P. R. Automatic Baseline Correction by Wavelet Transform for Quantitative Open-Path Fourier Transform Infrared Spectroscopy. *Environ. Sci. Technol.* **41**, 7054–7059 (2007).

84. Zhao, J., Woznicki, T. & Kusnierek, K. Estimating baselines of Raman spectra based on transformer and manually annotated data. *Spectrochim. Acta. A. Mol. Biomol. Spectrosc.* **330**, 125679 (2025).

85. Blacha-Grzechnik, A., Piwowar, K., Zassowski, P., Motyka, R. & Zak, J. In-situ Raman spectroelectrochemical studies on thionine layer electrochemically grafted to the gold surface. *Electrochimica Acta* **245**, 902–911 (2017).

86. Hutchinson, K., Hester, R. E., Albery, W. J. & Hillman, A. R. Raman spectroscopic studies of a thionine-modified electrode. *J. Chem. Soc. Faraday Trans. 1 Phys. Chem. Condens. Phases* **80**, 2053 (1984).

87. Orito, Y. Practical Methodology in Kinetic Modeling for Complex Reactions: Weighted Error Manipulation to Allow Effective Model Evaluation in a Borderline S_N Reaction. *ACS Omega* **10**, 9266–9274 (2025).

88. Li, J., Zhao, F., Zhao, J. & Zeng, B. Adsorptive and stripping behavior of methylene blue at gold electrodes in the presence of cationic gemini surfactants. *Electrochimica Acta* **51**, 297–303 (2005).

89. Nie, Z., Petukhova, A. & Kumacheva, E. Properties and emerging applications of self-assembled structures made from inorganic nanoparticles. *Nat. Nanotechnol.* **5**, 15–25 (2010).

90. Fang, Y. *et al.* Plasmon Enhanced Internal Photoemission in Antenna-Spacer-Mirror Based Au/TiO_2 Nanostructures. *Nano Lett.* **15**, 4059–4065 (2015).

91. Scanlon, D. O. *et al.* Band alignment of rutile and anatase TiO2. *Nat. Mater.* **12**, 798–801 (2013).

92. Derkachova, A., Kolwas, K. & Demchenko, I. Dielectric Function for Gold in Plasmonics Applications: Size Dependence of Plasmon Resonance Frequencies and Damping Rates for Nanospheres. *Plasmonics* **11**, 941–951 (2016).

93. Novotny, L. Strong coupling, energy splitting, and level crossings: A classical perspective. *Am. J. Phys.* **78**, 1199–1202 (2010).

94. Törmä, P. & Barnes, W. L. Strong coupling between surface plasmon polaritons and emitters: a review. *Rep. Prog. Phys.* **78**, 013901 (2015).

95. Deeb, C. *et al.* Size Dependence of the Plasmonic Near-Field Measured via Single-Nanoparticle Photoimaging. *J. Phys. Chem. C* **117**, 10669–10676 (2013).

96. Chikkaraddy, R. *et al.* Single-molecule strong coupling at room temperature in plasmonic nanocavities. *Nature* **535**, 127–130 (2016).

97. Fusco, Z. *et al.* Self-assembly of Au nano-islands with tuneable organized disorder for highly sensitive SERS. *J. Mater. Chem. C* **7**, 6308–6316 (2019).

98. Doan, M. Q. *et al.* Ultrasensitive Detection of Methylene Blue Using an Electrochemically Synthesized SERS Sensor Based on Gold and Silver Nanoparticles: Roles of Composition and Purity on Sensing Performance and Reliability. *J. Electron. Mater.* **51**, 150–162 (2022).

99. Alam, A.-M. *et al.* Generating Color from Polydisperse, Near Micron-Sized TiO_2 Particles. *ACS Appl. Mater. Interfaces* **9**, 23941–23948 (2017).

100. Zhang, Y., Guo, W., Zhang, Y. & Wei, W. D. Plasmonic Photoelectrochemistry: In View of Hot Carriers. *Adv. Mater.* **33**, 2006654 (2021).

101. Capitolis, J. *et al.* Two-dimensional photonic metasurfaces for slow light-controlled photocatalysis.

102. Goh, X. M. *et al.* Three-dimensional plasmonic stereoscopic prints in full colour. *Nat. Commun.* **5**, 5361 (2014).

103. Lee, T., Jang, J., Jeong, H. & Rho, J. Plasmonic- and dielectric-based structural coloring: from fundamentals to practical applications. *Nano Converg.* **5**, 1 (2018).

104. Wang, H. *et al.* Full Color Generation Using Silver Tandem Nanodisks. *ACS Nano* **11**, 4419–4427 (2017).

105. Zhu, Z., Bai, B., You, O., Li, Q. & Fan, S. Fano resonance boosted cascaded optical field enhancement in a plasmonic nanoparticle-in-cavity nanoantenna array and its SERS application. *Light Sci. Appl.* **4**, e296–e296 (2015).

106. Hüttenhofer, L. *et al.* Metasurface Photoelectrodes for Enhanced Solar Fuel Generation. *Adv. Energy Mater.* **11**, 2102877 (2021).

107. Zhirnov, E. *et al.* ICP etching of III-nitride based laser structure with Cl2–Ar plasma assisted by Si coverplate material. *J. Vac. Sci. Technol. Vac. Surf. Films* **23**, 687–692 (2005).

108. Oehrlein, G. S. *et al.* Future of plasma etching for microelectronics: Challenges and opportunities. *J. Vac. Sci. Technol. B* **42**, 041501 (2024).

109. Gibson, S. J. *et al.* Tapered InP nanowire arrays for efficient broadband high-speed single-photon detection. *Nat. Nanotechnol.* **14**, 473–479 (2019).

110. DuChene, J. S., Tagliabue, G., Welch, A. J., Cheng, W.-H. & Atwater, H. A. Hot Hole Collection and Photoelectrochemical CO2 Reduction with Plasmonic Au/p-GaN Photocathodes. *Nano Lett* (2018).

111. Li, X. *et al.* Designing multi-metal-site nanosheet catalysts for CO2 photoreduction to ethylene. *Nat. Commun.* **16**, (2025).

112. Delaney, M., Zeimpekis, I., Lawson, D., Hewak, D. W. & Muskens, O. L. A New Family of Ultralow Loss Reversible Phase-Change Materials for Photonic Integrated Circuits: Sb_2S_3 and Sb_2Se_3. *Adv. Funct. Mater.* **30**, (2020).

113. Dong, W. *et al.* Wide Bandgap Phase Change Material Tuned Visible Photonics. *Adv. Funct. Mater.* **29**, 1806181 (2019).

114. Chamoli, S. K., Verma, G., Singh, S. C. & Guo, C. Phase change material based hot electron photodetection. *Nanoscale* **13**, 1311–1317 (2021).

115. Zhao, X., Lou, T., Peng, Y., Sun, F. & Wei, X. Metasurface-Based Photodetectors: Pursuing Superior Performance and Multifunctionality. *ACS Photonics* acsphotonics.5c00691 (2025) doi:10.1021/acsphotonics.5c00691.

116. Wang, Q. *et al.* Optically reconfigurable metasurfaces and photonic devices based on phase change materials. *Nat. Photonics* **10**, 60–65 (2016).

117. Delaney, M. *et al.* Nonvolatile programmable silicon photonics using an ultralow-loss Sb_2Se_3 phase change material. *Sci. Adv.* **7**, (2021).

118. Hosseini, P., Wright, C. D. & Bhaskaran, H. An optoelectronic framework enabled by low-dimensional phase-change films. *Nature* **511**, 206–211 (2014).

119. Wuttig, M., Bhaskaran, H. & Taubner, T. Phase-change materials for non-volatile photonic applications. *Nat. Photonics* **11**, 465–476 (2017).

120. David, C., Kühler, P., Javier García De Abajo, F. & Siegel, J. Near-field nanoimprinting using colloidal monolayers. *Opt. Express* **22**, 8226 (2014).

121. Kim, H.-T. *et al.* Electrical oscillations induced by the metal-insulator transition in VO2. *J. Appl. Phys.* **107**, (2010).

122. Miller, K. J., Hallman, K. A., Haglund, R. F. & Weiss, S. M. Silicon waveguide optical switch with embedded phase change material. *Opt. Express* **25**, 26527 (2017).

123. Qazilbash, M. M. *et al.* Mott Transition in VO_2 Revealed by Infrared Spectroscopy and Nano-Imaging. *Science* **318**, 1750–1753 (2007).

124. Osorio Mayon, Y., White, T. P., Wang, R., Yang, Z. & Catchpole, K. R. Evaporated and solution deposited planar Sb_2S_3 solar cells: A comparison and its significance. *Phys. Status Solidi A* **213**, 108–113 (2016).

125. Wedemeyer, H. *et al.* Nanocrystalline solar cells with an antimony sulfide solid absorber by atomic layer deposition. *Energy Env. Sci* **6**, 67–71 (2013).

126. Han, Z. *et al.* Electrically Reconfigurable Plasmonic Metasurfaces Based on Phase-Change Materials $Sb_2 S_3$. *Nano Lett.* **25**, 7435–7441 (2025).

127. Chen, R. *et al.* Deterministic quasi-continuous tuning of phase-change material integrated on a high-volume 300-mm silicon photonics platform. *Npj Nanophotonics* **1**, (2024).

128. Laprais, C. *et al.* Reversible Single-Pulse Laser-Induced Phase Change of $Sb_2 S_3$ Thin Films: Multi-Physics Modeling and Experimental Demonstrations. *Adv. Opt. Mater.* **12**, 2401214 (2024).

129. Parize, R. *et al.* In situ analysis of the crystallization process of Sb 2 S 3 thin films by Raman scattering and X-ray diffraction. *Mater. Des.* **121**, 1–10 (2017).

130. Pala, N. & Karabiyik, M. Electron Beam Lithography (EBL). in *Encyclopedia of Nanotechnology* (ed. Bhushan, B.) 1033–1057 (Springer Netherlands, Dordrecht, 2016). doi:10.1007/978-94-017-9780-1_344.

131. Chapter 4 The influence of temperature on reaction rate. in *Studies in Physical and Theoretical Chemistry* vol. 86 117–138 (Elsevier, 1999).

132. Kolesnichenko, P. V., Tollerud, J. O. & Davis, J. A. Background-free time-resolved coherent Raman spectroscopy (CSRS and CARS): Heterodyne detection of low-energy vibrations and identification of excited-state contributions. *APL Photonics* **4**, 056102 (2019).

133. Etchegoin, P. G. & Le Ru, E. C. Resolving Single Molecules in Surface-Enhanced Raman Scattering within the Inhomogeneous Broadening of Raman Peaks. *Anal. Chem.* **82**, 2888–2892 (2010).

134. AL-Aqmar, D. M., Al-Shamiri, H. A. S., AL-Shareef, J. M., Abou Kana, M. T. H. & Kandel, H. M. Spectroscopic and Photo-Physical Properties of Near-IR Laser Dye in Novel Benign Green Solvents. *J. Fluoresc.* **30**, 1095–1103 (2020).

135. Han, C., Kundu, B. K., Liang, Y. & Sun, Y. Near-Infrared Light-Driven Photocatalysis with an Emphasis on Two-Photon Excitation: Concepts, Materials, and Applications. *Adv. Mater.* **36**, 2307759 (2024).

136. Yu, L. *et al.* In Situ Construction of Near-Infrared Response Hybrid Up-Conversion Photocatalyst for Degrading Organic Dyes and Antibiotics. *Molecules* **28**, 6674 (2023).

137. Zehentbauer, F. M. *et al.* Fluorescence spectroscopy of Rhodamine 6G: Concentration and solvent effects. *Spectrochim. Acta. A. Mol. Biomol. Spectrosc.* **121**, 147–151 (2014).

138. Moreki, M. A., Matlou, G. G. & Rapulenyane, N. Photo-Catalytic Degradation of Rhodamine 6g Under Visible Lamp Using Citrate Stabilized Zno Nanoparticles. Preprint at https://doi.org/10.2139/ssrn.5179095 (2025).

139. Xu, C., Bing, W., Wang, F., Ren, J. & Qu, X. Versatile Dual Photoresponsive System for Precise Control of Chemical Reactions. *ACS Nano* **11**, 7770–7780 (2017).

140. Wang, J.-P., Zong, M.-H. & Li, N. Photobiocatalysis: A promising tool for sustainable synthesis. *Chem Catal.* **4**, 100933 (2024).

141. Manjavacas, A., Liu, J. G., Kulkarni, V. & Nordlander, P. Plasmon-Induced Hot Carriers in Metallic Nanoparticles. *ACS Nano* **8**, 7630–7638 (2014).

142. Fusco, Z., Koenig, D., Smith, S. C. & Beck, F. J. *Ab initio* investigation of hot electron transfer in CO_2 plasmonic photocatalysis in the presence of hydroxyl adsorbate. *Nanoscale Horiz.* **9**, 1030–1041 (2024).

143. Fusco, Z., Riaz, A., David, C. & Beck, F. J. Cathodoluminescence Spectroscopy of Complex Dendritic Au Architectures for Application in Plasmon-Mediated Photocatalysis and as SERS Substrates. *Adv. Mater. Interfaces* **10**, 2202236 (2023).

144. Schrader, T., Shaji, A., David, C. & Perlt, E. Theoretical investigation on the formation of ethylene on a gold surface. Preprint at https://doi.org/10.48550/arXiv.2509.22835 (2025).

145. Kumari, G., Zhang, X., Devasia, D., Heo, J. & Jain, P. K. Watching Visible Light-Driven CO_2 Reduction on a Plasmonic Nanoparticle Catalyst. *ACS Nano* **12**, 8330–8340 (2018).

146. Johnson, P. B. & Christy, R. W. Optical Constants of the Noble Metals. *Phys. Rev. B* **6**, 4370–4379 (1972).

147. Gao, L., Lemarchand, F. & Lequime, M. Refractive index determination of SiO_2 layer in the UV/Vis/NIR range: spectrophotometric reverse engineering on single and bi-layer designs. *J. Eur. Opt. Soc.-Rapid Publ.* **8**, 13010 (2013).

148. Wang, J. *et al.* Ultrasensitive SERS detection of rhodamine 6G and p-nitrophenol based on electrochemically roughened nano-Au film. *Talanta* **210**, 120631 (2020).

149. Kamal, S., Chowdhury, A. & Chung-Kuang Yang, T. Ultrasensitive SERS detection of Rhodamine 6G using a silver enriched MOF-derived CuFe2O4 microcubes substrate. *Spectrochim. Acta. A. Mol. Biomol. Spectrosc.* **270**, 120826 (2022).

Acknowledgments

This research was conducted as part of the collaboration between Friedrich Schiller University Jena (FSU) and The Australian National University (ANU) through the International Research Training Group IRTG 2675 “Meta-Active” C4 Project. The project was funded by the German Research Foundation (DFG, Deutsche Forschungsgemeinschaft) under the grant number GEPRIS 437527638. The cooperation between the two universities made this work possible, and I am deeply grateful for the contributions of many excellent researchers involved.

First and foremost, I would like to express my sincere gratitude to my supervisor, Dr. habil. Christin David, for her invaluable guidance and support. Her insightful supervision, encouragement, and expertise have been fundamental to my development as an independent researcher. She has also provided me with valuable opportunities to develop my academic knowledges and research skills, also to present our works at academic conferences.

I would also like to extend my heartfelt thanks to my co-supervisor at ANU, A/Prof. Fiona J. Beck, for her guidance in the experimental aspects of this project and for offering me the opportunity to work in an advanced research environment.

My sincere thanks also go to my colleagues Ms. Anjalie Edirisooriya, Dr. Zelio Fusco**,** and Dr. Shenyou Zhao for their support in fabrication, characterization techniques, and data analysis. I am also grateful for the fruitful collaboration with Prof. Lan Fu and Mr. Dawei Liu in nanofabrication, as well as for access to world class NCRIS facilities (ANFF-ACT Node) at ANU.

I would like to acknowledge Prof. Ulf Peschel and all colleagues from the Institute of Condensed Matter Theory and Optics for their valuable discussions and suggestions throughout my research.

Finally, I would like to express my heartfelt thanks to Mr. Dawei Liu, my partner, for his continuous support and understanding. I am also deeply grateful to Dr. Jiajia Li and all my friends for their companionship and encouragement over the past four years. Above all, I thank my family for their unwavering love and support, which have sustained me throughout this journey.

Publications

1. **Lyu, N.**; Edirisooriya, A.; Fusco, Z.; Liu, D.; Fu, L.; Beck, F. J.; and David, C. 'Polarization-dependent elliptical nanopillar metasurface for selective light-driven reactions', *Advance Optical Materials* (2026).

2. **Lyu, N.**; Edirisooriya, A.; Fusco, Z.; Zhao, S.; Beck, F. J.; David, C. Coupled Au Nanoparticle-Cavity Nanostructures for Precise Control in Resonance-Driven Photocatalytic Reactions. *ACS Nano* **2025**, *19* (28), 25821–25829.

3. Fusco, Z.; Edirisooriya, A.; **Lyu, N.**; David, C.; Beck, F. J. Metasurfaces for Photochemistry. In *Semiconductors and Semimetals*; Elsevier, 2024; Vol. 115, pp 149–179.

4. **Lyu, N.**; Edirisooriya, A.; Liu, D.; Fusco, Z.; Zhao, S.; Fu, L.; Beck, F. J.; and David, C. Tuning Plasmonic Metasurfaces via Phase Change Material Substrates for Modulating Reactivity in Light-Driven Reactions. Preprint at https://doi.org/10.48550/arXiv.2604.09293 (2026).

Ehrenwörtliche Erklärung

Ich erkläre hiermit ehrenwörtlich, dass ich die vorliegende Arbeit selbständig, ohne unzulässige Hilfe Dritter und ohne Benutzung anderer als der angegebenen Hilfsmittel und Literatur angefertigt habe. Die aus anderen Quellen direkt oder indirekt übernommenen Daten und Konzepte sind unter Angabe der Quelle gekennzeichnet.

Bei der Auswahl und Auswertung folgenden Materials haben mir die nachstehend aufgeführten Personen in der jeweils beschriebenen Weise entgeltlich/unentgeltlich geholfen:
1.... Dawei Liu and Lan Fu: Rezept zur Herstellung von Nanostrukturen
2.... Fiona Beck and Zelio Fusco: MATLAB-Code zur Nanopartikelgrößenanalyse und SERS-Peak-Anpassung
3.... Anjalie Edirisooriya: AFM-Messung von Au NPs
Weitere Personen waren an der inhaltlich-materiellen Erstellung der vorliegenden Arbeit nicht beteiligt. Insbesondere habe ich hierfür nicht die entgeltliche Hilfe von Vermittlungs- bzw. Beratungsdiensten (Promotionsberater oder andere Personen) in Anspruch genommen.

Niemand hat von mir unmittelbar oder mittelbar geldwerte Leistungen für Arbeiten erhalten, die im Zusammenhang mit dem Inhalt der vorgelegten Dissertation stehen.
Die Arbeit wurde bisher weder im In- noch im Ausland in gleicher oder ähnlicher Form einer anderen Prüfungsbehörde vorgelegt.
Die geltende Promotionsordnung der Physikalisch-Astronomischen Fakultät ist mir bekannt.
Ich versichere ehrenwörtlich, dass ich nach bestem Wissen die reine Wahrheit gesagt und nichts verschwiegen habe.

Ort, Datum Unterschrift d. Verfassers

Appendices

Appendix 1. FEM simulation of disordered Au NPs with AFM images

To simulate the optical properties of disordered Au NPs, the AFM image can be imported into the simulation model. Figure A. 1 illustrates both the periodic and aperiodic unit models for the nanoparticles. As mentioned in Chapter 3.1, the periodic simulation model is constructed using the average parameters calculated from the SEM images. In Figure A. 1B, the AFM image reflects the height distribution of the nanoparticles, generating disordered quasi-spherical NPs. To minimize the influence of noise in the AFM measurements, the images are smoothed to remove high-frequency components.

The size of a single unit structure is $250 \times 238\, nm$, which is 134 times larger than that of the periodic model. Periodic boundary conditions are applied to all four surrounding surfaces to simulate the optical response of an infinite layer. In this model, the substrate consists of a silicon/silica bilayer, with a Ti layer serving as the back reflector. The TiO_2 cavity has thicknesses of 89 nm and 147 nm, corresponding to the F-P resonance peak and node, respectively.

Disordered Au NPs are coupled on the top surface of the cavity, resulting in an enhanced response around 650 nm for the h_{TiO2} = 89 nm sample, as shown in Figure A. 2. A tunable absorption is observed at this wavelength, showing an absorption difference of 82% between the two samples. Although image smoothing was applied to reduce noise, residual high-frequency noise produced a few small artificial nanoparticles (~1 nm in radius), which induced some sharp peaks in the simulation results.

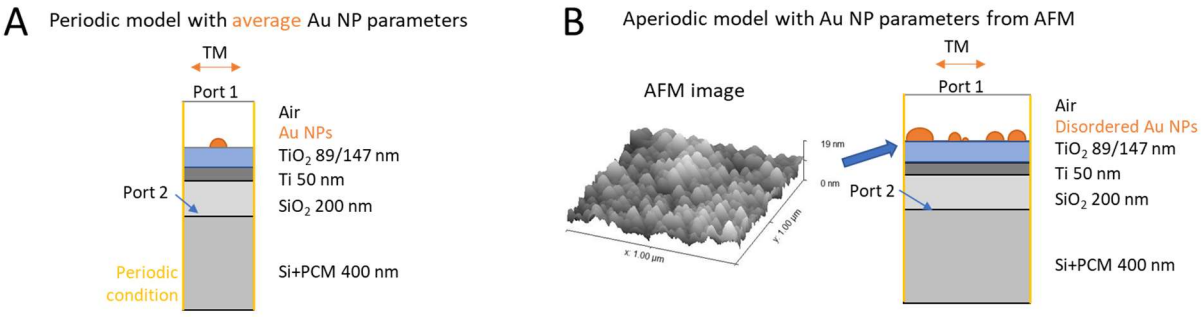

Figure A. 1 Simulation models of periodic (A) and aperiodic (B) Au NPs. The periodic model is based on the average parameters of Au NPs, while the aperiodic model is constructed from the AFM image of the Au NPs.

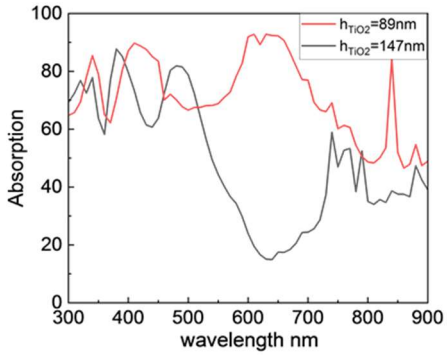

Figure A. 2 Simulated absorption spectra of Au NP-coupled TiO_2 cavities with thicknesses of 89 nm (red curve) and 147 nm (black curve), calculated using the aperiodic model. Noise in the AFM image affects the spectral quality, introducing sharp peaks.

Appendix 2. . Materials model applied in simulation model

Material	Source of refractive index
Air	Ideal model with n = 1, k = 0 for all wavelength
Gold (Au)	Johnson and Christy 1972: n, k 0.188 - 1.937 µm[146]
Titanium dioxide (TiO_2)	From results of ellipsometer, shown in Figure 3.2
Silicon dioxide (SiO_2)	Gao et al. 2013: n, k 0.252 - 1.25 µm[147]
Antimony sulfide (Sb_2S_3)	From results of ellipsometer, shown in Figure 5.6

Appendix 3. Principle of ellipsometry

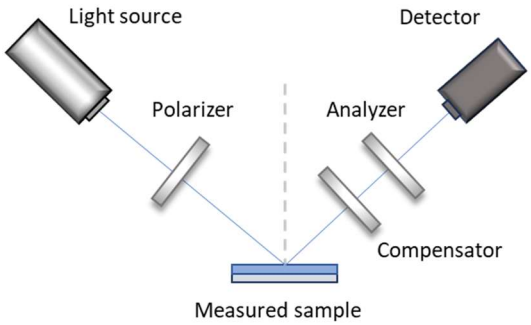

Figure A. 3 Basic principle of ellipsometer of a thin film sample

The refractive index of a thin film materials can be measured with ellipsometry, which are shown in Figure A. 3. The broadband light source covers a wild wavelength range from 200 to 2000 nm. And the light passes through the linear polarizer, and the polarization of the light is between s-wave and p-wave. And the linear-polarized light shines on the measured sample reflected the light. According to Snell's law, the incident angle is identical with the reflected light, which is set as 55°, 65°, and 75°. And the reflected beam has a different respond at two perpendicular polarizations, which propagates through the compensator and analyzer and collects by a detector.

The complex reflectance ratio ρ is measured, which reveals the ratio of s- and p-wave

$$\rho = \frac{r_p}{r_s} = \tan\Psi \; e^{i\Delta} \tag{A.1}$$

where r_p and r_s represent the reflectance of s-wave and p-wave, respectively. And the $\tan\Psi$ is the amplitude ratio upon reflection, and Δ is the phase shift which can be evaluated by the results of ellipsometer. The measured result is compared with a model constructed with an initial estimated model, and determined the refractive index, thickness and roughness of the sample.

Appendix 4. Raman spectrum peaks and band assignment for MB and N-Demethylated derivatives

Raman shift cm^{-1}	Band assignment
446	C-N-C skeletal deformation

479	skeletal deformation mode of thionine
501	C-N-C skeletal deformation
610	C-S-C skeletal deformation
772	C-H in-plane bending
804	NH_2 rocking vibration of thionine
1390	C-N symmetric stretching
1426	C-N asymmetric stretching
1434	C-N asymmetric stretching
1622	C-C ring stretching

Appendix 5. Simulated optical properties of Au-TiO_2 NPil array

The absorption spectra of Au-TiO_2 NPil arrays were calculated as a function of array periodicity to investigate the coupling effects among NPils. As shown in Figure A. 4, although the LSPR wavelength remains nearly stable as the periodicity increases from 150 to 300 nm, the resonance strength decreases, because an additional field enhancement is provided by the lattice resonance through inter-coupling between neighboring Au NDs. The resonance strength increases at smaller gap distances between plasmonic elements, reaching about 85% at a periodicity of 150 nm. Considering fabrication precision, the periodicity was set to 200 nm.

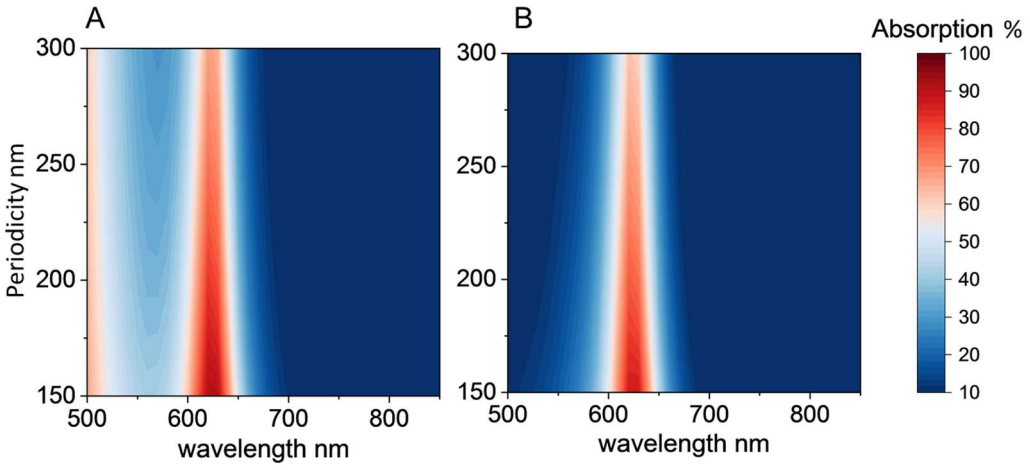

Figure A. 4 Simulated absorption spectra of the Au-TiO_2 NPil array with increasing periodicity in the x-direction, showing the total absorption (A) and the absorption of the Au nanodisks (B). The incident light is TM-polarized, and the NPil radii are r_x = 30 nm and r_y = 60 nm.

The non-thermal effects of LSPR in Au-TiO_2 NPil arrays were simulated using the approaches introduced in Section 2.2.2. The near-field enhancement and hot-electron generation rate are shown in Figure A. 5. Similar to the absorption trend, significant enhancement can be observed for both effects under TM polarization. The peak wavelength is approximately 670 nm, which is slightly red-shifted compared to the LSPR excitation wavelength, due to radiative damping in the nanostructure. The tunability arises from the increase in nanopillar radius, which induces a redshift of the peak to over 850 nm in both the localized electric field and the hot-electron generation rate. At the target wavelength of 633 nm, the electric field enhancement decreases from 60 (TM) to 11 (TE), while the hot-electron generation rate decreases from 27.2×10^{13} s^{-1} (TM) to 5.3×10^{13} s^{-1} (TE).

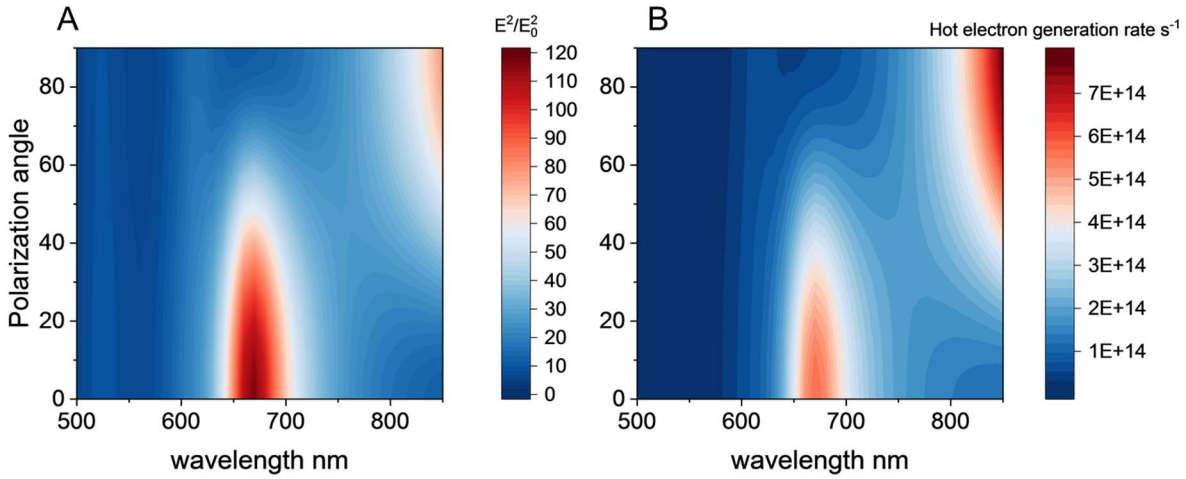

Figure A. 5 Simulated LSPR effects of Au-TiO_2 NPil array under various polarization from 0°(TM) to 90°(TE), which contains electric field enhancement(A) and hot electron generation rate(B). The radii of NPil in the model are r_x = 35 nm and r_y = 60 nm, and periodicity is 200 nm.

Appendix 6. Raman spectrum of MB degradation on Au mirror substrate

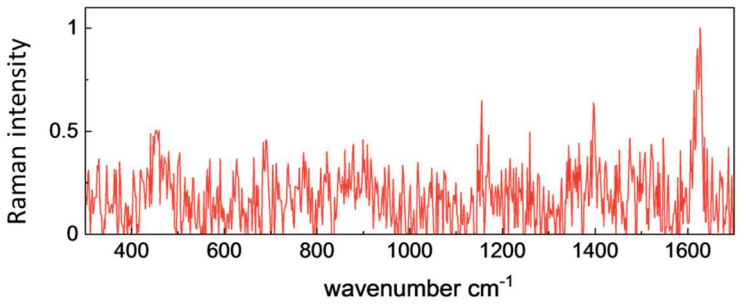

Figure A. 6 SERS measurement of MB degradation on reference samples, Au mirror substrate. Due to the limited signal intensity, the integrate time are increase to 10s. The signal is normalized at 1600 cm^{-1} peak.

Appendix 7. Three measurements of amorphous and crystalline Au NP-Sb_2S_3 cavity in MB degradation yield

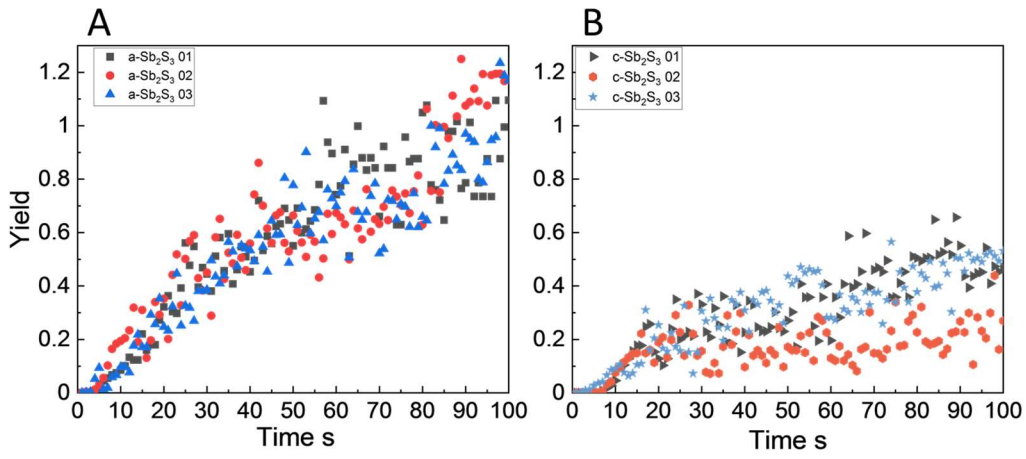

Figure A. 7 Product yields of MB reaction on amorphous and crystalline Au NP-Sb_2S_3 cavity

Appendix 8. Non-thermal effects simulation of Au NP-Sb_2S_3 cavity

The two non-thermal effects of the Au NP-Sb_2S_3 cavity were evaluated for two phase states, amorphous and crystalline, as shown in Figure A. 8. The catalytic activity, represented by near-field enhancement and hot electron generation rate, reveals a significant difference between the two material phases. At the target wavelength of 633 nm, both effects exhibit remarkable enhancement in the amorphous sample (h_{Sb2S3} = 40 nm), leading to an increased in excited electron population. Specifically, the electric field intensity is enhanced by a factor of 13, and the hot electron generation rate reaches 8.3×10^{13} s^{-1}.

However, upon crystallization, a dramatic reduction is observed across a broad spectral range from 400 to 900 nm. The change in the imaginary component of the refractive index extends the cut-off wavelength of Sb_2S_3, reducing the optical loss of cavity and then weakening the plasmonic resonance, which in turn increases tunability. When the crystalline sample is excited at 633 nm, the electric field intensity decreases to approximately 1/30 of that in the amorphous phase (0.43), and the hot electron generation rate drops to about 1/50 (0.2×10^{13} s^{-1}).

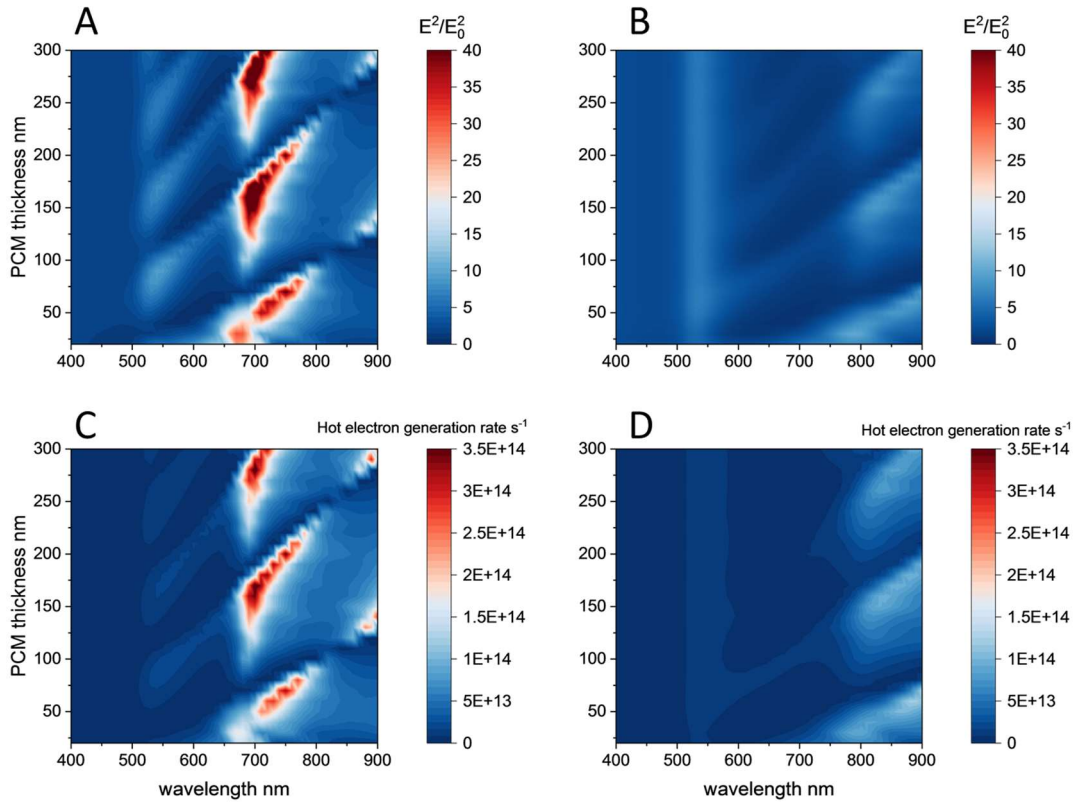

Figure A. 8 Simulated non-thermal effects of Au NP-Sb_2S_3 cavity which contains electrical field enhancement of amorphous phase(A), electrical field enhancement of crystalline phase(B), hot electron generation rate of amorphous phase (C) and hot electron generation rate of crystalline phase(D)

Appendix 9. Raman results of amorphous Au NP-Sb_2S_3 cavity under various laser power and environment temperature

The photothermal effect of the laser can induce a phase change during Raman measurements. The operating temperature of the sample is reduced to ensure stabilization of the cavity phase. As the laser power increases, the photothermal effect becomes stronger, and a lower temperature is required. The temperature is controlled by a Linkam LTS420 thermal stage. The Raman spectra of the amorphous Au NP-Sb_2S_3 cavity were measured with a 633 nm laser under

different laser powers for MB reactions. The measurement period was 100 s, and signals were collected every 1 s. The temperature was set to the highest value at which the cavity material phase remained stable, which are 15°C (1.36 mW), -50°C (6.8 mW) and -60°C (13.6 mW). Notably, for measurements with 13.6 mW laser power, characterization can only be conducted for 30 s. Longer illumination periods also induced crystallization. Although the laser power increased, the intensity of the product peaks at the final time step decreased as shown in Figure A. 9, reflecting a suppression of the reaction yield due to the lower temperature.

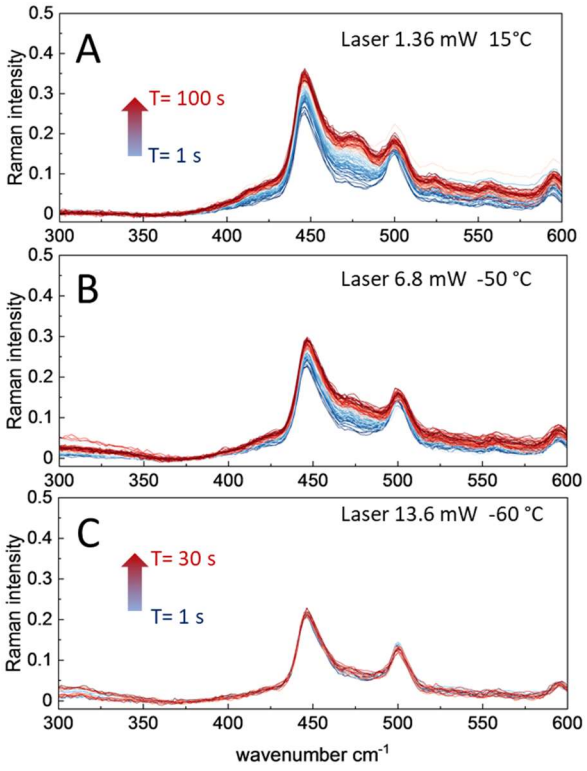

Figure A. 9 Raman spectrum of amorphous Au NP-Sb_2S_3 cavity at highest stable temperature with the later power in 1.36, 6.8 and 13.6 mW.

Considering the reactivity of the "switch-on" sample, the laser power was set to 10 mW. The Raman spectra were also measured at increasing temperatures from -20 to 15 °C reveals in Figure A. 10. The intensity of the product peak increased with rising temperature. The promotion of the reaction is strongly related to the processing temperature. Therefore, to enhance the reactivity of the "switch-on" sample and optimize turnability, the processing temperature was set to 15 °C.

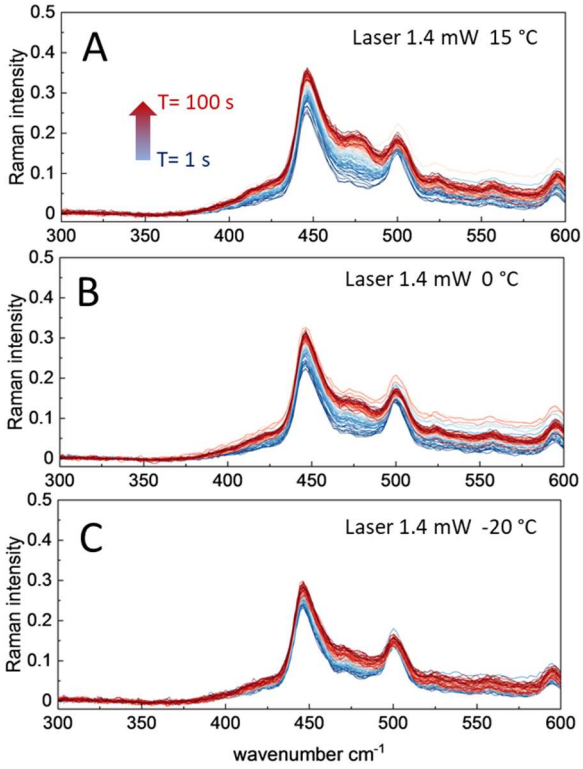

Figure A. 10 Raman spectrum of amorphous Au NP-Sb_2S_3 cavity at different temperatures from -20 to 15 °C with 1.36 mW laser.

Appendix 10. SERS measurement results of Au ND-Sb_2S_3 cavity with other reactions

To assess the catalytic performance of the Au ND-Sb_2S_3 cavity under 532 nm excitation, real-time Raman spectroscopy was employed using a 1.69 mW laser. The samples were immersed in a 20 ppm R6G solution overnight to ensure sufficient molecular adsorption. The Raman spectra, shown in Figure A. 11, captures the degradation process for both amorphous and crystalline Au ND-Sb_2S_3 cavities. Two characteristic peaks of the reactant molecules at 1362 and 1648 cm^{-1} are used to monitor the reaction[148], as their intensities correlate with the concentration of R6G, decreasing as the reaction progresses[149]. At 1648 cm^{-1}, the Raman intensity in the amorphous Au ND-Sb_2S_3 cavity decreased from 684 to 136, while the crystalline counterpart showed a similar reduction from 693 to 163. However, in current results, multiple factors contributed to the peak intensity decreasing. An effective approach to evaluate product yield of this chemical are still under developing.

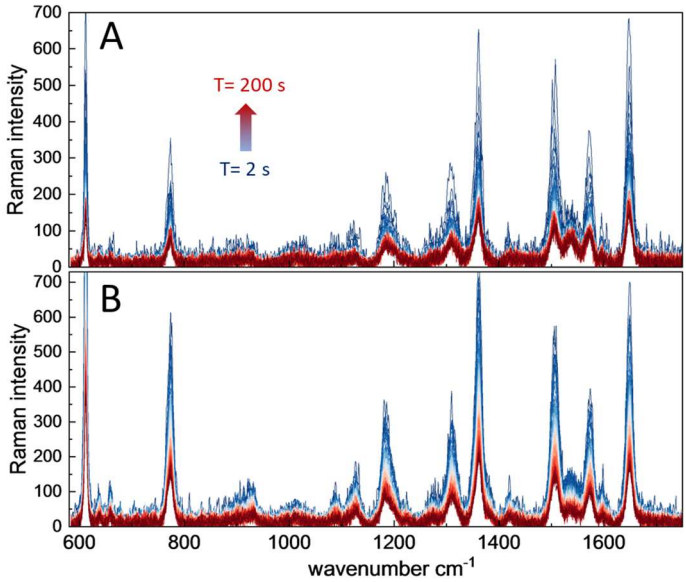

Figure A. 11 *in-situ* Raman spectra of amorphous (A) and crystalline (B) Au ND-Sb_2S_3 cavity for Rhodamine 6G degradation reaction in a 200 s period